Angular defined photo-electron sources for the KATRIN experiment

von

Jan Hendrik Christian Hein

Diplomarbeit in Physik

angefertigt im

Institut für Kernphysik

vorgelegt der

Mathematisch-Naturwissenschaftlichen Fakultät

der

Westfälischen Wilhelms-Universität

Münster

im Januar 2010

Ich versichere, dass ich die Arbeit selbständig verfasst und keine anderen als die angegebenen Quellen und Hilfsmittel benutzt, sowie Zitate kenntlich gemacht habe.

Referent:	Prof. Dr. C. Weinheimer
Korreferent:	Prof. Dr. D. Frekers

Contents

Chapter 1

Introduction

This diploma thesis focuses on the development of an angular selective photoelectron source for the KATRIN experiment[1]. The KATRIN collaboration aims to measure the mass of the electron antineutrino by investigating the kinematics of the Tritium decay. The shape of the electron energy spectrum is directly dependent on the neutrino mass $m(\bar{\nu}_e)$:

$$\frac{dN}{dE_{\mathrm{kin}}} \propto (E_0 - E_{\mathrm{kin}})\sqrt{(E_0 - E_{\mathrm{kin}})^2 - m^2(\bar{\nu}_e)},$$

see figure 1.2. A non zero neutrino mass is best observable in the endpoint region where deviations are directly visible in the spectral shape. With three years of measuring time the KATRIN experiment will be able to detect a neutrino mass of $m(\bar{\nu}_e) = 0.30\,\mathrm{eV}$ with $3\,\sigma$ significance, or $m(\bar{\nu}_e) = 0.35\,\mathrm{eV}$ at $5\,\sigma$ respectively. In case no signal different from $0\,\mathrm{eV}$ can be detected, the experiment will be able to set an upper limit on the neutrino mass of $m(\bar{\nu}_e) < 0.20\,\mathrm{eV}$ at $90\,\%$ confidence level, thus improving present upper limits by one order of magnitude.

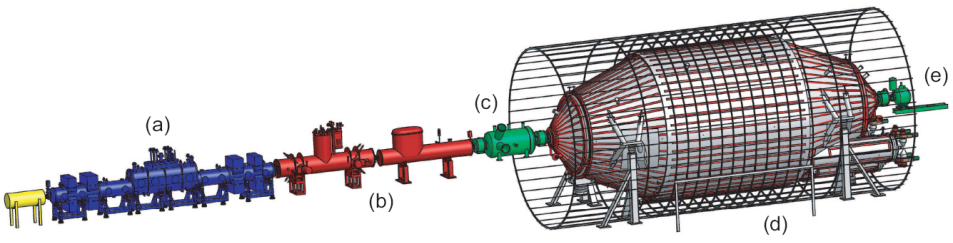

Figure 1.1: The KATRIN setup (without monitor spectrometer): a) windowless gaseous Tritium source, b) transport section, c) pre-spectrometer, d) main spectrometer with air coil system and e) detector section. Illustration from [Thü07]

[1] *KArlsruhe TRItium Neutrino Experiment*

The KATRIN setup is shown in figure 1.1. It basically consists of a source and transportation system (STS), a detector system and three *MAC-E* filters[2], namely the pre-, main and monitor-spectrometer. These spectrometers are high pass filters, designed to examine the high energetic tail of the electron kinetic spectrum of the Tritium decay at $E_0 = 18.6\,\mathrm{keV}$, see figure 1.2. Since the focus of this thesis are development and construction of an angular selective calibration source to investigate the properties of the main spectrometer, the principle of *MAC-E* filters is discussed in the following. For more information about the KATRIN experiment, see [Col05].

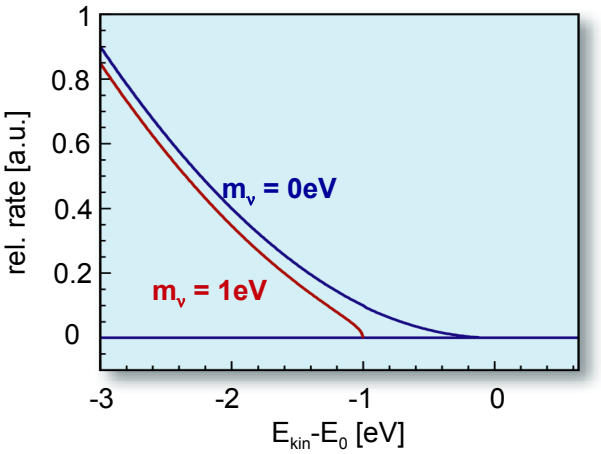

Figure 1.2: Schematic illustration of the electron energy spectrum endpoint for a β decay for two hypothetic electron neutrino masses $m(\bar{\nu}_e)$.

1.1 Principle of MAC-E filters

The interval of the spectrum below E_0 holds only a small fraction of electrons, hence a spectrometer with large angular and hight energy resolution is required. A *MAC-E* filter, working on the principle of magnetic adiabatic collimation fulfills these demands. The basic principle is illustrated in figure 1.3 for the case of the main spectrometer.

A spectrometer of *MAC-E* filter type is a high pass filter, based on electrostatic retardation of electrons. The analyzing plane is the region of highest electric potential U_0 and filters the electrons in dependence of their longitudinal kinetic energy $E_\parallel$. To increase the angular acceptance of the filter the isotropically distributed electron momenta need to be collimated into longitudinal direction, otherwise at small electron surplus energies only a small

[2] *MAC-E* stands for Magnetic Adiabatic Collimation and Electrostatic filter

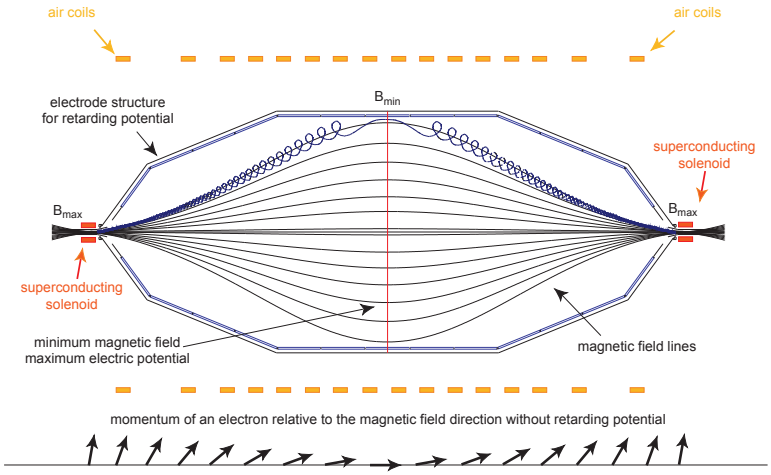

Figure 1.3: Schematic drawing of the KATRIN main-spectrometer as an example for a *MAC-E* filter. An exaggerated cyclotron motion of an electron is shown in blue. The arrows at the bottom of the figure give the relative momentum of an example electron. Taken from reference [Hug08]

fraction of isotropically distributed electrons with sufficient energies would pass the spectrometer.

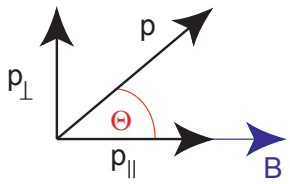

Figure 1.4: Definition of the angle Θ, taken from [Hug08]

.

The MAC-E filter uses strong magnetic fields for this purpose, created by superconducting solenoids, see figure 1.3. Electrons from Tritium decay are adiabatically guided in a spiral motion along the magnetic field lines into the spectrometer. The kinetic energy can be described in terms of longitudinal and transversal energy in good non-relativistic approximation as

$$E_{\text{kin}} = E_{\parallel} + E_{\perp} \tag{1.1}$$

$$E_{\parallel} = E_{\text{kin}} \cos^2 \theta \tag{1.2}$$

$$E_{\perp} = E_{\text{kin}} \sin^2 \theta \tag{1.3}$$

according to figure 1.4. With only slight changes of the magnetic field strength over a cyclotron period, the motion remains adiabatic, meaning

that the magnetic flux $\Phi = \int B\, dA$ enclosed by the gyration trajectory is constant. The electrons possess a magnetic moment μ, which is in non-relativistic terms expressed as

$$\mu = |\vec{\mu}| = \frac{e}{2m_e}|\vec{l}| = \frac{E_\perp}{B}. \tag{1.4}$$

Since in the case of the Tritium decay, the electrons gain a maximum Lorentz factor of $\gamma = 1.04 \approx 1$, the non-relativistic approximation may be used to good approximation. The magnetic moment is in case of non relativistic adiabatic guidance a conserved quantity[3]

$$\mu = \frac{E_\perp}{B} = \text{const.} \tag{1.5}$$

According to equation 1.5, with decreasing magnetic field strengths towards the analyzing plane, the electron transversal energy $E_\perp$ is transformed into longitudinal energy. As a result the full kinetic energy of an electron can be analyzed by the filter, except for the small amount of transversal energy due to the remaining magnetic field B_{min} in the analyzing plane.

Adiabatically guided, electrons enter the spectrometer through the entrance solenoid. According to equation 1.5, the transversal energy of an electron is increased in the high magnetic field. In case the transversal energy reaches a certain level, the angle θ (equation 1.3) exceeds $90\,^\circ$ and is magnetically reflected.

Assuming an electron angle $\theta = 90\,^\circ$ at the highest magnetic field B_{max} at the center of a solenoid, then the complete electron energy $E_{\text{kin,max}}$ is stored in the transversal component $E_\perp$. This electron will retain the maximum possible transversal energy ΔE in the analyzing plane with a magnetic field B_{min}. This can be expressed as (eq. 1.5)

$$\frac{E_{\text{kin,max}}}{B_{\text{max}}} = \frac{\Delta E_\perp}{B_{\text{min}}}. \tag{1.6}$$

This maximally possible transversal energy $\Delta E_\perp$ can not be analyzed and is expressed as the spectrometers resolution:

$$\Delta E = \frac{B_{\text{min}}}{B_{\text{max}}} \cdot E_0. \tag{1.7}$$

For the KATRIN main spectrometer with $B_{\text{max}} = 6\,\text{T}$, $B_{\text{min}} = 3 \cdot 10^{-4}\,\text{T}$ and $E_0 \approx 18600\,\text{eV}$ follows a resolution of $\Delta E = 0.93\,\text{eV}$. The transmission

[3] In the relativistic case $\gamma\mu$ is conserved.

function[4] of a MAC-E filter is expressed as

$$T(E_{kin}, U_0) = \begin{cases} 0 & E_{kin} < qU_0 \\ 1 - \sqrt{1 - \frac{E_{kin} - qU_0}{E_{kin}} \frac{B_{start}}{B_{min}}} & \text{for} \quad qU_0 \leq E_{kin} \leq \frac{qU_0}{1 - \frac{B_{min}}{B_{start}}} \\ 1 & \frac{qU_0}{1 - \frac{B_{min}}{B_{start}}} \leq E_{kin} \end{cases} \tag{1.8}$$

The transmission function of a source is measured by variation of the retarding potential U_0. Instead, in case of an electrostatic electron source, the source potential could also be varied.

1.2 Calibration-source requirements for KATRIN

Diverse electron sources are required for calibration and monitoring of the KATRIN spectrometer.

- First of all, nuclear standard sources are essential for continuous monitoring of the retardation potential U_0. An electron source based on condensed $^{83\mathrm{m}}Kr$, providing high stability and intensity and isotropically emitting conversion electrons, was developed by B. Ostrick (Universität Münster) [Ost09]. A solid $^{83}Rb/83\mathrm{m}Kr$ source is the scope of the dissertation of M. Zboril [Zbo] (Universität Münster / ASCR Prag).

  The K-shell conversion line of Krypton exhibits a natural width of $\Gamma = 2.7\,\mathrm{eV}$. This is sufficient for monitoring, but for detailed studies of the transmission properties of the MAC-E filter, the energy spread of a calibration source is required to be in the order of or smaller than the resolution.

- Unlike an ideal *MAC-E* filter, a real instrument like the KATRIN main-spectrometer shows inhomogeneous electric and magnetic fields across the diameter of its analyzing plane. The KATRIN main-spectrometer has a radius of 4.9 m. Over this large distance with the electrodes mounted on the hull, the spectrometer eventually shows an electric potential depression in its interior.

  The electromagnetic design of the main spectrometer is discussed in detail in [Val04], [Hug08] and [Val09]. Despite all improvements, according to these investigations the spectrometer shows an electric potential depression of $\Delta U = 1.04\,\mathrm{V}$ [Zac09] in the analyzing plane. Since the electric potential depression is radially dependent, the electron starting radius, corresponding to a guiding magnetic field line, affects the transmission function. To take the effect of this field depression into account

[4] For a derivation see [Val04].

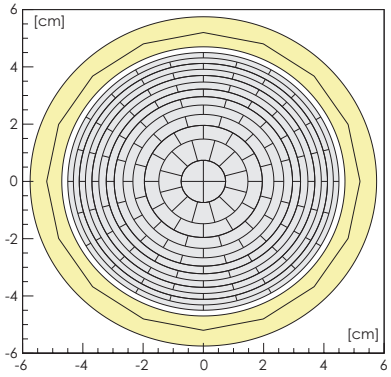

Figure 1.5: Pixel layout of the KATRIN final plane detector, illustration taken from [Val09].

during the analysis of the measured β-spectrum, the electron detector, is radially segmented (see fig. 1.5). A non compensated transmission function in comparison is shown in figure 1.6. The response of each of these segments has to be measured, thus a calibration source, that emits electrons on distinct positions and scans the flux tube transversally, is required.

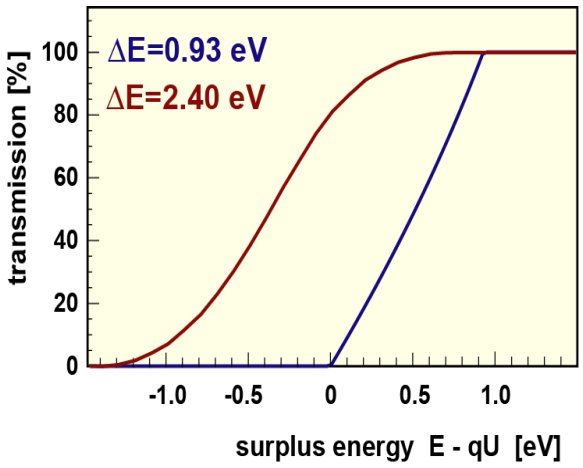

Figure 1.6: Results of a Monte Carlo simulation, including potential and magnetic field inhomogeneities $\Delta U \approx 1.2\,\mathrm{V}$ and $\Delta B \approx 0.4\,\mathrm{G}$, figure taken from reference [Dun]

- Like the electric potential, the magnetic field also shows a depression of $\approx 10\,\%$ in the analyzing plane. Thus calibration sources are required to cover the full anglar spectrum of $\theta_{\mathrm{solenoid}}$ at the magnet.
- At KATRIN the retarding potential U_0 is applied to the tank itself

and fine tuned with an inner wire electrode close to the tank wall. Due to small scale electronic structures of the wire electrode, electrons with larger angles, passing the spectrometer on outer trajectories, may suffer from the effect of early retardation. A pulsed, angular selective source would allow the investigation of this effect via time of flight (tof) measurements, see [Val09].

To summarize, complementary to nuclear standard monitoring sources, a pulsed, angular-selective, electrostatic calibration source, scanning the magnetic flux tube, was to be developed and investigated within the scope of this thesis.

Chapter 2

Essentials

Before discussing electron sources in detail, this chapter provides a basic toolset and essential information for the discussion. Beginning with the benefits of photoelectron sources, the emphasis of the first two sections lies on properties of these sources and the requirements on material and light source. The newly developed electron sources were tested at the Mainz Spectrometer, which is discussed in section 2.3. The chapter closes with a summary of employed simulation tools, used to investigate the electron source properties.

2.1 Electron source principles

There are several implementations to construct electron sources. One important basic element, describing an electron source, is the physical process that provides electrons. The three most common techniques, amongst other methods, are :

- thermionic emission
- field emission
- the outer photoelectric effect

Among these, the last named outer photoelectric effect offers key benefits, that are making it favorable:

- Since the outer photoelectric effect happens instantaneously[1], by using a short pulsed light source with high repetition rates, e.g. $f \approx 1\,\mathrm{kHz}$ and pulse lengths of $5\,\mathrm{ns} \leq \tau_{\mathrm{pulse}} \leq 200\,\mu\mathrm{s}$, a photoelectron source is able to create timed bursts of electrons, a valuable tool for time-of-flight (TOF) measurements.

[1] in the relevant time scale

- The kinetic starting energy E_{start}, which the electron gains, is independent of the intensity I_{inc} of the incident light, but constrained to the light source wavelength λ by

$$E_{\text{start}} = \frac{h \cdot c}{\lambda} - \Phi_{\text{metal}} \tag{2.1}$$

  with the metal work function Φ_{metal}. Small starting energies E_{start} and thus sharp electron energy distributions can be obtained by choosing a properly suited light source with a narrow emission spectrum matching closely the work function. This matching will be important for the discussed electron sources and results in small longitudinal and transversal energies of the photoelectrons ($E_{\parallel}$ and $E_{\perp}$).

The outer photoelectric effect is therefore used in this work to create pulsed, monoenergetic electrons and was utilized in all four electron sources, discussed in this document.

2.2 Electron sources based on the photoelectric effect

2.2.1 The light source

Photoelectron sources basically require a light source and an illuminated material. Generally solid metals serve as the cathode material, set on a constant negative potential to repel and accelerate photoelectrons. The work function Φ of most metals and alloys averages around 3 eV to 5 eV, depending on composition, surface and structure, see table 2.1.

Deuterium lamps

As can be seen from equation 2.1 for most elements only UV-light possesses sufficient energy to produce photoelectrons[2]. A deuterium lamp as it is currently in use at the pre-spectrometer electron gun at the *KIT* Karlsruhe, for example, is a suitable light source. The lamp emits UV-light with a continuous spectral range of about

$$185\,\text{nm} \leq \lambda_{\text{deut}} \leq 350\,\text{nm}$$

at high intensities, see [Hug08]. The drawback of deuterium lamps are the necessity of enhancements, like wavelength filters and choppers, in order to create narrow-band UV-light pulses.

[2] The rare multiphoton absorption is disregarded

Lasers

Lasers are the next option. For example a *KrF excimer* laser or a *frequency quadrupled Nd:YAG* laser can produce photoelectrons, with their corresponding wavelengths and photon energies of

$$\lambda_{\mathrm{KrF,excimer}} = 248\,\mathrm{nm} \quad \leftrightarrow \quad E_{\mathrm{KrF,excimer}} = 5.00\,\mathrm{eV}$$
$$\lambda_{\mathrm{Nd:YAG,quad}} = 266\,\mathrm{nm} \quad \leftrightarrow \quad E_{\mathrm{Nd:YAG,quad}} = 4.66\,\mathrm{eV}.$$

Lasers combine monoenergetic output of high power, narrow beam profiles and the possibility of precisely timed pulses as their paramount advantages. Drawbacks are, besides high costs, that application of a laser implies several technical difficulties, especially for the intended use at the Mainz spectrometer. Their intensity needs to be attenuated by several orders of magnitude, otherwise the large number of created electrons will cause damage to the *Si* PIN detector. Laser applications also involve safety precautions that may constrain operation in the laboratory during measurements.

Table 2.1: A list of metals and their work functions Φ [Lid08].

Element	Φ / eV	Element	Φ / eV	Element	Φ / eV
Ag	4.52-4.74	Al	4.06-4.26	As	3.75
Au	5.1-5.47	B	≈ 4.46	Ba	2.52-2.7
Be	4.98	Bi	4.34	C	≈ 5
Ca	2.87	Cd	4.08	Ce	2.9
Co	5	Cr	4.5	Cs	2.14
Cu	4.53-5.10	Eu	2.5	Fe	4.67 - 4.81
Ga	4.32	Gd	2.90	Hf	3.9
Hg	4.475	In	4.09	Ir	5.00-5.67
K	2.29	La	3.5	Li	2.93
Lu	≈ 3.3	Mg	3.66	Mn	4.1
Mo	4.36-4.95	Na	2.36	Nb	3.95-4.87
Nd	3.2	Ni	5.04-5.35	Os	5.93
Pb	4.25	Pd	5.22-5.6	Pt	5.12-5.93
Rb	2.261	Re	4.72	Rh	4.98
Ru	4.71	Sb	4.55 - 4.7	Sc	3.5
Se	5.9	Si	4.60-4.85	Sm	2.7
Sn	4.42	Sr	≈ 2.59	Ta	4.00 - 4.80
Tb	3.00	Te	4.95	Th	3.4
Ti	4.33	Tl	≈ 3.84	U	3.63 - 3.90
V	4.3	W	4.32 - 5.22	Y	3.1
Zn	3.63 - 4.9	Zr	4.05		

Light emitting diodes

Light emitting diodes (*LEDs*) represent a safe, easy to handle and comparatively inexpensive light source. Although the first blue light-emitting diode had been realized in 1971, it took until the late 90s for blue light-emitting diodes to become widely available. They represent a common light source which offers a broad spectrum of applications. Since a few years the implementation of *aluminum gallium nitrides* is common to push the *LEDs'* spectra into the ultraviolet regime below 300 nm. Nowadays there are several commercial products of *UV-LEDs* on the market. These UV-diodes are usually applied for therapeutic, medical, biological and chemical purposes and diagnoses. Due to the lethal effect of UV light on microorganisms the LEDs can be used for disinfection and sterilization devices.

In contrast their use in research, e.g. for photoelectron production, is a rather novel application. The general advantages of *UV-LEDs* are their versatility and ease of use, whilst providing narrow-band light with a typical full width at half maximum (*FWHM*) of $\Delta\lambda = 15\,\mathrm{nm}$, the possibility of pulsing short light bursts[3] and reduced cost in comparison.

Their main disadvantages are low maximum optical power output of about

$$150\,\mu\mathrm{W} \leq P_{\mathrm{max}} \leq 400\,\mu\mathrm{W}$$

and an inferior beam profile. Concerning the KATRIN experiment, the application of UV-LEDs for photoelectron production was first tested at a planar plate electron source (section 3.1). For the electron sources discussed in this thesis the inferior LED power output is less relevant since the emphasis was on the production of single photoelectrons with well-defined properties. In contrast the benefits, like the ease of use, the possibility of creating fast timed pulses with frequencies of the order of kHz and low cost led to the application of *UV-LED*s for the electron sources, presented in chapter 4 and 5. A detailed discussion of photoelectron production with UV-LEDs can be found in [V+09].

2.2.2 The *UV-LED*s: *T9B25C* and *T9B26C*

Among the comparatively small assortment of UV-LEDs on the market, the *T9B26C* from *Seoul Optodevice Co., Ltd.*, e.g. see figure 2.1, with the shortest provided wavelengths and highest optical power output were chosen. Their central peak wavelengths are

- $\lambda_{\mathrm{T9B25C}} = (255 \pm 15)\,\mathrm{nm}$
- $\lambda_{\mathrm{T9B26C}} = (265 \pm 15)\,\mathrm{nm}$

[3] within the scope of this thesis, bursts of $\tau = 20\,\mu\mathrm{s}$ were commonly used throughout experiments, the shortest measured pulse-length was $\tau = 5\,\mathrm{ns}$

Figure 2.1: The T9F26* UV-LED, equipped with a flat lens, equivalent to a *T9B26C* only with lower power output

equivalent to the wavelength of a *Nd:YAG* laser. The manufacturer provides different built-in lens optics for the *LEDs*. The optical power output P_{diode} at the maximally allowed DC forward current $I_{\text{FW}} = 20\,\text{mA}$ amounts to:

- $P_{\text{T9B25C}} = 150\,\mu\text{W}$
- $P_{\text{T9B26C}} = 400\,\mu\text{W}$

According to the data sheets, the *T9B26C* diode provides a considerable higher intensity and is hence favorable for most applications, as long as wavelength properties are secondary.

The optical spectrum

Due to the lack of precise information about the emission characteristics, e.g. wavelength spectra and pulse properties development, investigations of these were essential.

To determine the exact central peak wavelength λ_{cen} and full width at half maximum *FWHM*, spectra of both LEDs were measured. A grating spectrometer (*Jobin Yvon H10*) served as the monochromator and a *Si* PIN photodiode (*Hamamatsu S3590-06*) as the light detector with a sufficient detection efficiency in the relevant wavelength regime. The components were placed in a light-proof metal casing for suppression of environmental effects. The spectra of both *UV-LEDs* were measured and are provided in figure 2.2. The *LEDs* also emit a small fraction of light in the blue regime at about $\lambda_{\text{LED}} \approx (525 \pm 25)\,\text{nm}$, that is negligible since the according photon-energies are too low for photoelectron production.

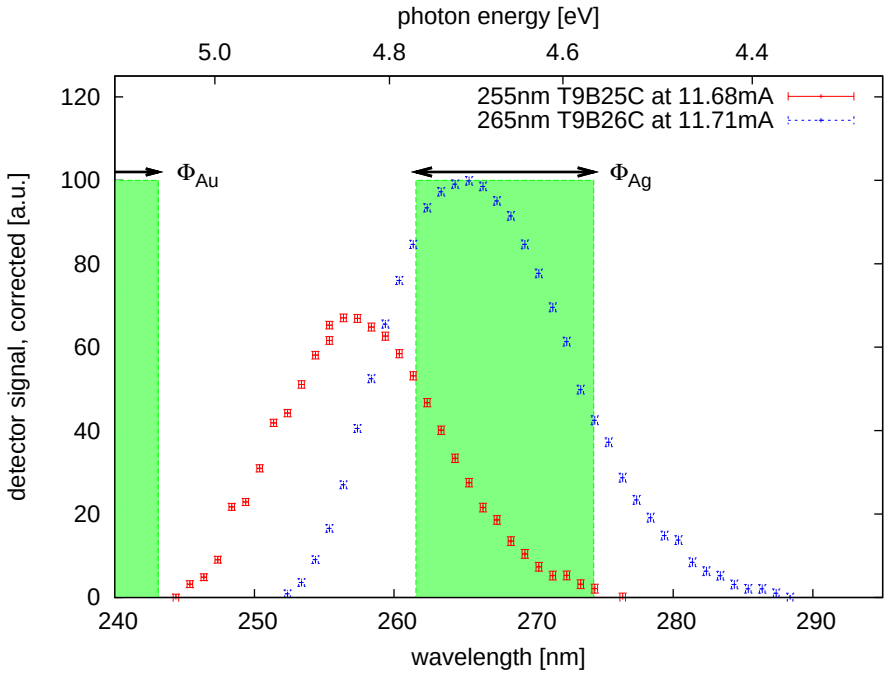

Figure 2.2: Measured spectra of both *UV-LEDs*, the *T9B25C* and *T9B26C*. While the diodes are operated at comparable forward currents I_{FW} the T9B26C shows a higher intensity in accordance with its higher optical power output $P_{\mathrm{opt}} = 400\,\mu\mathrm{W}$. It is obvious, that neither spectrum reaches up to the work function of gold $\Phi_{Au} = 5.1\,\mathrm{eV}$. Additionally the *T9B26C* is expected to possess a higher efficiency at a silver cathode, with an approximate work function $4.52\,\mathrm{eV} \leq \Phi_{\mathrm{Ag}} \leq 4.74\,\mathrm{eV}$.

Notes on calibration and uncertainties of the UV-LED spectra are provided in the appendix (B).

Operation in pulsed mode

The diodes are designed to work at DC currents of up to $I_{\mathrm{FW}} = 20\,\mathrm{mA}$. For tests and measurements conducted within the scope of this thesis, the employed voltage sources and frequency generators supplied up to 10 V. Therefore a safety resistor was used in series with the UV-LED. The I-V characteristics were determined, with the result that the resistor should be $R \geq 90\,\Omega$ for $I_{\mathrm{FW}} \leq 2\,\mathrm{mA}$.

Besides the constant current operation, the diodes can also be used in a pulsed mode. The data sheets name a maximum forward current of $I_{\mathrm{FW}} = 100\,\mathrm{mA}$ at duty cycles of 1 % and less, since a lowered power output also reduces thermal damages. The pulsed mode gives some advantages over the

constant current mode.

1. The signal to noise ratio is improved at the cost of overall intensity.
2. It is possible to employ the spectrometer in a time-of-flight mode. Typical pulse lengths for the investigation of the Mainz *MAC-E* filterin the TOF-mode span a wide range of $40\,\text{ns} \leq \tau \leq 200\,\mu\text{s}$.

The overall drawbacks are:

1. The reduced intensity, with corresponding low count rates in the spectrometer. This decreases the luminosity and increases measurement time.
2. The necessity of a fast data acquisition, e.g. a flash analog-to-digital converter (FADC). S. Streubel developed such a data acquisition system in 2009 within the scope of his diploma thesis [Str09].

This pulsed mode also requires an adaption of the safety resistor. This will become relevant for measurements in chapter 5.

2.2.3 Cathode materials

The drawback of the broad spectral emission[4] of such a UV-LED in comparison to that of a laser can be partially compensated by matching cathode metal and LED spectrum. Then only the high-energetic tail of the spectrum will create photoelectrons. The choice of an appropriate cathode material is important, since Φ_{metal} defines the electron starting-energy distribution ΔE_{start} (equation 2.1).

The work function Φ of metals depends on composition (elements), surface structure[5] and surface orientation. Heating, cooling, tempering and adsorbates like oxygen affect the surface structure and potential. Also structural surface damage, e.g. due to ion bombardment, and even the atomic density and layer thickness affect the work function (e.g. Smoluchowski effect, see reference [Smo41]).

As listed in table 2.1, the work function of metals is well known. Most of these work function measurements took place between 1950 and 1980. Discrepancies for the work function measurement of gold for example are explained by mercury contamination due to the application of mercury diffusion pumps and other effects.

Notable metals

In the case of the two electron sources, developed in the course of this thesis, the metal will be evaporated on the electron source surface. The work

[4] LED *FWHM* amounts $\Delta\lambda \approx 15\,\text{nm}$

[5] crystalline, polycrystalline, amorphous

Table 2.2: *From [Val09]*: Work function values for selected metals, gathered from various references, as listed in the last column. Some references do not give error bars for the measurements. There are notable differences in the values obtained by photoelectric or contact potential measurements, as well as between different crystalline orientations of monocrystals and for polycrystalline samples. The discrepancy between the work function of gold obtained with the contact potential difference method (1 and 2) is attributed [H$^+$66] to a contamination of the gold sample with mercury in those experiments using mercury pumps.

No.	material (cryst. direction)	method / remarks	Φ [eV]	reference
1	Au	contact potential diff.	5.22 ± 0.05	[H$^+$66]
2	Au	contact potential diff.	4.83 ± 0.02	[A$^+$59]
3	Au (polycryst.)	photoelectric	5.1 ± 0.1	[Eas70]
4	Au (100)	**photoelectric**	5.47	[Wea81]
5	Au (110)	**photoelectric**	5.37	[Wea81]
6	Au (111)	**photoelectric**	5.31	[Wea81]
7	Au	**after exposure to air**	4.2	[Sav95]
8	Ag (100)	**photoelectric**	4.22 ± 0.04	[C$^+$82]
9	Ag (110)	**photoelectric**	4.14 ± 0.04	[C$^+$82]
10	Ag (111)	**photoelectric**	4.46 ± 0.02	[C$^+$82]
11	Ag (polycryst.)	**photoelectric**	4.0 ± 0.15	[Eas70]
12	Cu (polycryst.)	**photoelectric**	4.65 ± 0.05	[Eas70]
13	Cu (100)	**photoelectric**	4.59	[Wea81]
14	Cu (110)	**photoelectric**	4.48	[Wea81]
15	Cu (111)	**photoelectric**	4.94	[Wea81]
16	Cu (112)	**photoelectric**	4.53	[Wea81]
17	Cr (polycryst.)	**photoelectric**	4.5 ± 0.15	[Eas70]
18	Fe (polycryst.)	**photoelectric**	4.5 ± 0.15	[Eas70]
19	Ni (polycryst.)	**photoelectric**	5.15 ± 0.1	[Eas70]
20	stainless steel 1.4429 DIN, 316LN AISI/SAE		4.4 ± 0.2	[Pic92]
21	stainless steel 302 AISI/SAE	**photoelectric** clean surface	4.75	[W$^+$99]
22	stainless steel 302 AISI/SAE	**photoelectric** varying grades of oxygen contamination	4.35-4.55	[W$^+$99]

function Φ of this amorphous and thin surface is required to be close to the photon energy of a *T9B26C* LED, $E_\mathrm{p} = (4.68 \pm .15)\,\mathrm{eV}$. For the selection of an adequate cathode metal, the following aspects were examined

- the specific work-function,
- (potential) uncertainties and their effects on the work function,
- (potential) change of Φ_metal over time, e.g. due to exposure to air, and
- their machinability.

Among the wide range of materials, especially *Ag, Au, Cu, Cr, Fe, Ni* and *stainless steel* are notable. These materials can be used for high vacuum applications. Table 2.2 lists their work functions in dependence of surface crystalline direction and applied experimental method.

The noble metal gold makes an excellent cathode material, since it does not corrode under normal conditions unlike silver and copper. Φ_{Au} is well known and was measured to amount between

- $\Phi_{\mathrm{Au}} = 4.83\,\mathrm{eV}$ [A$^+$59] or $\Phi_{\mathrm{Au}} = 5.22(\pm.05)\,\mathrm{eV}$ [H$^+$66] for the contact potential difference method.
- $\Phi_{\mathrm{Au,100}} = 5.31\,\mathrm{eV}$ to $5.47\,\mathrm{eV}$ for the photoeffect, on a monocrystal [Wea81].

Referring to figure 2.2 it is expected, that photoelectrons can be produced with none of the used UV-diodes[6]. Photoelectrons seemingly from a gold surface were observed once in this work (section 4.2.2) but this measurement could not be reproduced. It is most likely, that a stainless steel surface was illuminated due to beam misalignment.

In contrast for the following cathode materials photoelectron production was validated.

- stainless steel, $\Phi_{\mathrm{st.steel}} \approx 4.4\,\mathrm{eV}$ (alloy),
- chrome, $\Phi_{\mathrm{Cr,poly}} = 4.5\,\mathrm{eV}$,
- silver, $\Phi_{\mathrm{Ag,poly}} = 4.0\,\mathrm{eV}$, and
- copper, $\Phi_{\mathrm{Cu,poly}} = 4.65\,\mathrm{eV}$.

Thereby the latter two, *Ag* and *Cu*, tend to corrode, which affects the work function (over time). The photoelectrons are created under vacuum conditions, thus no such change is expected throughout the measurement.

For a vapor deposited metal, as applied at the two sources discussed in chapter 4 and 5, properties like structure, adsorbates / impurities and layer thickness, can only be estimated with high uncertainties. Therefore we chose to select a suitable material, usually silver or copper, and estimate the starting energy distribution, as applied in reference [V$^+$09] for the investigation of time-of-flight measurements. This procedure showed reasonable results.

After all, in order to understand and reduce the starting energy distribution of photoelectrons and improve electron yields, further investigations of metal layers and densities are an inevitable task.

2.3 Mainz spectrometer

The two electron sources developed in the scope of this thesis (chapter 4 and 5) are intended to be operated at the KATRIN main spectrometer (figure 2.3). For testing purposes in ultra-high vacuum and high magnetic fields,

[6] The depicted work function range represents values for photoelectron production from gold. Impurities and adsorbates are not regarded.

these newly developed sources were implemented at the Mainz *MAC-E* filter, the spectrometer of the former Mainz neutrino experiment and predecessor of KATRIN.

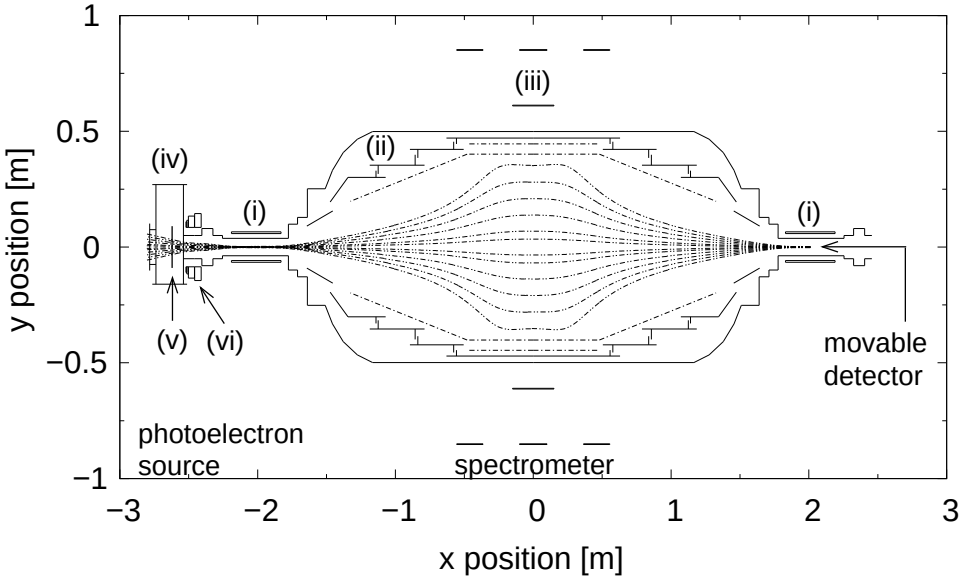

Figure 2.3: Schematic of the experimental setup to test the photoelectron source. From left to right: vacuum chamber with photoelectron source, electrostatic filter with magnetic adiabatic guiding and detector. The details shown in the sketch include: (i) two superconducting solenoids to produce the magnetic guiding field of the *MAC-E* filter(ii) the electrode configuration comprising a vacuum tank on ground potential and an inner high-voltage electrode system, (iii) field-shaping air coils, (iv) the additional vacuum chamber (see Fig. 2.5), (v) the stainless steel cathode and (vi) an additional water-cooled coil for local enhancement of the magnetic field strength. Magnetic field lines connecting the photocathode and the detector are indicated as dashed curves. The analyzing plane of the spectrometer at $x = 0$ is defined by the maximum of the retardation potential $|U_{\mathrm{spec}}|$ coinciding with the minimum magnetic field strength B_{min} (from [V$^+$09]).

The vessel geometry is similar to but smaller than the KATRIN spectrometers, consisting of a large cylinder of about 4 m length, with a superconducting solenoid at each end. These magnets create magnetic field strengths of $B_{\mathrm{max}} = 6\,\mathrm{T}$ at their center at $z = \pm 2.01\,\mathrm{m}$ (z=0 describes the analyzing plane). Full metal electrodes and wire modules, lying on a difference voltage are implemented on the inside of the metal hull. This implementation shapes the electric field and suppresses electron and ion background caused by radioactive decay as well as by interaction of cosmic ray particles within the hull.

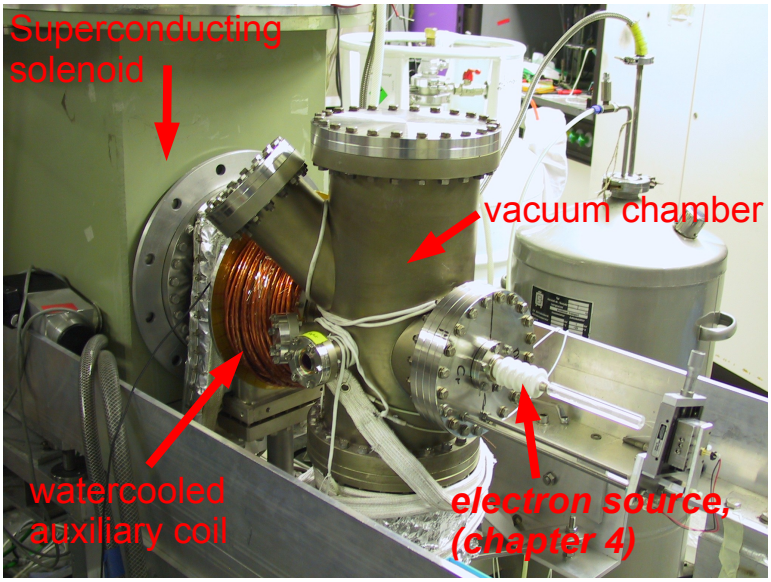

Figure 2.4: Photograph of the vacuum chamber and entrance magnet at the Mainz *MAC-E* filter.

Vacuum chamber

A vacuum chamber, see figure 2.4, is attached to the entrance of the spectrometer. A shutting valve separates the chamber from the spectrometer and enables venting of the chamber. Figure 2.5 schematically shows the design of the cylindrical chamber. The chamber contains four *CF 40* ports in the y-z-plane, usually equipped with window-flanges, as well as a fifth CF100 flange at a 40 ° angle with respect to the vertical direction. Besides an usually mounted window or blind flange, the CF100 flange may alternatively carry a wire scanner with the following purpose:

The constellation of the photo cathode on negative potential U_{source}, the analyzing plane on negative potential U_{spec} and a strong magnetic field in between creates a Penning trap, depicted in figure 2.6. Electrons with energies $E_{\parallel} < e \cdot U_{\text{source}}$ and $E_{\parallel} < e \cdot U_{\text{spec}}$ can become trapped within these fields. These electrons will eventually create background as well as discharges within the spectrometer. To decrease the number of trapped electrons, the wire scanner swipes a metal wire through the Penning trap. A detailed discussion on Penning traps and the wire scanner is found in reference [Val09]. During the measurements discussed in the following a stationary wire was permanently installed through the central flux tube of this trap.

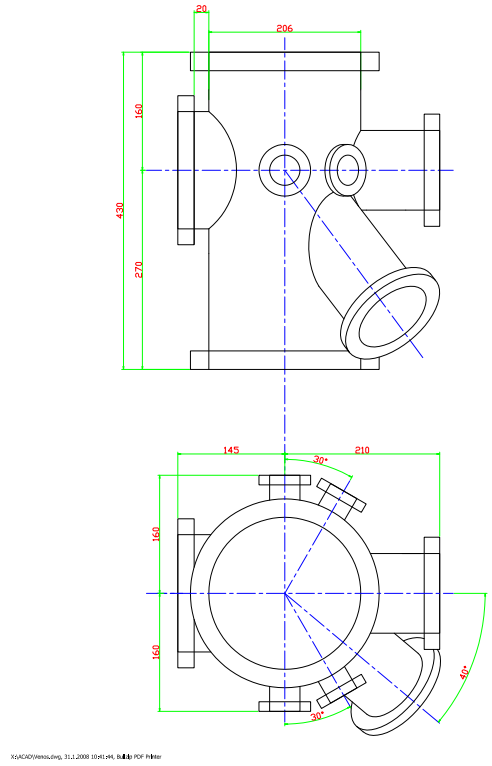

Figure 2.5: The entrance vacuum chamber, side- and top-view. This chamber was used to hold the photoelectron sources.

Detector

At the spectrometer exit to detect the electrons, a Hamamatsu silicon PIN diode is mounted on a mobile sledge. The detector position corresponds to the imaged magnetic flux tube. By adjusting the position the imaged area is enlarged or decreased.

Air coils

Besides the superconducting solenoids, magnetic air coils define and shape the magnetic flux tube in the analyzing plane. The outer magnetic flux tube can hence be compressed, as seen in figure 2.3, and the magnetic field strength in the analyzing plane of the spectrometer B_{ana} is defined. Since the spectrometer resolution directly corresponds to the ratio of the B-field in the analyzing plane B_{ana} and at the solenoid B_{solenoid}, the width of the transmission function can be set. This is basically the resolution ΔU_{res} in

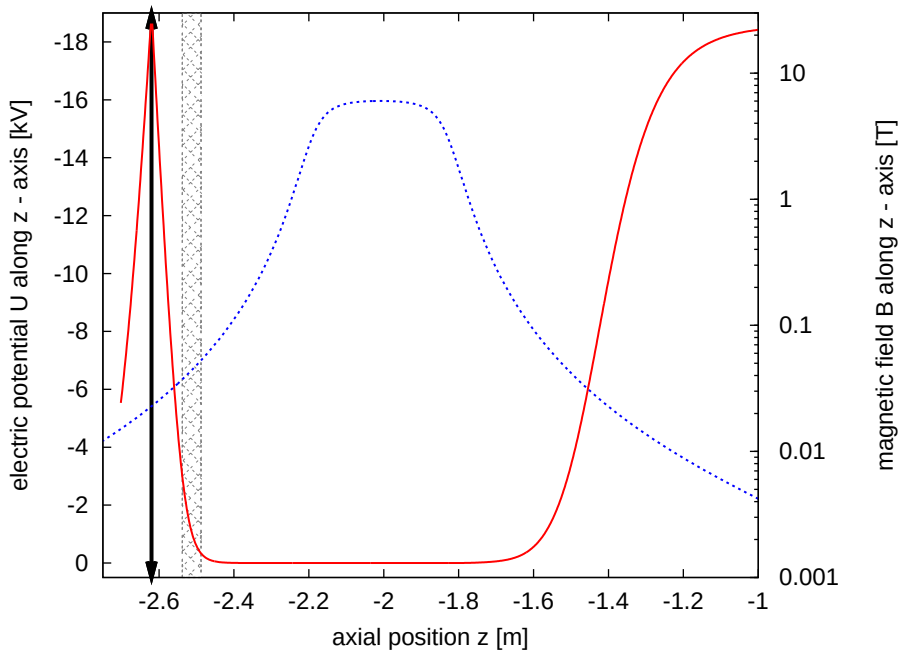

Figure 2.6: Illustration of a Penning trap between a planar plate (black arrow at $z = -2.618\,\mathrm{m}$) and spectrometer, both on $U_{\mathrm{tot}} = U_{\mathrm{spec}} = -18.6\,\mathrm{kV}$ potential. Electrons become trapped in the potential well (red) and guided by the high magnetic field (blue, logarithmic). The position of the wire scanner, wiping through the trap, is depicted in gray.

dependence of the spectrometers electric field (compare eq. 1.7).

$$\Delta U_{\mathrm{res}} = \frac{B_{\mathrm{ana}}}{B_{\mathrm{solenoid}}} \cdot U_{\mathrm{source}} \tag{2.2}$$

While the resolution should be as small as possible for tritium decay measurements, it might be advisable to select a broad resolution for the investigation of the properties of the various electron sources.

Additional coils

Two further coils are employed at the spectrometer. The first is a water-cooled auxiliary coil (labeled as (vi) in figure 2.3), with the purpose of additionally increasing the magnetic field at the vacuum chamber. By increasing the magnetic field, the field lines at an electron source in the chamber are compressed and the number of field lines, intersecting with the source is increased. Basically the area of the source, that is being imaged onto the detector, is decreased with an increased magnetic field. A photograph of the spectrometer including the auxiliary coil is provided in figure 2.4. The

geometry of this 'hand-made' coil can only be approximated, which leads to uncertainties concerning simulations with the according magnetic field.

The earth magnetic field also has to be compensated, hence earth-field-compensation coils (EFC) enable shifting of the magnetic flux tube passage within the spectrometer. Shifting of the flux tube also improves detector alignment. At the beginning of a measurement period the EFC calibration serves to ensure, that the electron source is completely imaged on the detector.

2.4 Simulation tools

In order to analyze and understand properties of electron sources, the source geometries are simulated and their fields and according electron trajectories are computed. The employed tools were mainly developed by Dr. Ferenc Glück (Forschungszentrum Karlsruhe) and further processed by Sebastian Vöcking (Universität Münster). These programs are only briefly discussed in this section, for detailed discussion see references [Val04], [Vöc08] and [Hug08].

Magnetic field calculation

The programs *magfield2.c* and *magfield3.c* were employed for calculations of the magnetic field. *Magfield2.c* calculates the magnetic field of axially symmetric coil configurations, while *magfield3.c* is able to perform field calculations with different local coil symmetry axes. Therefore the magnetic field is first computed locally. Then the field values are transformed into the global coordinate system.

The programs use two different methods for field computation:

- The method of *elliptic integrals* is used to accurately calculate the magnetic field. This method can calculate the magnetic field everywhere, but is rather slow.
- The second method, the use of *Legendre polynomial expansion*, is less accurate, but very efficient and fast, hence it is employed at larger distances from the coil.

Electric field calculation

For electric field calculations the program *elcd3_ 2.c* applies the boundary element method for axially symmetric geometries, consisting of solid electrodes and wires. After discretization of the geometry into small sub elements, the program computes charge densities which are assumed to be homogeneous for a given sub element. This method has the advantage that it is able to compute the electric field of smallest substructures that are part of larger

geometries in contrast to the common used finite difference method. A comparison of both methods can be found in [Val04].

Electron tracking

After the computation of electric and magnetic fields the routine *traj.c* performs microscopic tracking of electrons. The calculation is based on relativistic equations of motion. The program takes advantage of the electrons cyclotron motion and divides the motion into n_{period} circulations, which are likewise divided into n_{timestep} cyclotron steps. For computations at *MAC-E* filters with distinct local magnetic field, this method is favorable over time step discretization. A huge benefit are the implemented control parameters, logging energy and adiabatic invariant errors and improving reliability of calculations.

Chapter 3

Established photoelectron sources at KATRIN

The two electron sources, discussed in this chapter, were not scope of this thesis. However they are briefly discussed to illustrate processes, which are fundamental for the newly developed sources. The first geometry is kept simple: a planar plate illuminated by ultraviolet light. A detailed discussion can be found at [Val09]. The second source is more subtle and includes illumination of a thin gold layer from behind the source. For more information, see references [Hug08] and [Frä07].

3.1 Planar plate photoelectron source

This source was created with the aim to fill and investigate a Penning trap similar to the one in between the two spectrometers of KATRIN [Val09]. Figure 3.1 shows a photo of the setup. This simple electron source consists of a round planar plate, made of stainless steel, $\oslash_{\text{plate}} = 18\,\text{cm}$ in diameter and $d_{\text{plate}} = 10\,\text{mm}$ thick. On the edge a circular frame with 6 mm radius avoids sharp edges, high electric fields and potential discharges. Stainless steel was chosen as the cathode material because of its easy handling and ready machinability, whilst possessing a work function $\Phi = 4.4(\pm.2)\,\text{eV}$ [Pic92], well matching the *T9B26C*.

The ellipsometry-vacuum-chamber containing the plate (section 2.3), is equipped with four windows. Two of these windows are UV-transparent (Suprasil / Sapphire) and allow the LED to illuminate the center of the plate from a 30° angle (see figure 3.2). At this distance and angle the illuminated spot metes about $2\,\text{cm}^2$. The area $9 - 14\,\text{cm}^2$ around the plate center is imaged on the detector. Thus in principle all photoelectrons can be imaged on the detector. This will not happen as not all electrons are able to pass the spectrometer.

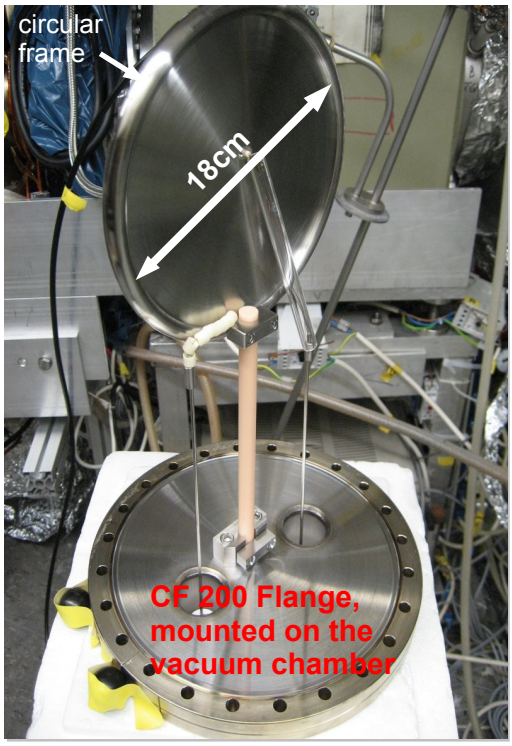

Figure 3.1: Photo of the planar plate electron source.

3.1.1 Simulations

Figure 3.3 shows the electromagnetic tracking of 1 eV surplus-energy electrons ($U_{\text{spec}} - U_{\text{source}} = 1\,\text{eV}$) with the planar plate electron source (section 3.1) in the Mainz spectrometer. The electrons are guided along the magnetic field-lines. One can observe the constriction of trajectories close to the solenoids and their broadening at the analyzing plane in the weak magnetic field. Since the electrons posses sufficient surplus energy all electrons started within a certain radius r manage to pass the spectrometer. Depending on the detector position some outer tracks will bypass the detector, the corresponding electrons will not be detected. By varying the detector-position, the imaged area on the plate surface is altered.

In the early phase of an electron trajectory the motion is determined by the electrostatic acceleration. With increasing energy $E_{\text{kin}}(\hat{x})$ and leaving the cathode, the magnetic field eventually becomes the dominant force. The

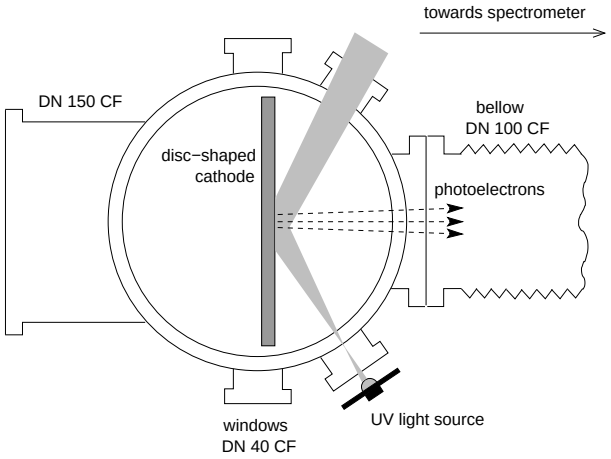

Figure 3.2: (from [Val09]) Sketch of the irradiation of the backplate with UV light from a UV LED. The schematic diagram (dimensions are not to scale) shows the top view of the vacuum chamber housing the disc-shape high voltage electrode of diameter $D = 180\,\mathrm{mm}$ and thickness $d = 10\,\mathrm{mm}$. The chamber is attached to the spectrometer via a bellow, indicated on the right-hand side of the drawing. Two of the four windows are made of UV-transparent material (sapphire and Suprasil, respectively) and thus allow to shine UV light from an external light source onto the electrode disc. Photoelectrons created at the stainless steel cathode will be accelerated by the strong electric field and guided by the magnetic field through the bellow towards the spectrometer.

angle θ, that describes the distribution between $E_\perp$ and $E_\parallel$, gains relevance:

$$\begin{aligned} E_{\mathrm{kin}} &= E_\perp + E_\parallel \\ E_\perp &= E_{\mathrm{kin}} \cdot \sin^2\theta \\ E_\parallel &= E_{\mathrm{kin}} \cdot \cos^2\theta \end{aligned} \tag{3.1}$$

There are various feasible expressions to determine the beginning of adiabatic guidance.

- First of all there is the adiabatic invariant, which is constant for adiabatic motion. A suitable expression is the magnetic moment

$$\mu = \frac{E_\perp}{B}. \tag{3.2}$$

  The magnetic moment for three electrons, started on different radii on the plate, is illustrated in figure 3.5. The magnetic moment strongly oscillates until after a distance of approximately 15 cm it observably starts to converge to a constant value, since the electric field strength and thus the acceleration of electrons decreases.

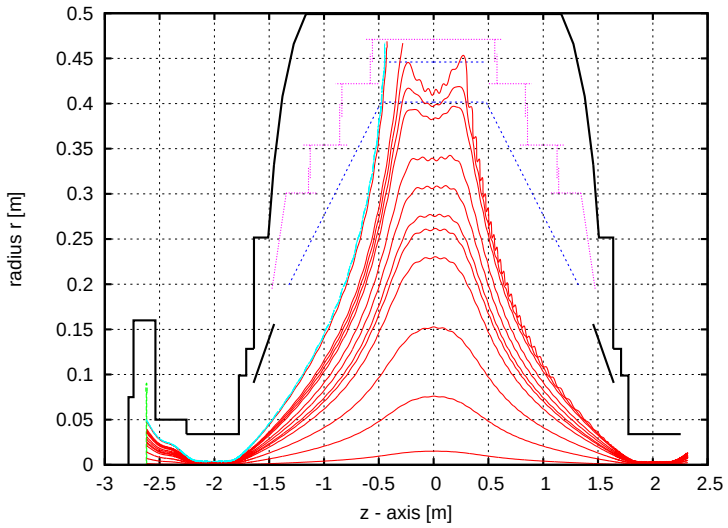

Figure 3.3: Electron trajectories passing the spectrometer with 1 eV surplus energy. The electrons were started on different radii r_0, where larger radii r_0 correlate to outer tracks. Besides the constriction of trajectories close to the magnets at $z = \pm 2.01\,\mathrm{m}$ one can observe the air coil effect, compressing the outer magnetic field in the analyzing plane. The trajectories of electrons on larger radii in these magnetic field and close to or passing the wire modules become very erratic, small variations of environmental parameters can immensely affect the trajectories. The trajectories in light blue depict electrons, that are guided on outer magnetic field lines, passing the electrodes. With longitudinal energies $E_{\parallel} < q \cdot U_{\mathrm{spec}}$, respectively U_{source}, at cathode and electrode and guided along the magnetic field lines, these are trapped.

- Figure 3.6 shows, that in case of this source, the magnetic field dominates the electric after a distance of up to 10 cm. This distance depends of the local electromagnetic field constellation of $|E|$, $|B|$ and an α between the two corresponding field vectors (figure 3.4).

- Thirdly, to illustrate the process, trajectory plots (figure 3.7) show how electrons follows the magnetic field lines. Although adiabatic motion starts at distances of approximately $z > 15\,\mathrm{cm}$, the electron roughly follows the magnetic field lines from the first few cm.

This demonstrates that the transition to adiabatic motion is a smooth process. For a different geometry the transition is illustrated in chapter 5. A more elaborate investigation of transitions from non-adiabatic motion to adiabatic guidance is discussed in [Hug08].

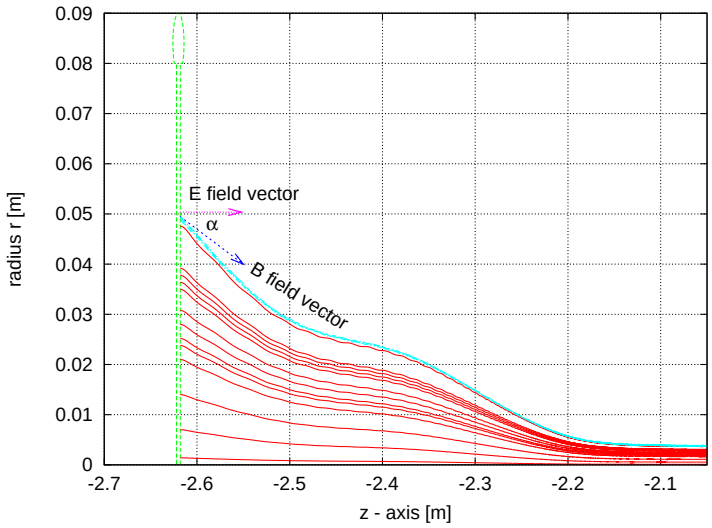

Figure 3.4: An enhanced illustration of figure 3.3, showing the beginning of electron trajectories within the ellipsometry chamber. Accelerated by the cathode (green), the electron trajectories (red) are guided towards the magnet at $z = -2.01\,\mathrm{m}$. This figure demonstrates the dependence of $\alpha(r)$, as the α increases analog with the radius, due to the inhomogeneous magnetic field.

3.1.2 Distribution of θ

The angle θ of an electron at the entrance magnet is in the following depicted as $\theta_{\mathrm{solenoid}}$. Electrons with angles $\theta_{\mathrm{solenoid}} \leq 90\,^\circ$ are able to pass the entrance magnet, whereas electrons with larger angles are reflected due to negative longitudinal momenta (compare eq. 1.2). Figure 3.8 shows the distribution of the angle $\theta_{\mathrm{solenoid}}$ at the high magnetic field for this planar electron source. Using $\theta_{solenoid}$ is useful for describing the electrons. $\theta_{\mathrm{solenoid}}$ is relevant for the transmission function and time of flight and describes the relevant electron property in dependence of the magnetic field at the solenoid.

As can be seen in figure 3.8 the detected electrons gain angles of $\theta_{\mathrm{solenoid}} \leq 5\,^\circ$. This distribution is fine for an electron source with the purpose of filling Penning traps. In contrast calibration sources for KATRIN will require angular emission angle of at least

$$0\,^\circ \leq \theta_{\mathrm{solenoid}} \leq 90\,^\circ \tag{3.3}$$

to examine the magnetic field depression in the analyzing plane. Different realizations of an electron source are required, such as the pre-spectrometer electron gun as discussed in section 3.2.

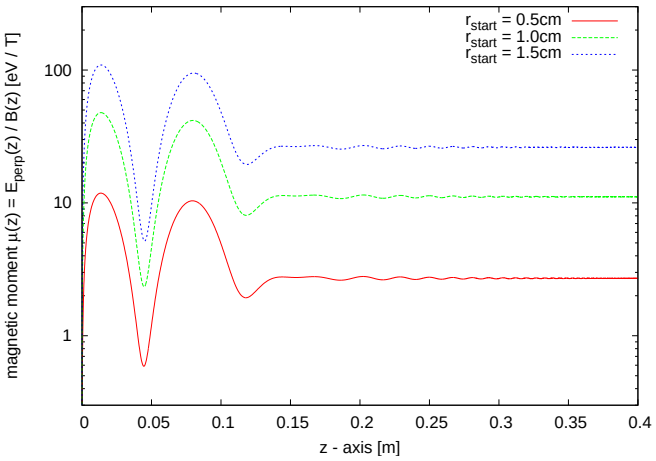

Figure 3.5: The magnetic moment of three electrons started on radii $r_1 = 0.5\,\mathrm{cm}$, $r_2 = 1.0\,\mathrm{cm}$ and $r_3 = 1.5\,\mathrm{cm}$. The strong oscillation of the magnetic moment decreases with distance from the strong electric potential until at $z > 0.15\,\mathrm{cm}$ the magnetic moment observably converges to a constant value.

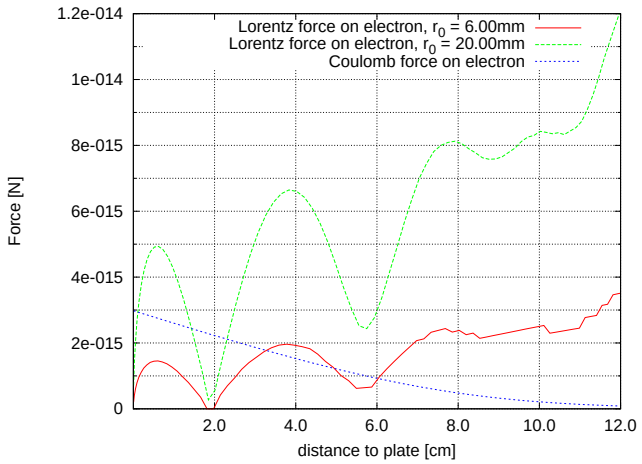

Figure 3.6: Comparison of Lorentz force (magnetic component) and Coulomb force on electrons in order to describe the transition to adiabatic motion. The electrons are emitted from the planar plane on a $U_{\mathrm{source}} = -18.6\,\mathrm{kV}$ potential. The blue line depicts the coulomb force, decreasing in distance from the cathode. The Lorentz force is displayed in red and green for two electrons, created on different starting radii r_0. Due to $F_{\mathrm{B}} = q \cdot (\hat{v} \times \hat{B})$ and the inhomogeneous magnetic field-line expansion, electrons created on outer radii gain larger amounts of transversal energies. In contrast electrons, started at the center of the plate $r_0 = 0$, will not gain any transversal energy, due to $\hat{E} \parallel \hat{B}$ for $(z = 0)$.

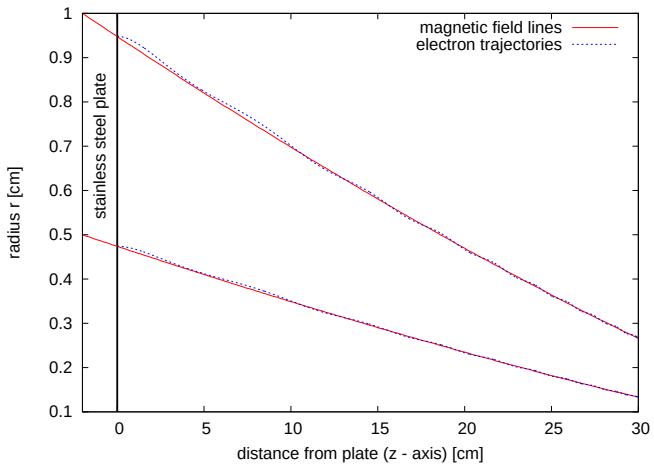

Figure 3.7: Illustration of trajectories of two electrons and corresponding magnetic field lines. The electron is accelerated along the electric potential. At sufficient kinetic energies the magnetic field dominates and guides the electron along magnetic field lines. Although adiabatic motion starts at distances of approximately $z > 15\,\mathrm{cm}$, the electron roughly follows the magnetic field lines from the first few cm on.

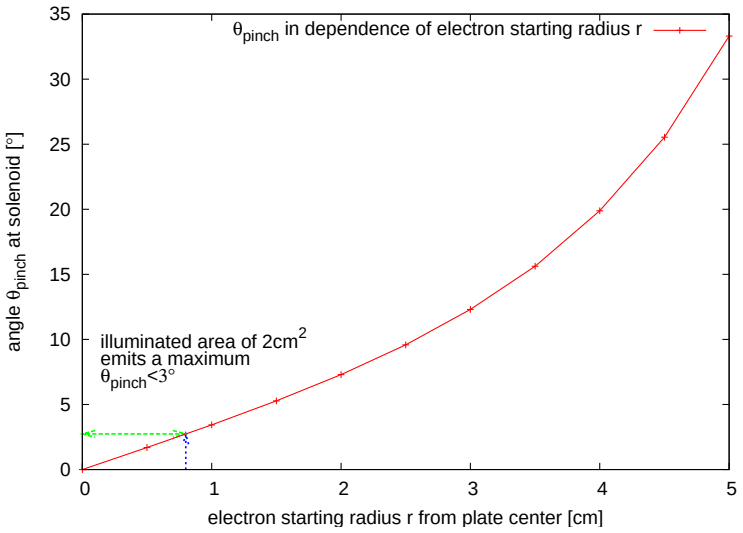

Figure 3.8: Planar plate electron source: The angle $\theta_{\mathrm{solenoid}}$ at the solenoid in dependence of the electron starting radius r_{start}. The illuminated area of approximately $2\,\mathrm{cm}^2$ (blue arrow) emits angles $\theta_{\mathrm{solenoid}} \leq 3\,^\circ$ (green arrow).

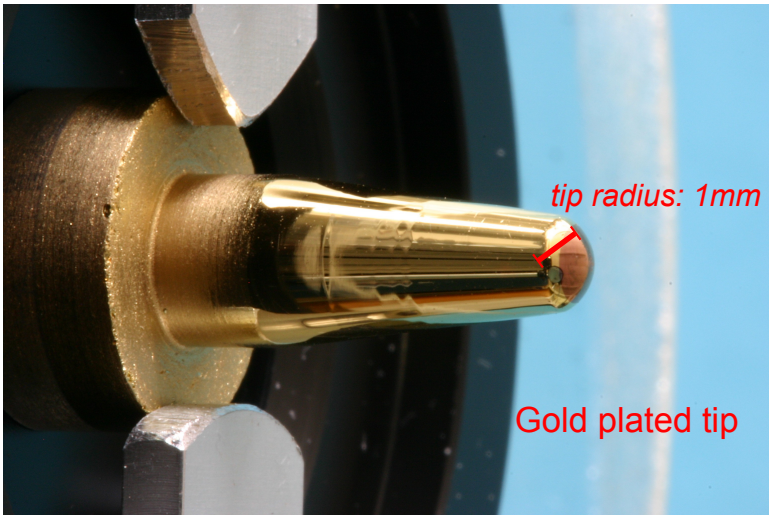

Figure 3.9: Picture of the pre-spectrometer electron source.

3.2 The Pre-Spectrometer Electron Gun

In order to gain transversal energies, electrons need to be accelerated in an electric field with an angle $\alpha \neq 0\,^\circ$ to the magnetic field. For higher θ_{solenoid} compared to those of the previous source, improved geometries are necessary. The current pre-spectrometer e-gun is a good example. It consists of an UV-transparent quartz tip with a curvature radius of $r_{\text{tip}} = 1\,\text{mm}$ which is plated with a gold layer, thin enough to transmit enough UV-light to create photoelectrons at the surface.

The workfunction of gold Φ_{Au} has been measured under several conditions, with multiple methods and for different crystalline orientations and configurations. Some measurements are listed in table 2.2.

The vapor deposited gold layer of the pre-spectrometer electron source is thin, amorphous and was certainly exposed to air. Additionally the surface was damaged by ion bombardment over time. It is hard to name an exact work function Φ_{egun}, without further knowledge, but also irrelevant, since this source is back-illuminated by a Deuterium lamp with a broad range spectrum $185\,\text{nm} \leq \lambda_{\text{Deut.}} \leq 400\,\text{nm}$ [Ham] equivalent to $6.7\,\text{eV} \geq E_p \geq 3.1\,\text{eV}$.

Electromagnetic and tracking simulations have been extensively performed for this setup in 2007 [Hug08]. An important outcome of these simulations is the correlation of the electron starting-radius r and the angle θ_{solenoid} at the center of the magnet for different surplus-energies, see figure 3.10. A similar plot for the planar plate electron source had been provided with figure 3.8

As figure 3.11 shows, the angular distribution of electrons created with

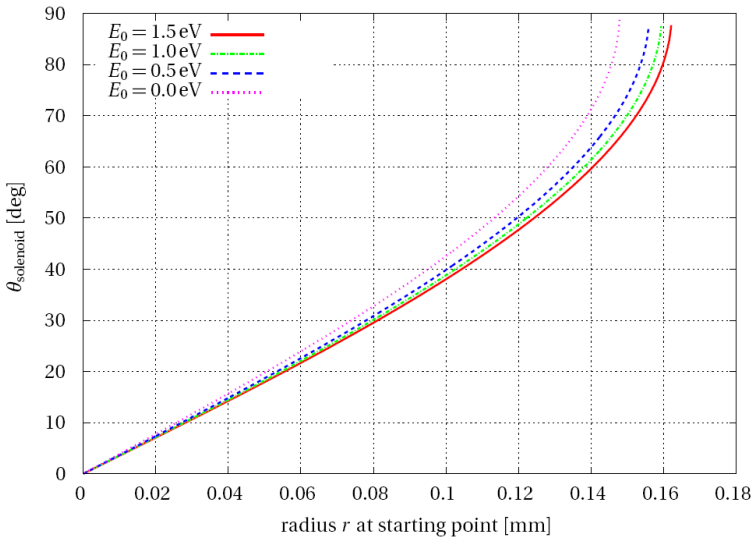

Figure 3.10: Illustration of the angular emission point dependence of $\theta_{\mathrm{solenoid}}$. Electrons are created on the surface of the cathode and accelerated by the electric field, perpendicular to the surface. Due to axial symmetry, the electron starting position is described by the radius r_{start}. Taken from [Hug08].

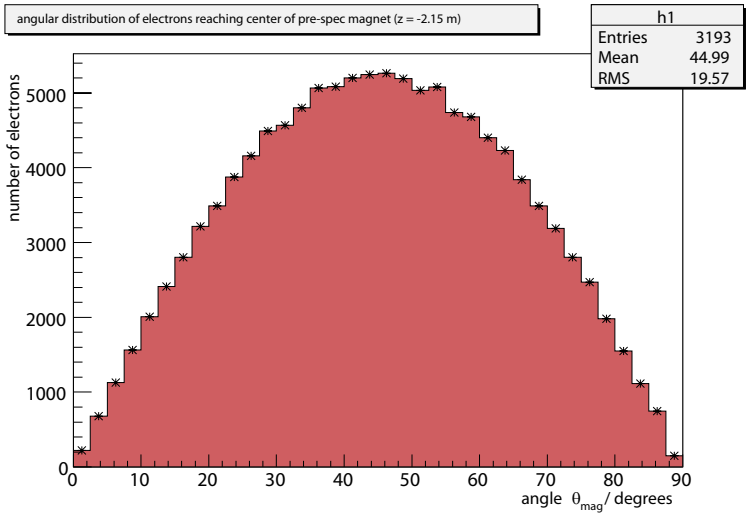

Figure 3.11: Angular distribution for the pre-spectrometer electron source at the center of the entrance magnet. Taken from [Hug08].

this electron gun ranges from $\theta_{\text{solenoid}} = 0\,^\circ$ to up to $\theta_{\text{solenoid}} = 90\,^\circ$, with only few electrons at both extremes, i.e. a non-isotropic angular distribution.

This source emits electrons of angles $0\,^\circ \leq \theta_{\text{solenoid}} \leq 90\,^\circ$ due to the curved surface structure. It is currently applied at the pre-spectrometer at Karlsruhe for calibration purposes. More detailed investigations were achievable with improved geometries, that do not emit electrons 'isotropically' distributed, but with a pre-defined angle θ_{solenoid}. In the course of this thesis and based on this source a new electron gun was developed. The discussion follows in the next chapter.

Chapter 4

Angular distribution of electrons emitted from a curved surface

4.1 Concept

The electron source, which is the subject of this chapter, was developed to create electrons with well defined total energy and emission angle. This angular selectivity is instrumental for investigations of the KATRIN main spectrometer. Based on the current pre-spectrometer electron source (chapter 3), which emits a broad angular spectrum, a new concept was investigated for the development of an electron source with a defined angle θ_{solenoid} at the entrance solenoid.

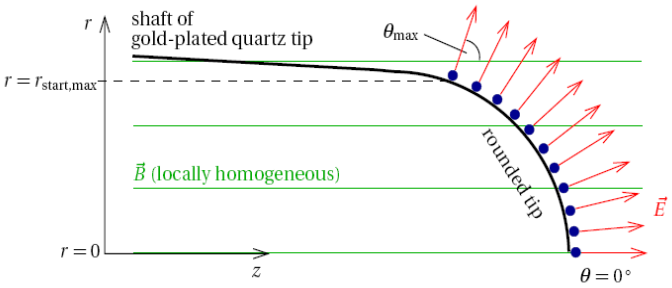

Figure 4.1: Schematic illustration of the angular dependence on the emission point. Electrons are created on the surface of the cathode and accelerated by the electric field, perpendicular to the surface. Due to axial symmetry, the electron starting position is defined by the radius r_{start}. Taken from [Val09].

Figure 4.1 summarizes the principle of the pre-spectrometer electron

source. The source has a spherical shaped tip and photoelectrons, created on the surface, are accelerated perpendicular to this surface by the E-field due to the applied electric potential U_{source}. The electric field accelerates the photoelectron and, since $\hat{F} = -e \cdot (\hat{E} + \hat{v} \times \hat{B})$, the magnetic field catches and eventually guides adiabatically the electron with rising kinetic energy, i.e. with rising $\hat{v}$. As K. Hugenberg [Hug08] showed, the angle θ_{solenoid} depends on the starting radius r_{start}, see figure 4.2.

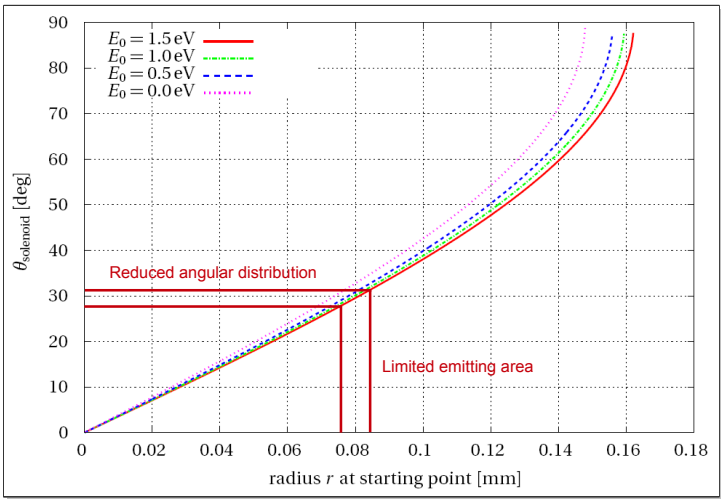

Figure 4.2: Dependence of the angle θ_{solenoid} in the center of the magnet on the starting radius at the tip. The four curves in this graph are results of the four different starting energies 0.0 eV, 0.5 eV, 1.0 eV and 1.5 eV used for the simulation. *New: Limitation of discrete starting radii reduces the emitted angular distribution of the source.* The plot shows that $\Theta_{\text{solenoid}} = 90\,^\circ$ is not reached. This is an artifact of the discretization. At high angles the slope of the curve is steep. The last $10\,^\circ$ are emitted in an r range of $\Delta r = 0.002\,\text{mm}$. The spacing between the starting points is approximately equidistant in r. Therefore, the simulation just does not include electrons with angles close to $90\,^\circ$. This figure shows the result of a simulation with $U_{\text{source}} = -1\,\text{kV}$ and $B_{\text{mag}} = 0.283\,\text{T}$. Taken from [Hug08].

The new source, developed within the scope of this diploma thesis is shaped similar to the pre spectrometer electron source. Analog to this previous electron gun, the new source is intended to scan the flux tube transversally but will provide electrons with a well determined angle $0\,^\circ \leq \theta_{\text{solenoid}} \leq 90\,^\circ$. Due to field inhomogeneities, especially in the outer flux tube regions of the spectrometer, measurements of electrons with high transversal energies are essential. The principle for angular selection is basically simple. To create electrons, with a specified angle θ_{solenoid}, these photoelectrons may

only be created at the corresponding radius r_{start}, on the surface. This is achieved by restricting the UV illumination on the cathode to these areas.

4.1.1 External illumination

To limit the irradiated area, one solution is the application of a frequency quadrupled *NdYAG* laser, which provides sufficient intensity in the UV (as discussed in section 2.2.1). Lasers provide fine, monoenergetic beam profiles, but will require to be attenuated by orders of magnitude. For the purpose of angular selection the illuminated spot is required to possess a diameter of the order of $\leq 100\,\mu$m and less[1]. Smaller diameters result in finer angular distributions. To ensure reproducibility of measurements, high precision positioning is demanded of the order of up to $\approx 30\,\mu$m. This is an approximation and is based on simulations, discussed in section 4.3.

A laser is expensive and requires safety precautions, which may impede measurements at the Mainz spectrometer. The required positioning precision represents technical challenges, especially with regard to reproducibility. These obstacles may be certainly overcome, but these solutions may be also unnecessary, since another illumination techniques was applicable.

4.1.2 Back illumination

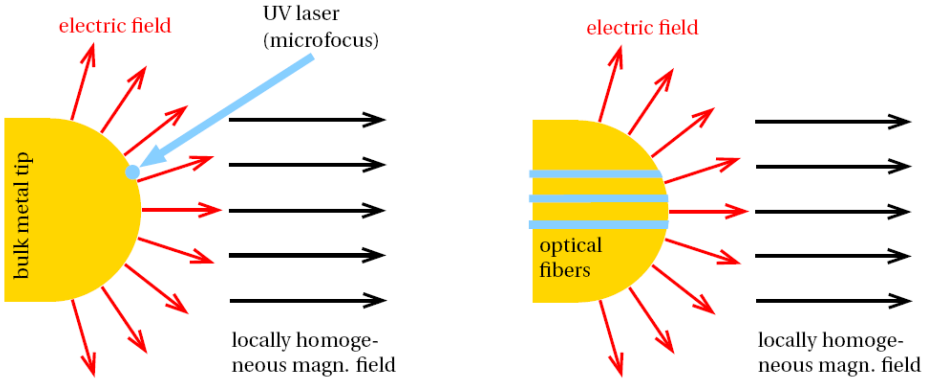

Figure 4.3: Two possibilities to restrict electron emission areas. Besides external illumination, e.g. by a laser microfocus (left), the application of optical fibers implemented in the cathode (right) offers the possibility of reproducible measurements and use of a larger array of light sources. Drawing from [Val09].

A possible illumination technique is to illuminate small spots on the surface from the back by using optical light guides, that are metal coated on

[1] Exact numbers depend on the electromagnetic field and are obtained from simulations, see section 4.3

the front surface, as described in figure 4.3. These fibers represent small and accurately localized electron-emitting spots on the surface. They increase the measurement precision and reproducibility and expand the array of suitable light sources.

Challenges and implementation

The implementation of a fiber within a metal bulk evokes several problems. Fixation of the fiber is required, e.g. by gluing or clamping. As the electric field is perpendicular to the surface and the angle between electric and magnetic field at the source define the resulting electron angle θ_{solenoid}, residual surface irregularities need to be reduced by polishing. This reduces UV-light reflections at the end of the fiber as well as high electric field strengths. Peaks on the surface, artificially enhancing the electric field strength, may otherwise result in field emission or add an uncertainty to electron starting energy distributions. The fiber surface needs a metal coating for photoelectron production. An adequate metal is to be selected, see section 2.2.3, and then evaporated and condensed on the cathode. Therefor an appropriate surface density of a few $\mu g/cm^2$ has to be specified.

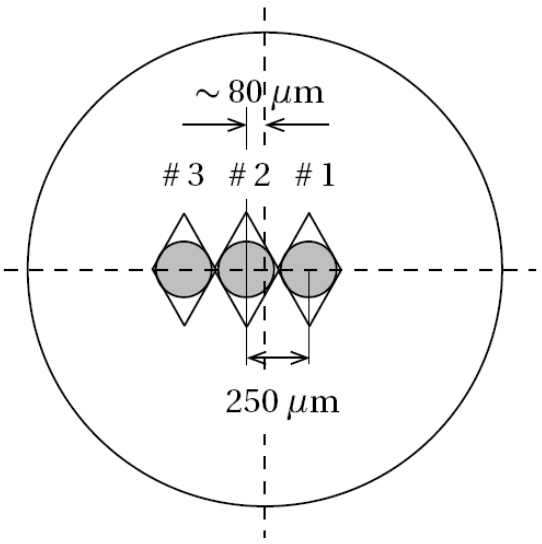

Figure 4.4: The optical fibers were clamped and glued into diamond shaped notches. The central fiber is positioned $\approx 80\,\mu$m off axis. This lay-out enables three different selectable angular intervals and ensures small distances between fibers and center. Drawing from [Val09].

The back illumination permits reproducible measurements with easy handling and allows to employ UV-LEDs. For the availability of multiple selectable electron angles as well as for the case, that one fiber is damaged,

three fibers were implemented. To pinch the fiber into the metal, the tip was bisected first. The fibers were clamped and glued into diamond shaped notches between both halves, as seen in figure 4.4. The polishing of fiber and surface was conducted in multiple steps with finest grit of $5\,\mu$m.

The pre-spectrometer tip consisted of quartz, to allow full illumination of the gold layer from behind. Since fibers are employed for the transmittance of UV-light, the use of quartz[2] is obsolete, the tip consists of solid aluminum with $r_{\text{tip}} = 1\,\text{mm}$ radius. Figure 4.5 shows the finished tip of the electron source.

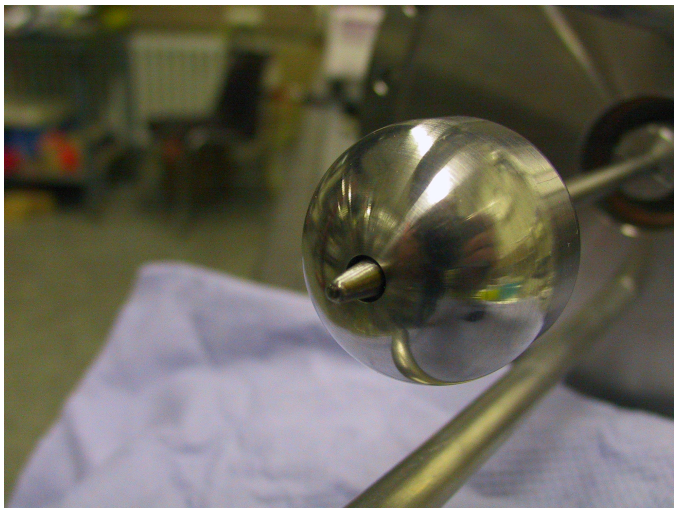

Figure 4.5: The finished electron source tip.

4.1.3 Optical light guides

The optical light guides were supplied by the company *j-fiber GmbH*, Jena. These *High-Power-Small-Core* (*HPSC*) fibers contain a high *OH* percentage and are designed for high power transmission in the near-UV and visible range, from 280 nm up to 750 nm. The central peak wavelength of both UV-diodes is outside this stated range, and application of this fiber was questionable. Suitable fibers designed for shorter wavelengths were not available from any of the inquired light guide suppliers. Figure 4.6 shows the fiber optical attenuation in $^{\text{dB}}/_{\text{km}}$. Because the average fiber length in the setup lies between 1 m and 1.5 m, the manufacturer *j-fiber* stated the transmittance of UV-light at 265 nm and 255 nm should be sufficient. This is supported by photoelectron production tests, see section 4.2.1. Further investigation may be of interest to interpret electron yield and angular distribution.

[2] as used as bulk material for the current pre-spectrometer electron source

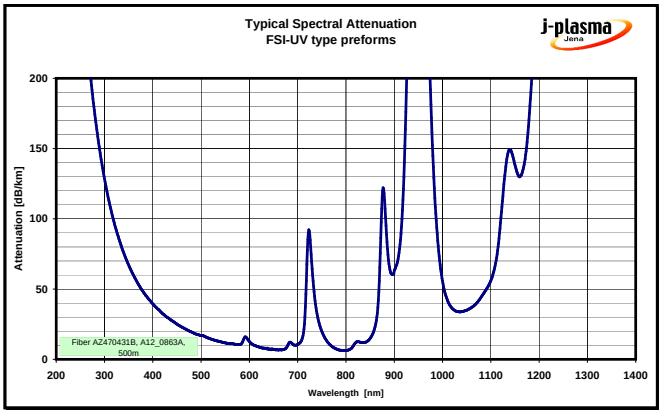

Figure 4.6: Typical attenuation for the selected fiber (in $^{\mathrm{dB}}/_{\mathrm{km}}$), provided by *j-fiber GmbH, Jena*. Wavelengths of $\lambda = 265\,\mathrm{nm}$ are highly attenuated and sufficient transmission had to be validated.

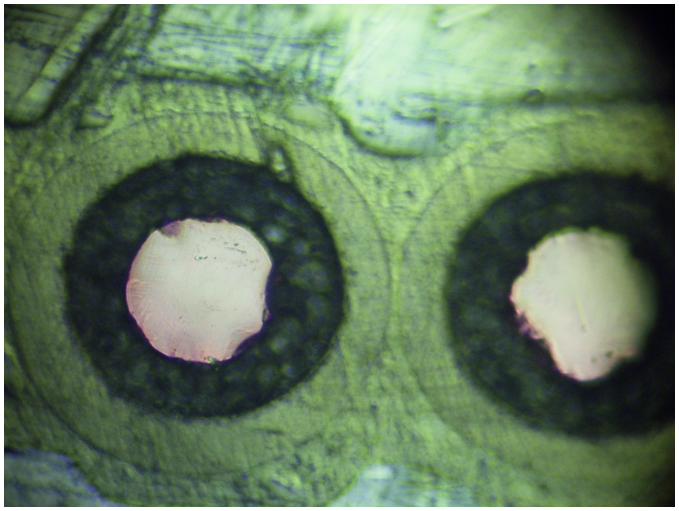

Figure 4.7: Picture of the light guides, as they are implanted into the tip. One can clearly distinguish the back-illuminated core (white), cladding (black) and coating.

The implemented light guide *FAQS00-98105022* is a 98/145/245 (core / cladding / coating diameters in μm) step index fiber, with *FCC-12* acrylate coating, a coating material, that guarantees long-term performance and reliability. The drawback of *FCC-12* coating is the specified operation temperature between -60 ℃ and 85 ℃. Hence bake out of the UHV-set-up at temperatures exceeding 85 ° is prohibited and the epoxy glue, holding the fiber, needs to be hardened within this temperature range. Different coatings were not available for the specified fiber.

Different fiber diameters were considered as well. Besides the 98 μm core diameter fiber a 25 μm (25/125/250) HP Quartz fiber was available. The smaller core diameter would have provided an enhanced angular selection at the expense of electron yield. For the purpose of the first proof of principle of this electron source, the application of the larger core-diameter was advisable.

Table 4.1: Positioning of the three fibers, from [Val09]. All positions were measured relative to the center of the aluminum tip. The mechanical preparation of the tip allows a positioning accuracy of about $\pm 20\,\mu$m, which determines the uncertainty to be applied to all values listed in the table. The outermost fiber #3 could not be used.

fiber no. comment	#1 'outer fiber'	#2 'inner fiber'	#3 broken (not used)
center of fiber	170 μm	80 μm	330 μm
innermost position, covered by core	121 μm	310 μm	281 μm
outermost position, covered by core	219 μm	129 μm	379 μm

Overall three light guides were implemented. The central 'inner' fiber was set off axis at $r_1 = 80\,\mu$m, as listed in table 4.1. Since the fibers are implemented in the aluminum bulk, exact positioning is technically challenging and a deviation of fiber position of up to $\approx 30\,\mu$m is possible. The distance between the fibers, in contrast, is known and was measured to be $250(\pm 10)\,\mu$m, see figure 4.8. The close positioning of the fibers with the central fiber $r_1 = 80\,\mu$m off axis enables three different selectable angle intervals and ensures small distances between fibers and center. Analog to the pre-spectrometer electron source (figure 4.2), the area emitting electrons capable of passing the magnet without reflection is situated within a radius of about $r_{\text{start}} \approx 135\,\mu$m around the z-axis[3]. The total diameter of a fiber amounts to 245 μm. Even when all fibers are embedded in a plane close to the z-axis, at least the outermost fiber can not possibly remain in the emitting area. The area emitting electrons with angles below 90 ° can be enlarged by increasing the local magnetic field at the source. Then at least a part of the outer fiber might be imaged onto the detector. As discussed

[3] At larger radii r_{start}, the angle between electric and magnetic field due to the curved surface is increased and electrons will gain angles $\theta_{\text{solenoid}} > 90\,^\circ$ and are magnetically reflected. The maximum radius can be increased by amplification of the local magnetic field.

in section 4.3, simulations show, that the maximal radius amounts to about $r \approx 182\,\mu$m with a magnetic field increase due to a water-cooled auxiliary coil, at a current $I_{\text{aux}} = 100\,\text{A}$.

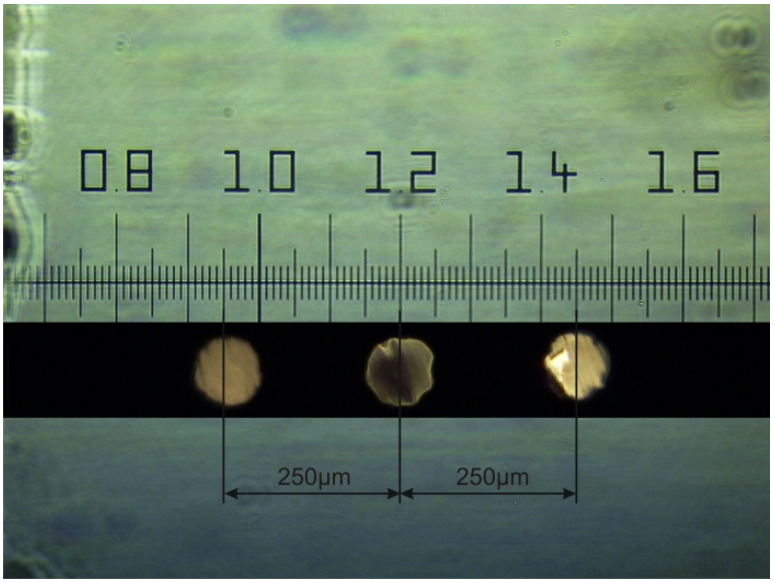

Figure 4.8: Relative positioning of the three fibers. Although the fiber position is only known with a considerable uncertainty of $30\,\mu$m, the relative distance between the fibers is exactly known to be $\delta = 250\,\mu$m.

4.1.4 Optical coupling

As discussed in section 2.2.1, light emitting diodes offer a worse beam profile in comparison to a laser. This was of disadvantage, since the illuminated spot was to be kept in the order of 10 to $100\,\mu$m. Due to the application of optical fibers, this worse beam profile is now secondary. Instead, the LED illuminates a fiber end and an optical coupling is to be established. UV-LEDs, equipped with a ball lens, showed superior efficiency at optical coupling, respectively electron yields, over flat-lenses.

Extended light sources like LEDs require an elaborate lens array for optical coupling. The alternative is simple placement of the light source in front of the fiber. In cooperation with the Institute of Applied Physics at the University of Münster, optical setups using UV-transparent microscope optics and/or lens-arrays were evaluated. The increase of efficiency was expected to amount up to 10 % with a high risk of decreasing the efficiency, which outweighs the benefits. So no extra lenses except the built-in ball lense of the diode were used. This consideration of course only applies for a proof of principle source.

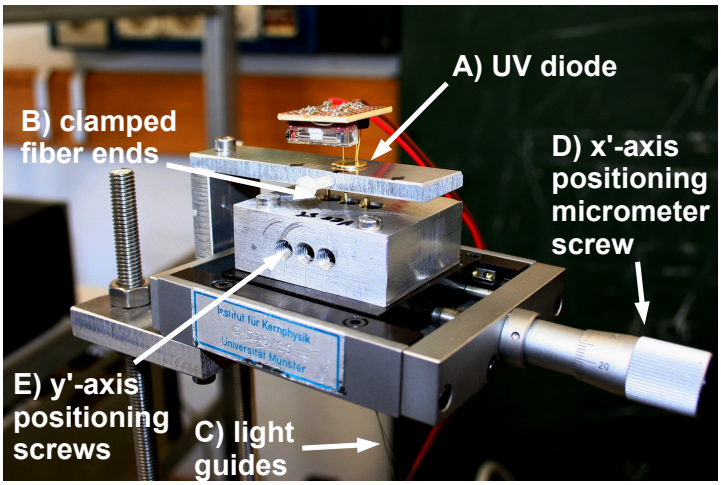

Figure 4.9: The fiber positioning device: The diode *(A)* is fixed on top, while the three fiber ends *(B)*, clamped in brazen jackets, are fixed in the micrometer-screw *(D)* driven sledge. The fiber x' and y' position are adjusted by the micrometer screw *(D)* and the three positioning screws *(E)*.

For optical coupling, the diode was fixed in a positioning device, as seen in figure 4.9. Clamped in brazen jackets, the fiber end positions are adjusted with a micrometer screw. Highest electron yields were gained at smallest distances $d \leq 1\,\mathrm{mm}$ between fiber and diode (see figure 4.10), despite the expectation that the focal length of the ball lens should result in optimum yield at a distance of about 5 mm.

4.1.5 Synopsis

A photograph and the technical drawing of the final electron source setup are presented in figure 4.11. Attached behind the tip, a hemispherical piece of aluminum (see figure 4.5) shapes the electrostatic field close to the tip. This cathode is screwed onto a hollow metal shaft, that is connected to the vacuum flange. Fed through this shaft and the attached 30 kV high voltage feedthrough, the fibers were attached to the fiber positioning device outside and illuminated with the UV light from the LED. At a distance $d_{\mathrm{lens}} = 23.8\,\mathrm{mm}$ in front of the tip, an electrostatic lens on ground potential further shapes the local electric field at the tip. The lens is mounted on the flange via two stainless steel poles. The maximal cathode potential U_{source} applied to the HV-feedthrough amounted to $-20\,\mathrm{kV}$. This results in a maximum electric field strength of $8.5\,\mathrm{kV/cm}$ between cathode and lens.

For the first measurement phase, silver with a surface density of

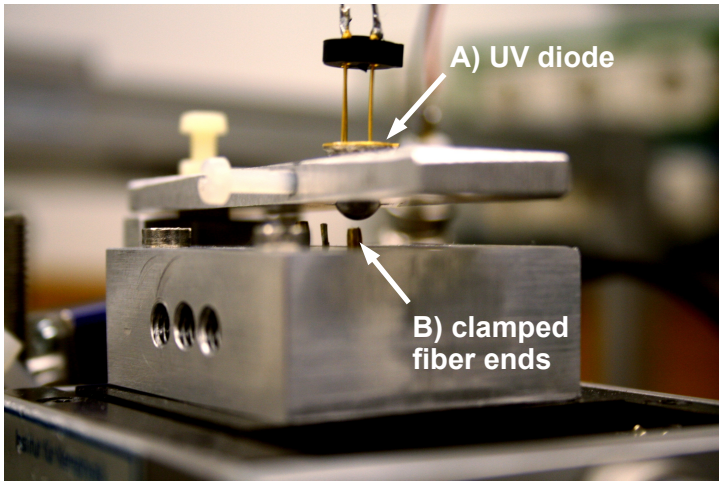

Figure 4.10: Close-up photograph of the interface between LED and fibers. Highest electron yields were gained with smallest distances $d \leq 1\,\mathrm{mm}$ between fiber and diode.

$\rho_{Ag} = 35(\pm 5)\,\mu\mathrm{g/cm^2}$ was condensed on the surface and for the second measurement period, copper was condensed on the fibers with $\rho_{Cu} = 30(\pm 5)\,\mu\mathrm{g/cm^2}$. Additionally to copper on the tip, silver and chrome layers were applied on the shaft of the tip. The idea behind this approach was to test whether the photoelectron yield by external illumination was sufficient and to additionally measure a full transmission function from these surfaces. A comparison of these transmission functions with the measured functions of both fibers would provide additional information about the distribution of θ per fiber.

Before the source was installed at Mainz, the photo-electron production from a silver layer and a sufficient vacuum stability required verification and were tested at Münster (section 4.2.1). During the measurements the outer fiber was accidentally broken, leaving only the inner two operational.

With regard to previous simulations[4] the distributions of $\theta_{\mathrm{solenoid}}$ were assumed to possess a width of about $\Delta\theta_{\mathrm{solenoid}} \approx 30^\circ$ per fiber. Elaborate simulations, see section 4.3, were carried out after the measurement period in Mainz.

[4] analog to the tip electron source at the pre-spectrometer at Karlsruhe, see section 3.2

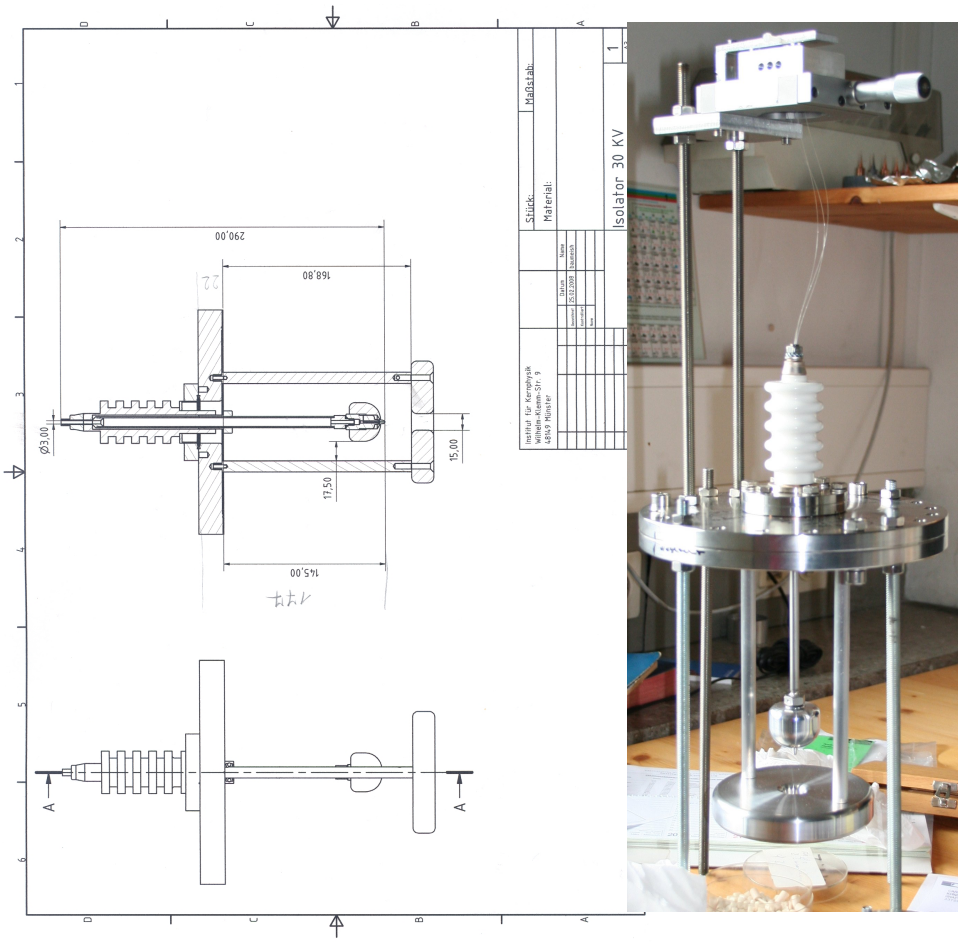

Figure 4.11: Technical drawing and photograph of the final electron source setup.

4.2 Measurements

4.2.1 Measurements at Münster

Tests of vacuum stability and photoelectron production were conducted at a test stand, see figure 4.12, that was part of the diploma thesis of D. Hampf [Ham08]. The vacuum chamber was equipped with an avalanche photo diode (APD). This liquid N_2–cooled detector operated at a reverse bias of up to $U_{\mathrm{det}} \leq 1550\,\mathrm{V}$, rendering the APD a low noise single photon detector. Due to the lack of an according strong magnetic field, adiabatic guidance was no integral part of these measurements.

Summary

The vacuum stability was proven at pressures in the order of about $p = 4 \times 10^{-7}$ mbar. Photoelectron production measurements were conducted with photo-pulses of $5\,\mu\text{s} \leq \tau_{\text{LED}} \leq 40\,\mu\text{s}$ length as well as in continuous mode for improved photoelectron counts.

Figure 4.13 confirms that, by using this electron gun setup, photoelectrons were successfully produced. The figure illustrates the dependence of the photoelectron energy of the cathode potential U_{source}. During these measurements the 'outer' fiber irreparably broke, but fortunately this outermost fiber was expected to show the least photoelectron electron count rates at Mainz, as discussed in section 4.1.3 and 4.3. Hence the incident did not impair following measurements.

4.2.2 Measurements at Mainz

After photoelectron-creation had been validated, the electron source was brought to and installed at the Mainz spectrometer. Test runs with a closed shutting valve between spectrometer and the ellipsometry chamber proved a reasonable vacuum stability at pressures p_{source} in the order of $\approx 3(\pm.5) \cdot 10^{-7}$ mbar. The pressure was read out to amount $p_{\text{source}} \approx 2.5(\pm.5) \cdot 10^{-7}$ mbar after opening the valve.

Typical measurement conditions were:

- Cathode high-voltage set to $U_{\text{source}} = -18053\,\text{V}$.
- The retarding voltage scanned from $U_{\text{source}} - 10\,\text{V}$ (no transmission of the spectrometer) to $U_{\text{source}} + 15\,\text{V}$ (transmitting spectrometer).
- The current through the water cooled auxiliary coil was set to $I_{\text{aux}} = 100\,\text{A}$, for increased electron yields from the outer fiber.
- The spectrometer resolution was set to $\Delta E = 1.5\,\text{V}$ at $U_{\text{spec}} = -18\,\text{kV}$.

Figures 4.14 shows the results of four measurements of the transmission function. The transmission functions were scanned beginning with the two runs, measuring the transmission function of the 'inner' fiber, followed by two runs measuring the 'outer' fiber. During the third run a strong discharge forced an interlock high-voltage shutdown resulting in the lack of some data points. These discharges occurred several times during the measurement period and are assumed to be Penning discharges, see section 2.3. After high voltage restoration the fourth run was conducted. It shows analog behavior compared to the previous one. During all measurements a reproducible offset $\Delta U_{\text{plus}} \approx 2.5\,\text{V}$ was seen for the transmission functions. This may be partially be explained by an insufficient calibration of the absolute energy scale.

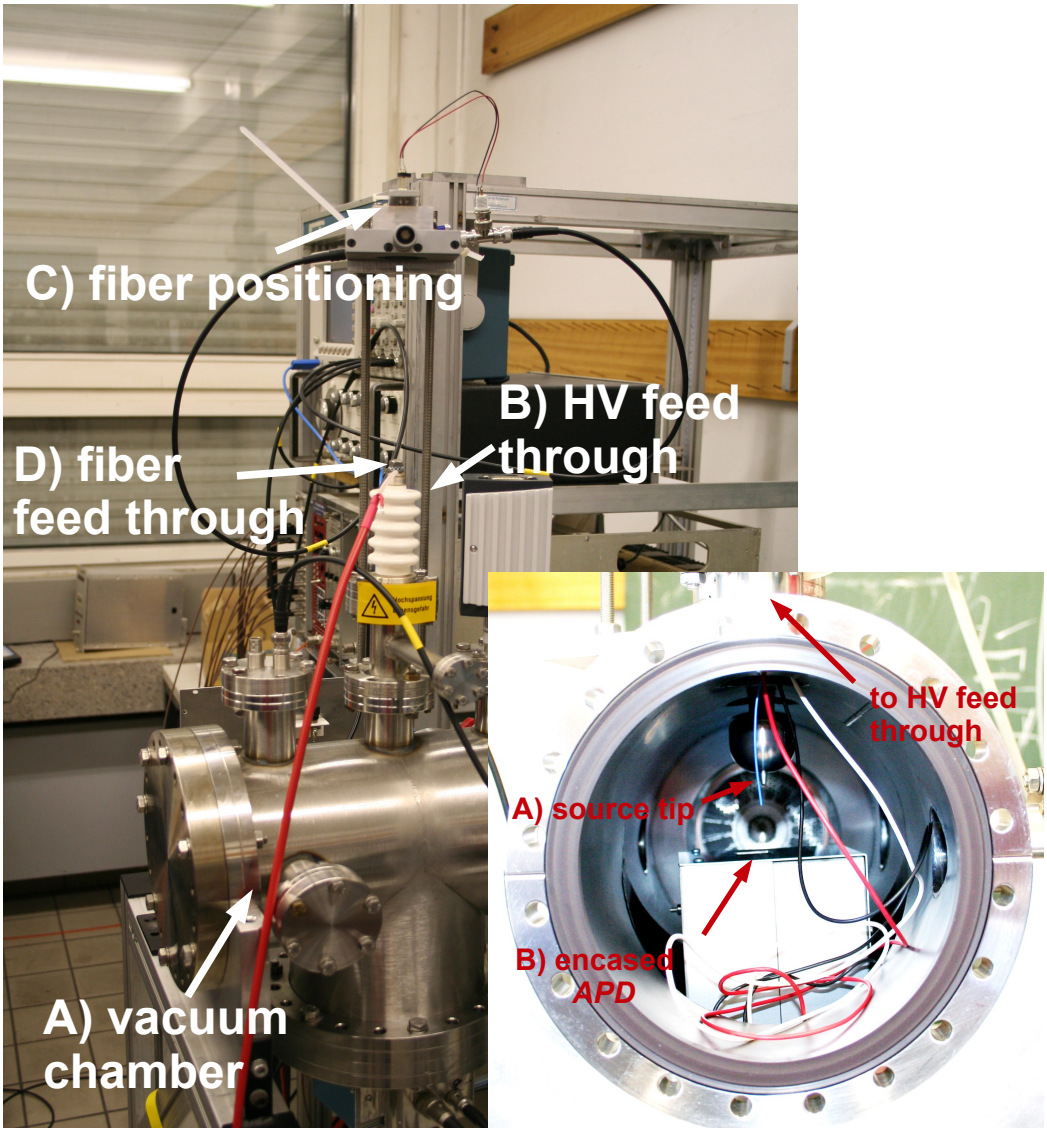

Figure 4.12: The test stand at Münster.
Left: The HV feedthrough *(B)* is mounted on the vacuum chamber *(A)*. Optical coupling is established at the fiber positioning device *(C)*. At *(D)* the other fiber end is fed through the HV-feedthrough into the vacuum chamber. *Right*: The tip of the electron source *(A)* points towards the encased, N_2-cooled *APD (B)*. The right photo was taken during assembly, with wires reaching into the chamber, that were later removed for the measurements.

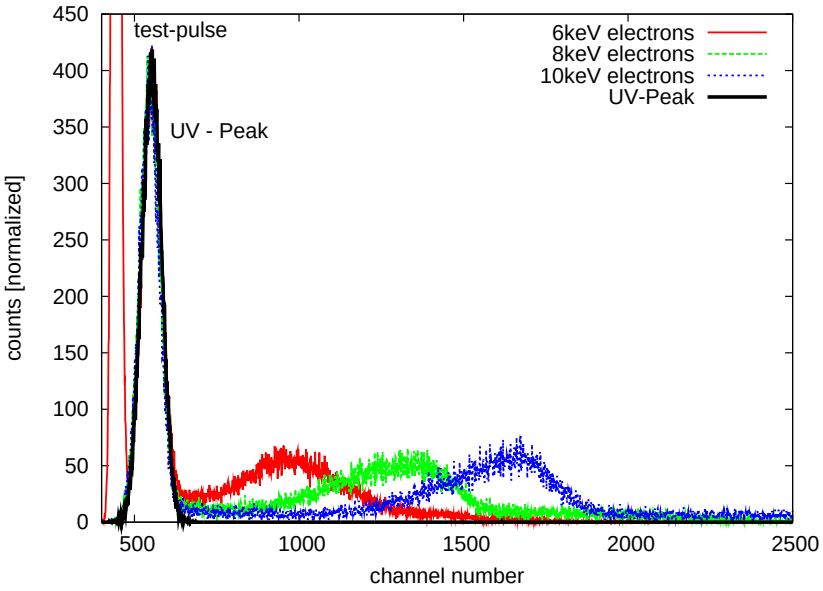

Figure 4.13: Verification of photoelectron production at Münster. The correlation between electron energy, defined by the potential U_{source}, i.e. channel number, and the detected signal height show that this signal consists of electrons. For $U_{\text{source}} = 0\,\text{V}$ merely photons, depicted black, were detected. The counts were normalized to the UV-peak height.

All transmission function measurements showed reproducible behavior for the fibers. The transmission functions corresponding to the inner fiber are steeper and their point of first rise is at lower surplus energies. This is a first hint, that the two fibers emit electrons at different angles θ_{solenoid}. As can be seen, the angular range is broad, since the transmission functions are spread along the whole $\Delta E_{\text{res}} = 1.5\,\text{eV}$ which denotes the spectrometer resolution. Tracking simulations and comparison to measurements will be described in section 4.3.

Notes on the count rates

Comparing transmission functions of both fibers, count rates of the different runs are normalized to match the rate of the first run. The outer fiber showed a decreased electron count rate by a factor of about 2.5. The scaling factors for each run are:

'inner' fiber		'outer' fiber	
#1	#2	#3	#4
×1	×0.97	×2.28	×2.60

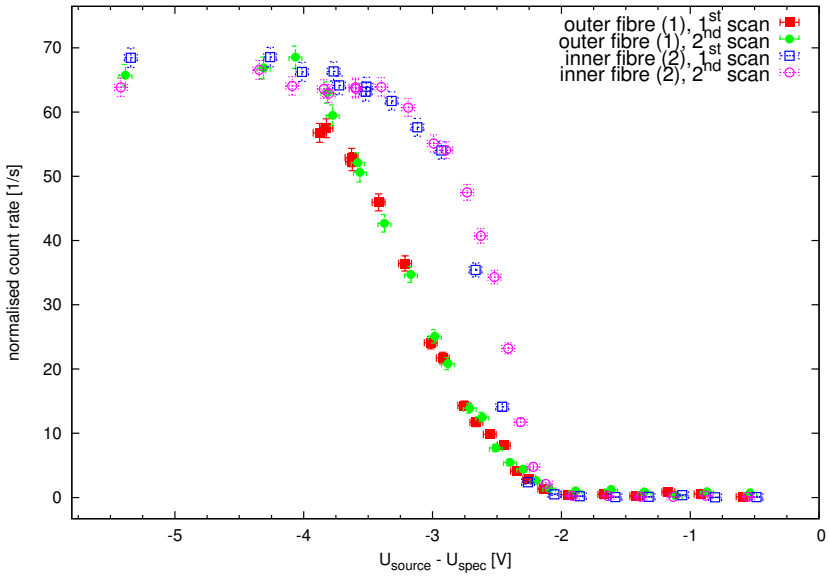

Figure 4.14: Four transmission function measurements, two for each fiber (Taken from [Val09]).

It is interesting to note that without a guiding B-field (see section 4.2.1) the 'outer' fiber showed a higher photoelectron count rate[5] than the 'inner' fiber. This may be caused by two effects.

1. The photoelectron count rate from the surface depends on

   - a difference of the effectiveness σ_{oc} of the optical coupling,
   - the efficiency of photoelectron creation at the fiber surface. The energy of incident photons (optical spectrum of light source) and material properties of the thin metal layer primarily determine the yield from one fiber.
   - the quality of the fiber surface, which might be damaged and / or uneven after polishing and thus reflect or absorb a fraction of light.

   According to measurements without a guiding magnetic field (see section 4.2.1) the electron yield from the outer fiber is assumed to be larger by a factor of approximately $\times 1.5$. An exact relative effectiveness can not be distinguished because of uncertainties concerning the manually established optical coupling and a possible change of conditions over time, due to transports, and exposure to air.

[5] factor $\times 1.5$

2. The opposing factor is the effective imaged area, emitting photoelectrons with $\theta_{\text{solenoid}} \leq 90\,^{\circ}$. Simulations as in chapter 4.3 show, that a large fraction of electrons from the outer fiber will be magnetically reflected before entering the spectrometer, hence lower electron yields are expected.

4.2.3 Discussion

Two different transmission functions and resulting different angular emissions have been measured for both fibers. This shows experimentally that with non-adiabatic acceleration of the photoelectrons, with an E-field at an angle to the B-field, the transversal energy of the electron can be defined.

The width of the measured transmission functions may be broadened by a energy smearing, caused by an starting energy distribution (photoeffect, section 2.1) as well as fluctuations of U_{source} and U_{spec}. However since the transmission functions spreads over the full $\Delta E_{\text{res}} = 1.5\,\text{V}$ resolution, the angular emission is expected to be broad too. For further understanding of the source properties, simulations are necessary. These are presented in the following section 4.3.

4.3 Simulations

In order to analyze the measured transmission functions of both fibers, simulations, including electron tracking from the source to the high magnetic field, are necessary. This will help to understand and possibly improve the angular emission from the source.

The electron source is an improved version of the current pre-spectrometer electron source. The angular definition is based on the spherical shape of the electrode surface. Hence it is reasonable to recapitulate the angular emission of this tip.

Analog to chapter 4.1 the r_{start}–dependence of $\theta_{\mathrm{solenoid}}$ is investigated for the new geometry at first. The rotational symmetric geometry of the electrostatic setup, that was used for these simulations, is shown in figure 4.15. The whole electromagnetic setup is axially symmetric around the z-axis.

Figure 4.16 shows the dependence of the angle $\theta_{\mathrm{solenoid}}$ in the high magnetic field on the starting radius r_{start} for two magnetic field setups. The first case regards the magnetic field of the solenoids alone, while for the second case, the field of the auxiliary coil is included (with $I_{\mathrm{aux}} = 100\,\mathrm{A}$). The correlation of $\theta_{\mathrm{solenoid}}$ with r_{start} can be explained by an electron acceleration from the cathode until the magnetic guidance dominates, for a detailed discussion see [Hug08]. All electrons with $\theta_{\mathrm{solenoid}} \leq 90\,^{\circ}$ are emitted from within a certain radius $r_{\mathrm{max,off}} \leq 135\,\mu\mathrm{m}$ and $r_{\mathrm{max,100A}} \leq 182\,\mu\mathrm{m}$. increasing the magnetic field at the source also increases this threshold. It should be noted, that the exact magnetic field of the auxiliary coil can only be calculated approximately due to uncertainties of the coil geometry.

4.3.1 Angular emission of a fiber

The following considerations were made in order to analyze the angular emission (fig. 4.17).

- The fiber is positioned within the metal tip, parallel to the z-axis.
- The radial positions of the center of a fiber, specified as the offset o, are $o_1 = 80\,\mu\mathrm{m}$, $o_2 = 170\,\mu\mathrm{m}$ and $o_3 = 330\,\mu\mathrm{m}$.
- The core radius of a fiber is $f = 49\,\mu\mathrm{m}$.
- It is assumed that electrons are only emitted from the fiber core area (depicted gray).
- The function $s(r)$ corresponds to the length of the segment (green) of a circle of radius r that overlaps with the fiber core. $s(r)$ can be derived from figure 4.17. It is defined as

$$s(r) = 2 \cdot r \cdot \arcsin\left(\sqrt{1 - \left[\frac{r^2 + o^2 - f^2}{2 \cdot o \cdot r}\right]^2}\right). \tag{4.1}$$

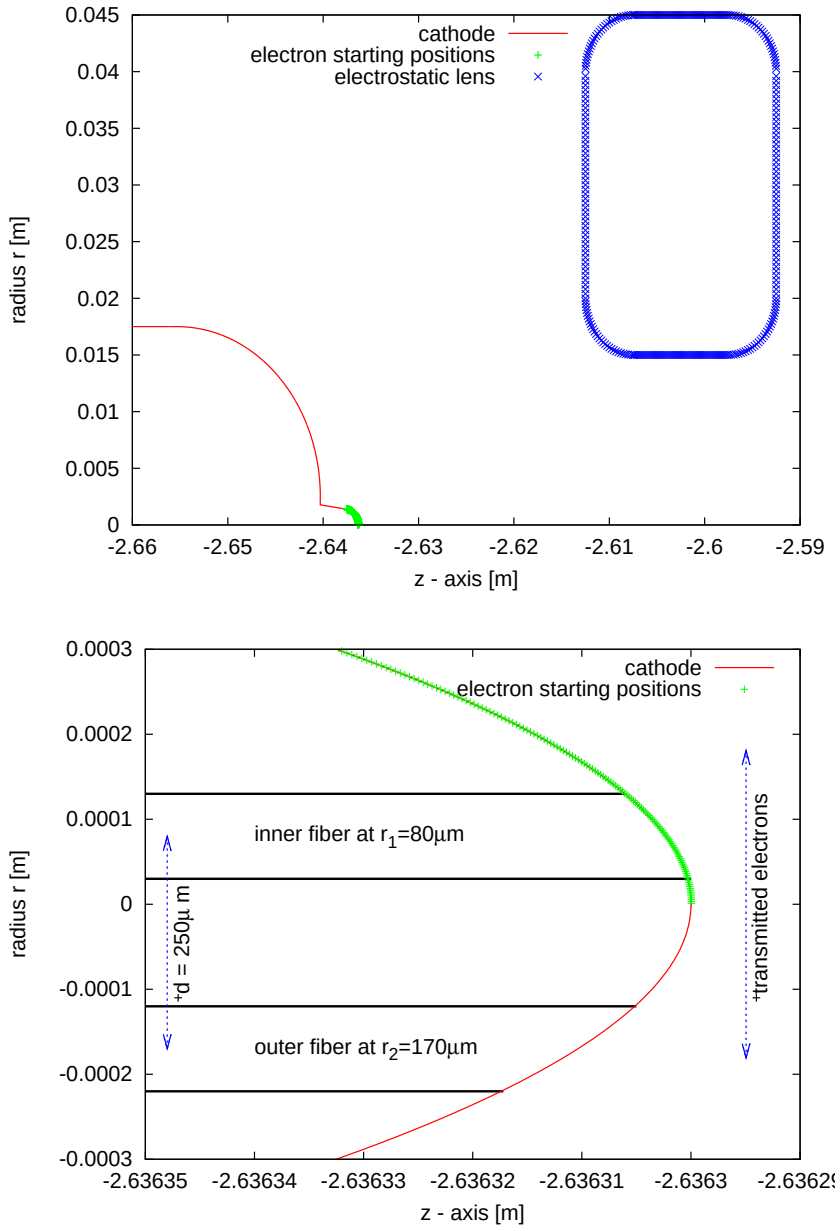

Figure 4.15: The rotational symmetric geometry used to simulate the electron source. The surface curvature in the right figure is misleading due to the aspect ratio of the axes. On the right, a maximum radius for transmitted electrons ($\theta_{\text{solenoid}} \leq 90\,^{\circ}$) is illustrated (blue arrow to the right). This radius $r_{max} = 182\,\mu\text{m}$ corresponds to a current $I_{\text{aux}} = 100\,\text{A}$.

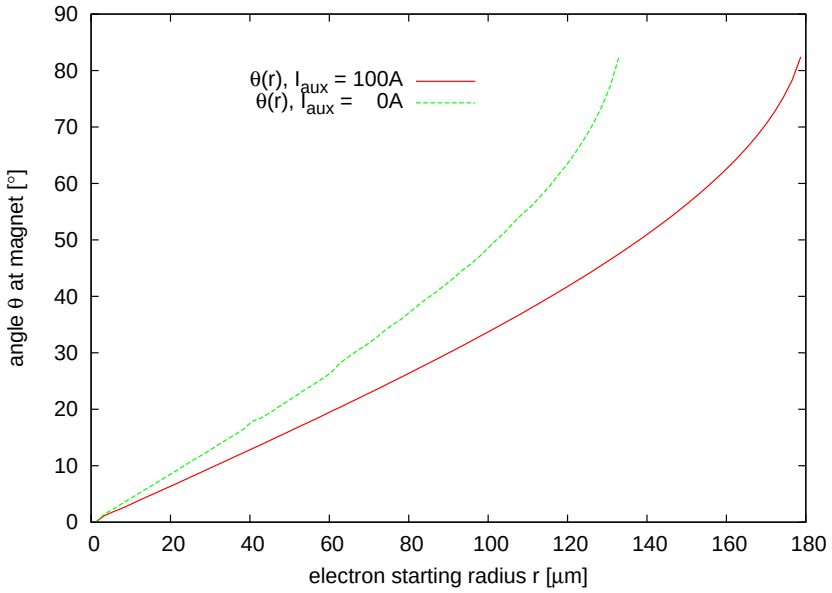

Figure 4.16: The dependence of the electron angle θ_{solenoid} at the magnet on the electron starting radius r. In the figure angles θ_{solenoid} close to 90 ° are not reached. This is due to discretization, all angles θ_{solenoid} between 0 ° and 90 ° can be obtained.

- This function $s(r)$ directly correlates to the number of electrons $n(r)$ emitted on this specific radius r.

$$s(r) \propto n(r)dr \tag{4.2}$$

Under this assumptions the number of electrons per radius, $n(r)$, is given by 4.2 with an unknown constant multiplicator.

r can be converted to an angle $\theta_{\text{solenoid}}(r)$, analog to figure 4.16. The angular emission in arbitrary units is then obtained by plotting $s(r)$ as a function of θ_{solenoid}, as shown in figure 4.18.

As mentioned, this plot is based on the assumption, that electrons are only created within the fiber core radius f. Additionally a possible misalignment of the electron source in the ellipsometry chamber can not be excluded, but is not regarded in these investigations.

4.3.2 Transmission functions

As the next step, transmission functions can be derived and compared to those obtained by measurements.

1. The number of electrons created within a radius r_{max} is gained from

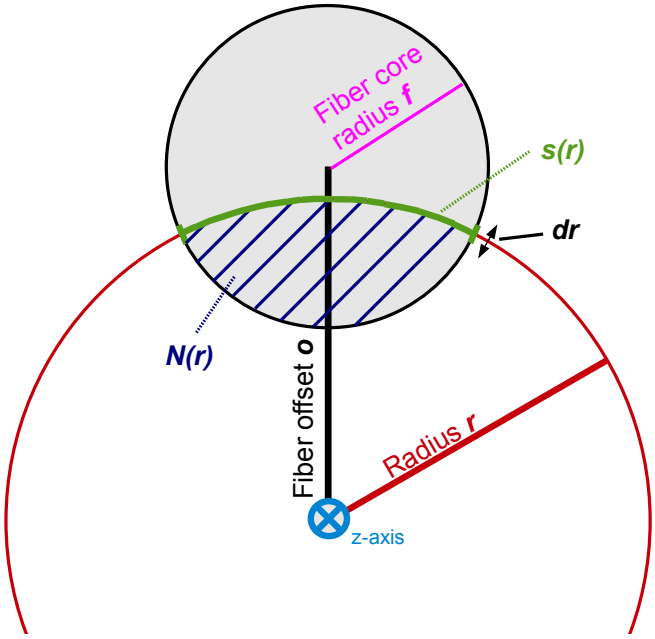

Figure 4.17: Schematic illustration of the tip surface, front view. The fiber core (gray) is positioned a distance o of the z-axis (light blue) and has a radius f (magenta). The radius r from the z-axis is depicted with a red circle. The segment $s(r)$ of this circle intersects with the area of the fiber core. $s(r)$ (green) is proportional to the number of electrons emitted from the core with $\theta_{\text{solenoid}}(r)$. Electrons with angles $\leq \theta_{\text{solenoid}}(r)$ are emitted from the blue shaded area.

the integration

$$N(r_{\text{max}}) = \int_{r_0=0}^{r_{\text{max}}} n(x)dx \ . \tag{4.3}$$

2. r_{max} corresponds to an angle $\theta_{\text{pinch,max}}$ (figure 4.16).

3. For a given spectrometer setting (U_{ana}, B_{ana}) the transversal energy $E_{\perp,\text{ana}}$ at the analyzing plane depends on the angle θ_{solenoid} at the magnet.

$$E_{\perp,\text{ana}} = \Delta E \cdot \sin^2\left(\theta_{\text{solenoid}}\right), \tag{4.4}$$

with the spectrometer resolution ΔE, in this case

$$\Delta E = E_{\text{source}} \cdot \frac{B_{\text{ana}}}{B_{\text{solenoid}}} = 1.5\,\text{eV} \tag{4.5}$$

4. With equation 4.4, $N(r_{\text{max}})$ can also be expressed as $N(E_{\perp,\text{max}})$, the number of electrons with transversal energies $E_\perp \leq E_{\perp,\text{max}}$ at the

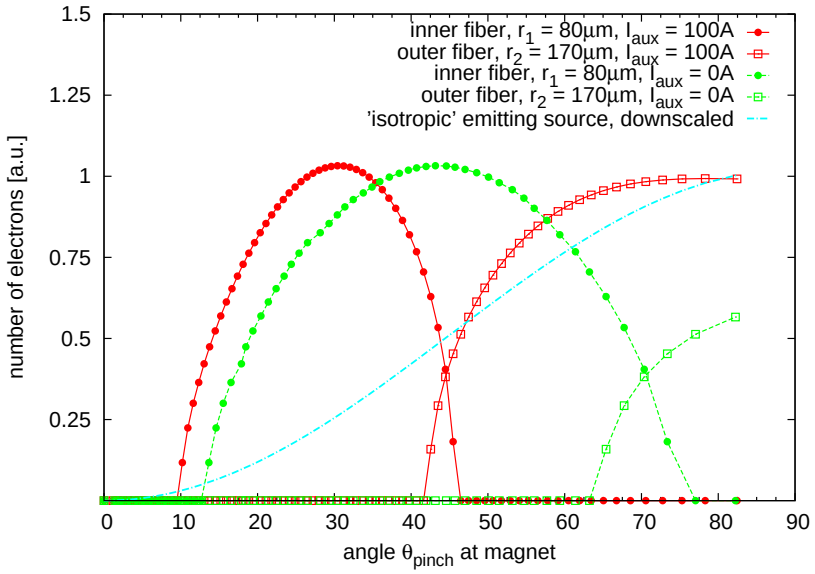

Figure 4.18: The theoretical derived number of electrons per angle $n(\theta_{\text{solenoid}})$. The green lines depict a setup without the auxiliary coil. The angular distributions are broad, they overlap and a large fraction of electrons from the outer fiber (right) is magnetically reflected. With a current $I_{\text{aux}} = 100\,\text{A}$ the angular width of both distributions is reduced and a larger fraction of electrons from the outer fiber is able to pass the magnet. *For comparison the 'isotropic' emission of the full surface is illustrated in light blue. Due to a larger surface, this distribution was downscaled.*

analyzing plane. $E_{\perp,\text{max}}$ equals the amount of surplus energy necessary to transmit $N(E_{\perp,\text{max}})$ electrons.

5. Plotting the number $N(E_{\perp,\text{max}})$ against the difference

$$\Delta U = U_{\text{source}} - U_{\perp,\text{spec}} = \frac{1}{q} \cdot E_{\perp,\text{max}} \tag{4.6}$$

results in the transmission function.

In figure 4.19, the calculated transmission functions are shown and compared to measurements. While the mean position and separation of both theoretical functions matches those functions measured at the Mainz spectrometer, there is conflict concerning the shape of the functions. The reason for this disparity is discussed in the following.

4.3.3 Convolution with a Gaussian

At photoelectron creation, the electron would gain kinetic energy $0 \leq E_{\text{start}} \leq E_{\text{max}}$ from the photon, as can be seen from equation 2.1. The corresponding

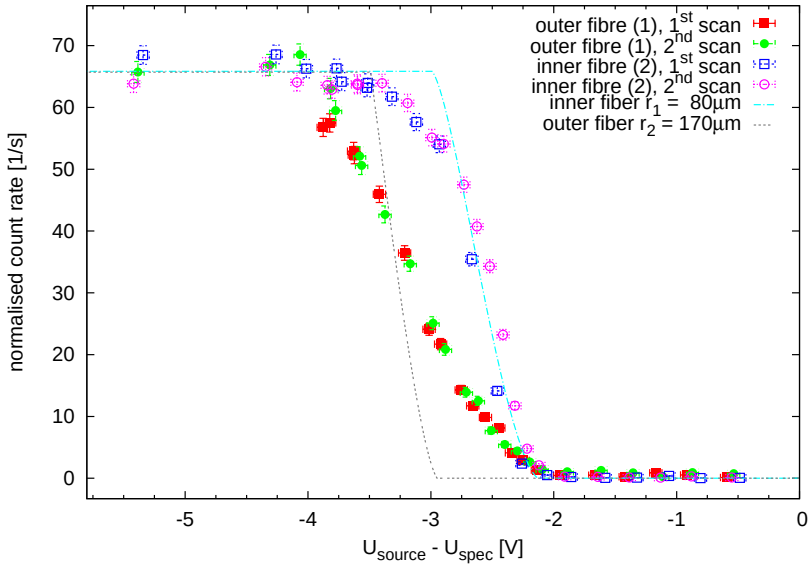

Figure 4.19: Theoretical transmission functions compared to measured transmission functions. Both theoretical transmission function positions were shifted by $\Delta E = -1.85\,\mathrm{V}$ to adjust to the four measured functions. This offset is most probably due to an insufficient energy calibration before the measurement. While the central positions of measured and simulated transmission function are similar, the shape of both functions differ.

momentum vector is assumed to be isotropically distributed. This has an effect on transmission function measurements, since the electron energy $E_{\parallel}$ in the analyzing plane is directly affected. As a second effect, noise and fluctuations of cathode and spectrometer potential affect transmission function measurements. To express these additional influences

1. the varying starting energy can taken into account in the simulation, with random energies between E_{start} and $0\,\mathrm{eV}$,

2. the transmission function is convoluted with a distribution function to account for noise and fluctuations of the applied potentials.

For time-of-flight and transmission function measurements from the planar plate electron source, see section 3.1, K. Valerius used the latter method. A normal-distributed energy smearing described the data well [Val09]. The simulation was able to reproduce the experimental results of a similar measurement.

The routine *tm_ convolute.cpp* was developed to calculate the transmission function and convolute the result with an energy distribution. It

- reads the simulated electron trajectories,

- creates a histogram of the simulation runs analog to figure 4.16,
- calculates $N(i) = \sum_{x=0}^{i} n(x)$ and r_i,
- reads total, transversal and longitudinal energies (E_{source}, $E_{\perp}$ and $E_{\parallel}$ respectively) and
- plots the corresponding transmission function.

For the convolution an analytical solution is not possible since $s(r)$ does not possess a unique primitive. Hence as a second step, the transmission function is convoluted discretely with a Gaussian $g(x)$ as an approximation for a real energy smearing:

$$g(x) = \frac{1}{\sigma \cdot \sqrt{2\pi}} \cdot exp\left(-\frac{1}{2} \cdot \left(\frac{x - x_0}{\sigma}\right)^2\right) \tag{4.7}$$

σ is user-defined, usually between 0.15 eV and 0.5 eV and directly correlates to the starting energy distribution and noise on the potentials. Figure 4.20

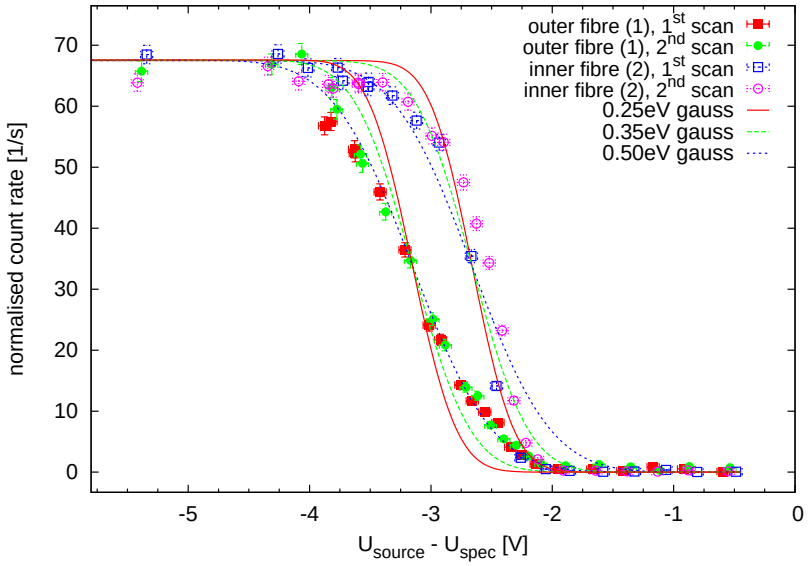

Figure 4.20: The theoretically transmission functions were convoluted with a gauss distribution, see equation 4.7. σ was varied between 0.25 eV to 0.50 eV. Both functions were shifted by an offset $\Delta E = 2.45$ eV to match the measured results.

shows the comparison of convoluted theoretical transmission functions with measured transmission functions. The consistency agreement between both has been clearly improved by incorporating noise and photon energy distribution. While the transmission function positions are consistent (most

notably the position difference of the two fibers), there is a conflict concerning the shapes of the transmission functions. If the energy smearing is only caused by noise and electron starting energy distribution, σ should be independent of r, respectively the fiber position. As can be seen in figure 4.20, σ_{outer} has to be assumed to be on the order of 0.35 eV to 0.50 eV to match the transmission function for the outer fiber. In contrast σ_{inner} for the inner fiber is expected to be smaller, approximately between 0.25 eV and 0.35 eV. By variations of

1. the fiber position, maintaining a fixed distance between the fibers,
2. the magnetic fields, e.g. due to variation of I_{aux}
3. assumed effective area for photoelectron production, namely variation of the variable f

this inconsistency could not be explained. The according simulations are provided in the appendix.

This inconsistency is likely to be caused by slightly different electromagnetic geometries of experiment and simulation. A possible explanation is the assumption of a perfect spherical shape at the critical area within $r_{\text{start}} \leq 182\,\mu\text{m}$. This small area was manually polished and due to technical limitations it is unlikely to assume a perfect surface structure. A deviation of an ideal surface and its electric field can not be excluded and will result in altered angular emissions.

4.3.4 Discussion

This electron source was developed with the intention to create angular defined electrons. The principle is based on a curved surface with its perpendicular E-field at an angle to the magnetic field. The angular distribution of θ_{solenoid} is thereby determined by the emitting area, was which decreased by reducing the area to a spot with a diameter of $98\,\mu$m. The fiber-implemented tip-electron-source successfully demonstrated this principle. After comparison of measured transmission functions to simulations, the angular emission is mostly understood.

However this distribution remains still too broad for a possible application at the KATRIN spectrometer. Methods to increase angular selectivity are associated with the implementation of larger numbers of fibers with smaller diameters, distributed over the surface. Today there are UV-transparent fibers available with core diameters of $10\,\mu$m and presumably even smaller diameters will be available in the future. Cladding and coating of the fibers still represent inevitable problems and restrict further advances. The full diameter of these fibers still amounts to about $250\,\mu$m. Even half the diameter would be too large for feasible setups. This means the fraction of the photoelectron creating area in comparison to the full imaged surface

still remains small, restricting the number of selectable electron angles. Miscellaneous ways of improvement of implementation of fibers were discussed and possible solutions result in technical challenges to be faced. The development of this electron source was eventually abandoned with the advent of a new source geometry discussed in the following chapter.

Chapter 5

Angular definition by rotatable electric fields

5.1 Concept

An improved geometry to define θ_{solenoid} precisely consists of a rotatable parallel plate capacitor in a magnetic field (Fig. 5.1). The two plates, referred to as front and back plate, lie on voltages U_{front} and U_{back}, with a resulting difference voltage $\Delta U = U_{\text{front}} - U_{\text{back}}$ over a distance d between the plates. The electric field of an ideal parallel plate capacitor is perpendicular to the plate surface. Photoelectrons are created on the backplate and accelerated along the field lines towards the front plate. To convey transversal energy $E_{\perp}(\hat{x})$, the electron is required to be accelerated at an angle α to the magnetic field. Hence the plates are rotated by this angle α. This geometry is, in the first place, a simple and easy to use setup. The electric field $\hat{E}(\hat{x})$ of a parallel plate capacitor is known and also analyzable in detail. For reduced calculation times and small plate distances d in the order of ≤ 2cm the local magnetic field can initially be approximated homogeneous and constant.

The electric field component $\hat{E}_{\perp}$ is transversal to the magnetic field $\hat{B}$, with

$$\hat{E}_{\perp} = \hat{E}_{\text{tot}} \cdot \sin^2(\alpha),$$

In principle the larger $\hat{E}_{\perp}$ the higher is the higher is the transversal energy the electron will finally gain at larger distances to the plates. Thus by rotation of the capacitor and variation of the potential difference ΔU between the two plates $\hat{E}_{\perp}$ will be changed and accordingly the transversal energy in distance to the plates. This way the electron angle at high magnetic fields θ_{solenoid} becomes selectable. The important variables for this geometry are namely:

- The angle α between $\hat{E}(\hat{x})$ and $\hat{B}(\hat{x})$. In case of the previous chapter 4, this angle was achieved by the curvature of the surface.

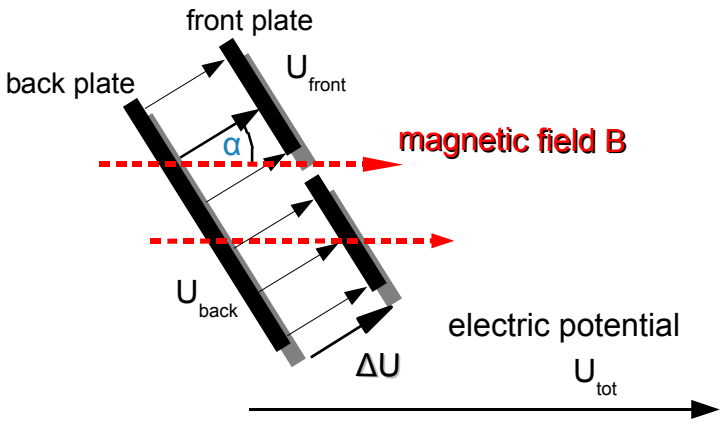

Figure 5.1: The schematic concept of a new electron source. (explanation: see text)

- The total potential, defined by the back plate $U_{\text{tot}} = U_{\text{back}}$. This is the total amount of energy, the electron gains between source and ground potential.
- The potential difference $\Delta U = U_{\text{front}} - U_{\text{back}}$. In combination with α, this potential difference defines the amount of transversal energy of an electron and therefore θ_{solenoid}.
- The plate distance d. This defines the field strength $\hat{E} = \frac{\Delta \hat{U}}{d}$ as well as the effect of apertures, discussed in section 5.2.2.
- The local magnetic field $\hat{B}(\hat{x})$. The magnetic field leads the electron adiabatically after the initial acceleration. Amongst others the field strength defines the transition to adiabatic motion and affects the amount of transversal energy of an electron at the entrance of the spectrometer.
- Plate size and aperture dimensions. While the influence of most variables is self evident, plate size and the aperture also play a role. Both lead to field effects like electric field punch-through and electrostatic lens effects. These are discussed in section 5.2.2.

5.2 Simulations, with simplified geometries

Since the new source is to be tested at Mainz, the geometry is designed for the local environment at Mainz. At the center of the ellipsometry-chamber $z = -2.638(\pm 0.010)\,\text{m}$, the magnetic field amounts to about

$B_{\text{center}} = 164.0\,\text{G}$. At the center the value deviates z-axis dependent with $\frac{\Delta B}{\Delta z} \approx 0.9\,\text{G/mm}$. The field may have been increased by an auxiliary coil, but this is not necessary for this source and would increase the B-field uncertainty.

For the first simulations the geometry is simplified. For now the magnetic field is approximated by a constant homogeneous magnetic field. This reduces computation times and enables a larger number of simulations. In contrast the electric field is calculated in detail without greater impact on computing times.

5.2.1 An ideal planar plate capacitor

The simulations were conducted step by step, beginning with the most simple geometry. The first runs were conducted with electrons created at the back plate of an ideal parallel plates capacitor in the xy plane of approximately infinite area. For electron tracking the electrons are tracked from $z_{\text{start}} = 1 \cdot 10^{-8}\,\text{m}$ in front of the back plate with no starting energy $E_{\text{start}} = 0\,\text{eV}$ and a constant magnetic field of user defined strength B is assumed. The magnetic field lines run at an angle α to the z-axis[1]. It is additionally assumed, that the electron is able to pass the front plate, without requiring an aperture. At later stages the additional effects of aperture and inhomogeneous B-field will be investigated.

Analog to the tracking from a tip, the electrons movement begins along the electric field lines, until the magnetic field dominates. Figure 5.2(a) now shows the the first 5 cm of an example electron trajectory. The electron is accelerated by $\Delta U = 4\,\text{kV}$ over $d = 1\,\text{cm}$ and guided along the magnetic field lines (here: $\alpha = 30\,^\circ$), depicted by a linear fit (green).

In figure 5.2(b) the displayed z-axis of figure 5.2(a) is zoomed to the first $120\,\mu\text{m}$. The distance between electron starting position and the guiding magnetic field line amounts just $48.9\,\mu\text{m}$, demonstrating that adiabatic guidance dominates the motion early on.

Transversal energy oscillations

By rotating the coordinate system by $\alpha = 30\,^\circ$ around the y-axis, so that the magnetic field line is parallel to the z'-axis, an important feature of the electron source can be explained, see figure 5.3(a). The electron is accelerated along the z-axis and moves along the magnetic field lines, following a spiral motion. Since there is an angle α between $\hat{z}$ and $\hat{B}$, and due to the spiral motion the electron is de- and reaccelerated by the perpendicular fraction of the electric field depending on the phase of the motion, i.e. the transversal energy $E_\perp$ oscillates. This dependence is demonstrated in figure 5.3(b).

[1] and perpendicular to the y-axis

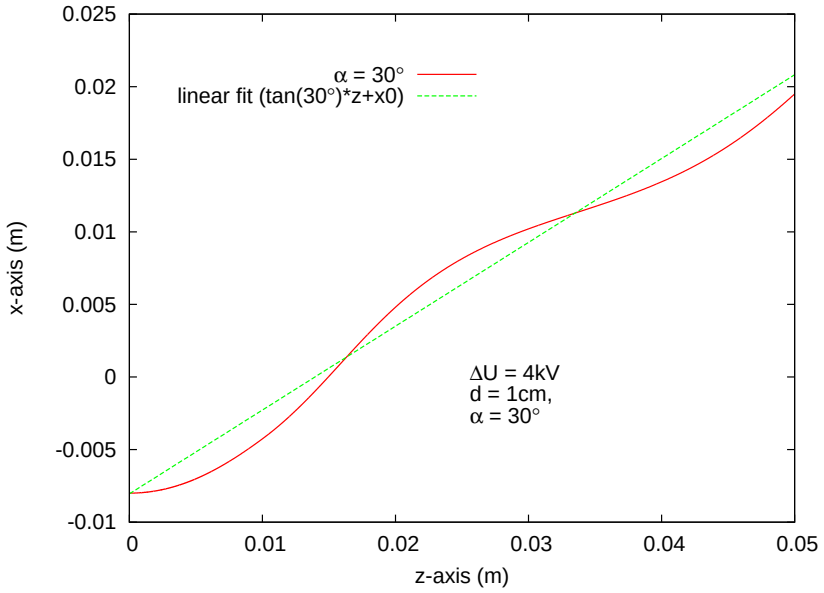

(a) Overview

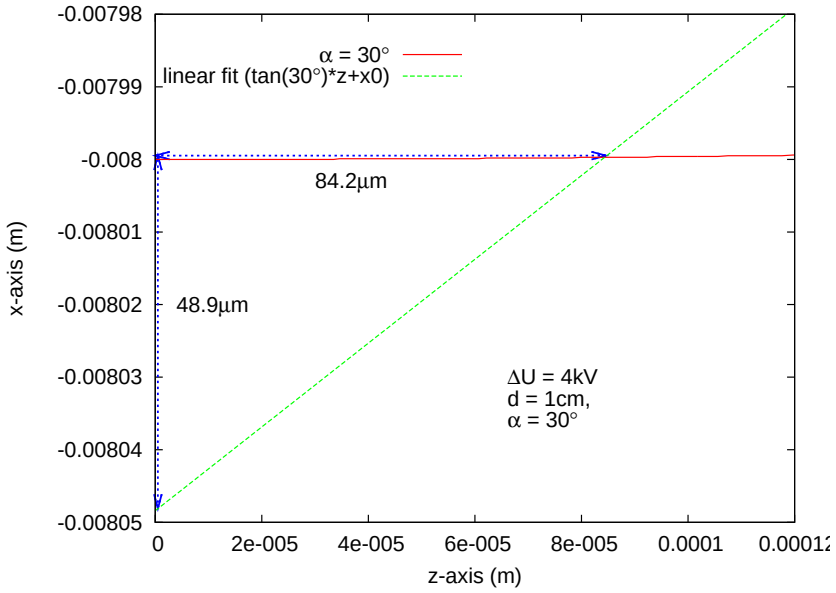

(b) zoom into back plate area

Figure 5.2: Transition to adiabatic movement and $E_\perp$ oscillations. The simulations show an electron started within ideal plate capacitor with $\alpha = 30\,°$, $\Delta U = 4\,\mathrm{kV}$, with $d = 1\,\mathrm{cm}$, $U_{\mathrm{tot}} = -18.6\,\mathrm{kV}$, $E_{\mathrm{start}} = 0\,\mathrm{eV}$ and $B = 200\,\mathrm{G}$. The back plate is positioned at $z = 0\,\mathrm{m}$. The electron trajectory is depicted red, the linear fit for the magnetic field line is green. In figure 5.2(a) one can observe the electron following a spiral motion along the magnetic field line. Since the electron is not instantaneously guided adiabatically the electron starting position and intersection of the magnetic field line with the back plate differ, which is show in figure 5.2(b), where the z-axis is enhanced.

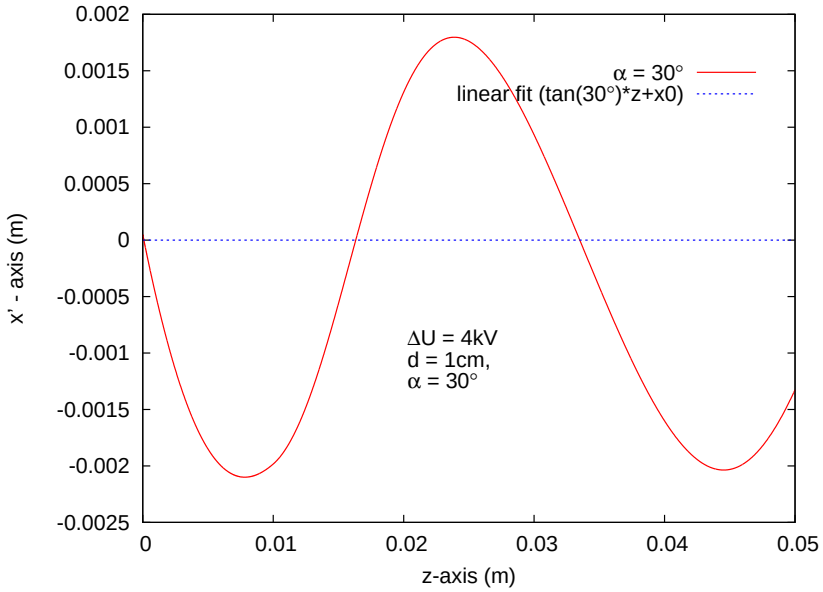

(a) Rotation of system xz by 30°to $x'z$, so $\hat{B} \parallel z$.

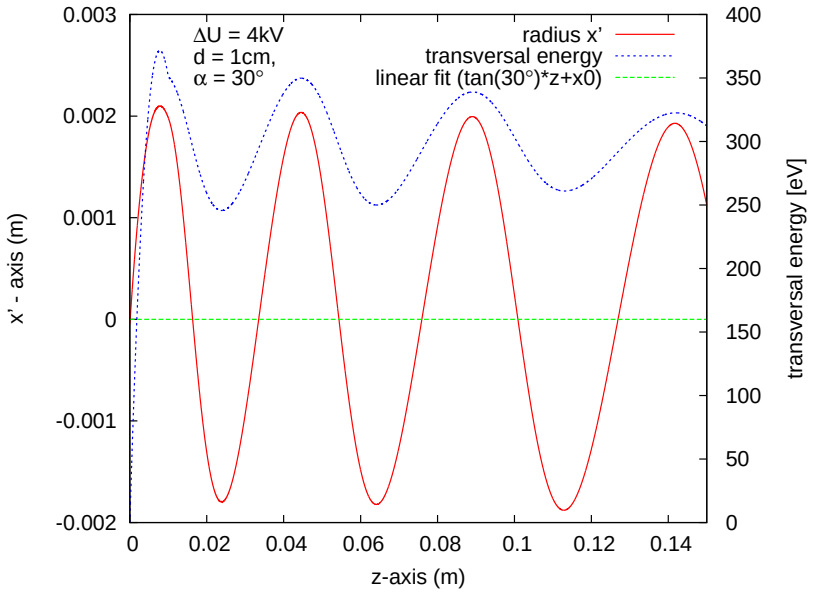

(b) Correlation of x' and $E_\perp$

Figure 5.3: fig. 5.2 continued

These oscillations are critical for understanding the features of this geometry, as discussed in the following.

$E_\perp$ in dependence of ΔU

As a second step electrons were tracked under various conditions. Figure 5.4(a) describes the dependence $E_\perp(\Delta U)$ for a given angle $\alpha = 20\,^\circ$, $B = 300\,\mathrm{G}$ and $U_{\mathrm{back}} = -18.6\,\mathrm{kV}$. The increase of $E_\perp$ close to the back plate steepens with an increased ΔU. The front plate at $z_{\mathrm{front}} = d = 0.01m$ is depicted by the vertical black line, the back plate is positioned at $z_{\mathrm{back}} = 0m$. Since the electric field is not continuously differentiable at the front plate, transversal energy oscillations show a kink when the electron is passing the front plate. In the zoom of the z-axis, see figure 5.4(b), one can observe the decay of $E_\perp$-oscillations with the decreasing electric field at a distance to the source. For $z \to \infty$ the transversal energy $E_\perp(r, z)$ of an electron converges to $E_\perp(z = \infty) = E_{\perp,\infty}$. At first glance $E_{\perp,\infty}$ seems proportional to ΔU.

Assuming adiabatic guidance, from the magnetic moment

$$\mu = \frac{E_\perp(\hat{x})}{B(\hat{x})} = \text{const.} \tag{5.1}$$

and

$$E_\perp(\hat{x}) = E(\hat{x}) \cdot \sin^2\theta(\hat{x}) \tag{5.2}$$

follows

$$\theta_{\mathrm{solenoid}} = \arcsin\sqrt{\frac{B_{\mathrm{solenoid}}}{B(\hat{x})} \cdot \frac{E_\perp(\hat{x})}{E_{\mathrm{solenoid}}}}. \tag{5.3}$$

The transversal energy $E_\perp(\hat{x})$ in the local (weak) magnetic field $B(\hat{x})$ can be converted to an angle $\theta_{\mathrm{solenoid}}$ at the center of the solenoid.

For a well defined $\theta_{\mathrm{solenoid}}$ the oscillation is required to be small, to reduce systematical errors. Hence simulations are conducted over a distance z until $E\perp, \infty$ can be obtained with small remaining systematical errors. In figure 5.4 this conversion (equation 5.3 was applied to designate the $\theta = 90\,^\circ$ limit as a horizontal red line. Electrons with higher transversal energies will be magnetically reflected and can not enter the spectrometer.

In between the plates, the motion of the electron and thus the transversal energy oscillations depend on the electric field strength, as can be seen in figure 5.5. For the three electrons, the field strength was kept constant at $2\,\mathrm{kV/cm}$, while the plate distance d was varied. Although the electrons were started at the same electric field, they eventually gain different transversal energies in dependence of the decoupling from the capacitor field.

The simulations show that electrons can be created with this principle (fig. 5.4) that have transversal energies corresponding to $\theta_{\mathrm{solenoid}} \approx 0\,^\circ$ to $\theta_{\mathrm{solenoid}} \approx 90\,^\circ$, depending on ΔU.

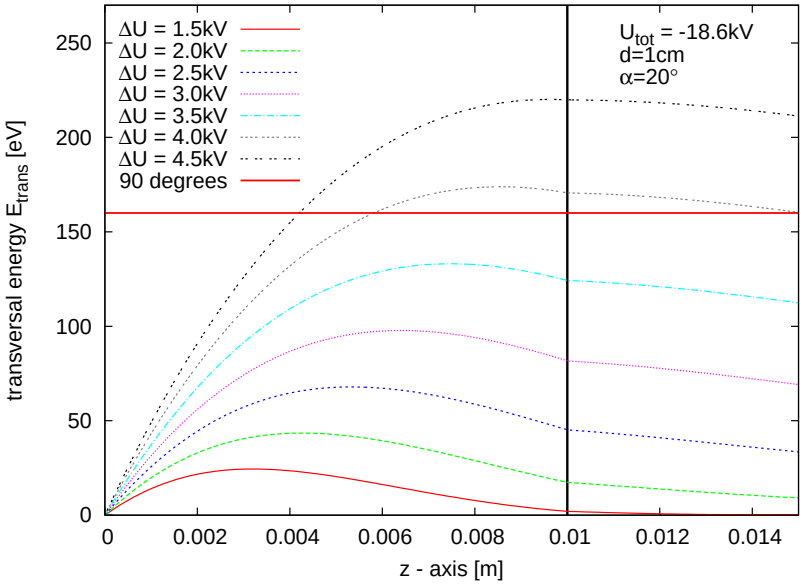

(a) First 1.5cm

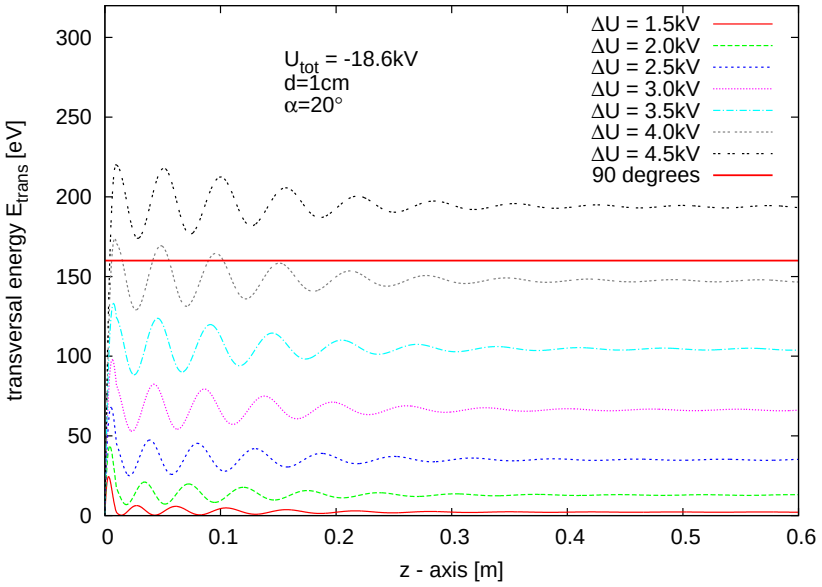

(b) Overview

Figure 5.4: The transversal energy $E_\perp(z)$ of an electron, in dependence of the accelerating voltage ΔU, is plotted against the z-axis. The angle $\alpha = 20\,^\circ$ is fixed. The front plate is depicted at $z_{\text{front}} = 0.01\,\text{m}$ with a vertical black line, the back plate is positioned at $z_{\text{back}} = 0$. The horizontal red line depicts the required transversal energy to gain electrons of $\theta_{solenoid} = 90\,^\circ$. The simulations show that electrons can be created with this principle that have transversal energies corresponding to $\theta_{\text{solenoid}} \approx 0\,^\circ$ to $\theta_{\text{solenoid}} \approx 90\,^\circ$, depending on ΔU. With increasing distance to the plate the oscillations decrease until at infinite distance the transversal energy converges to $E_{\perp,\infty}$.

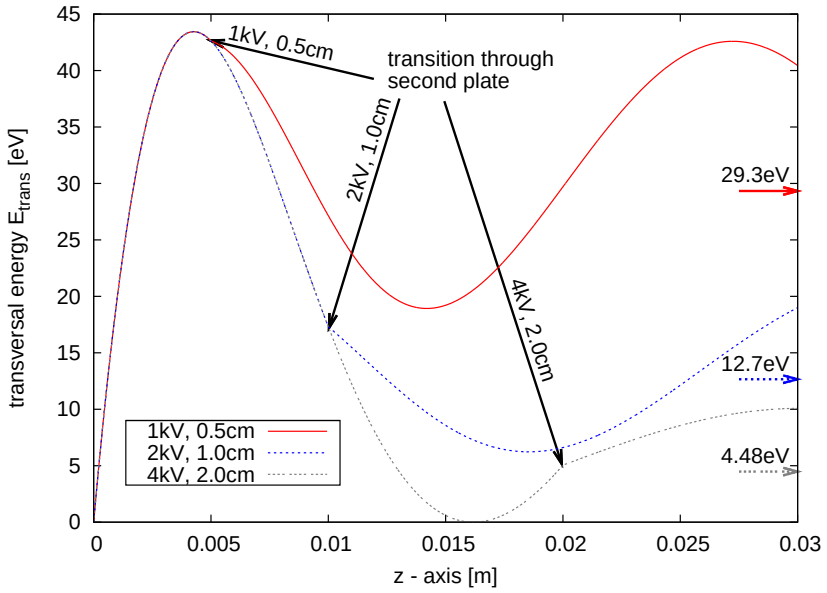

Figure 5.5: The dependence of transversal energy oscillations of the decoupling from the plate capacitor field. For the three cases, the field strength was kept constant for varying distances d. The electrons follow the same trajectory until they reach their front plates at $d_1 = 0.5\,\mathrm{cm}$, $d_1 = 1.0\,\mathrm{cm}$ and $d_3 = 2.0\,\mathrm{cm}$ (plates not depicted). One can observe the discontinuity of oscillations at the the front plate. On the right the electron transversal energy in infinite distance is depicted with arrows.

.

$E_\perp$ in dependence of α

Simulations for a fixed potential difference and variations of α are analog to the preceding. As shown in figure 5.6. The simulations assume a magnetic field of $B = 300\,\mathrm{G}$. This is in contrast to a calculated magnetic field of $\approx 170\,\mathrm{G}$ at the center of the chamber. However this difference does not affect principle observations, while on the other hand the plots are suited to demonstrate the following important effect:

at first, with increasing α, the transversal energy is increased as well. For $\Delta U = 4\,\mathrm{kV}$, see figure 5.6(a) and 5.6(b), the angles α are proportional to the transversal energy at infinite distance $E_{\perp,\infty}$, for the simulated range of α.

Lowering the potential difference to $\Delta U = 2\,\mathrm{kV}$, see figure 5.6(c), the electron transversal energy oscillation at the front plate $z_{\mathrm{front}} = 0.01\,\mathrm{m}$ is at or near a minimum. The displayed electrons gain less transversal energy $E_{\perp,\infty} < 20\,\mathrm{eV}$ and additionally their sequence has changed, meaning that highest transversal energies $E_{\perp,\infty}$ are gained at medium angles close

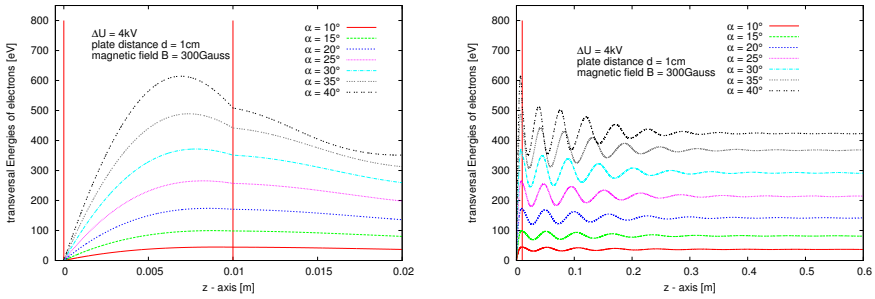

(a) $\Delta U = 4kV$, enhanced (b) $\Delta U = 4kV$

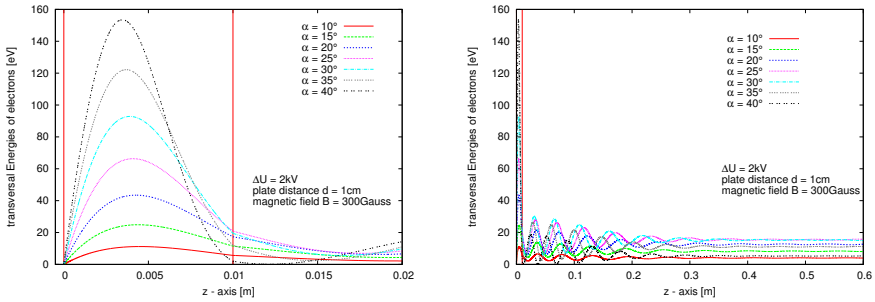

(c) $\Delta U = 2kV$, enhanced (d) $\Delta U = 2kV$

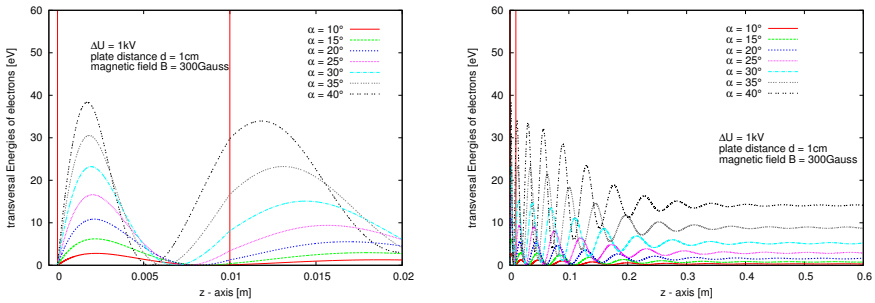

(e) $\Delta U = 1kV$, enhanced (f) $\Delta U = 1kV$

Figure 5.6: The transversal energy of an electron for a fixed potential difference ΔU in dependence of the angle α. A change of α with fixed ΔU also changes $E_\perp$ and therefor θ_{solenoid}. $B = 300\,\text{G}$, $U_{\text{tot}} = -18.6\,\text{kV}$, $d = 1\,\text{cm}$, ΔU and α variable.

to $\alpha = 25\,°$. This coherence is displayed in figure 5.7. The reason is, that electrons with higher angles α leave the strong electric field at a minimum. In comparison to the strong field between the plates, the electric field outside the plates is weak and incapable to re-increase the transversal energy sufficiently. This effect is of course less pronounced at strong electric fields outside the plates, namely at high front plate potentials U_{front}.

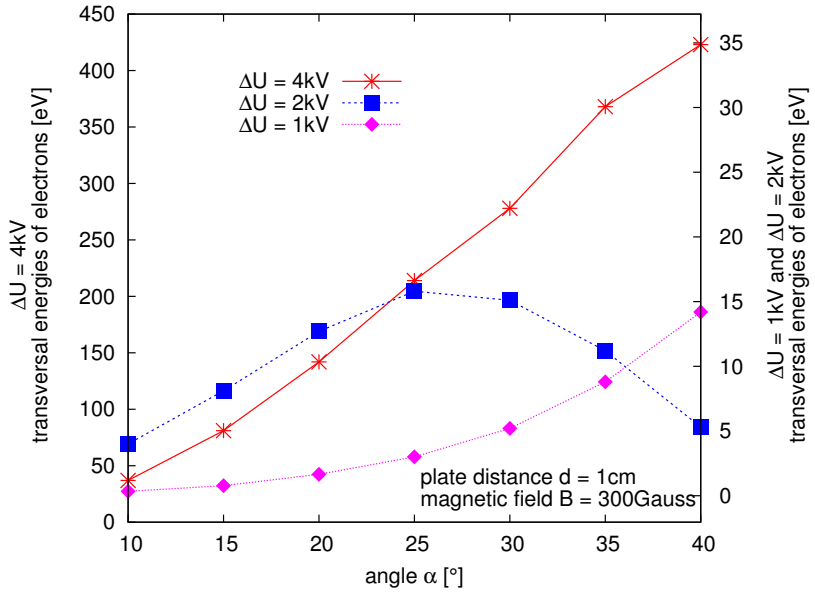

Figure 5.7: Transversal energy $E_{\perp,\infty}$ in dependence of angle α and ΔU. For $\Delta U = 4\,\mathrm{kV}$, depicted red, the transversal energy rises analog with α. By reducing the potential difference to $2\,\mathrm{kV}$, depicted blue, the $E_\perp$ oscillation is close to a minimum when the front plate is reached. The result is a local maximum of $E_{\perp,\infty}$ at medium angles close to $\alpha = 25\,$.

Short summary

By setting ΔU and α the transversal energy $E_\perp$, and thus the angle $\theta_{\mathrm{solenoid}}$, is defined. Besides the mentioned variables α, ΔU, U_{back}, $\hat{B}$ and d, these simulations show, that the transversal energy $E_{\perp,\infty}$ also depends on the *phase of motion* at the front plate, when entering a weaker (and inhomogeneous) electric field.

The simulations assisted at setting useful parameters for the electron source geometry. The back plate potential will be set to $U_{\mathrm{back}} = -18.6\,\mathrm{kV}$, the energy spectrum endpoint of tritium decay.

The plate distance was set between $d_{min} = 0.01m$ and $d_{max} = 0.02m$. This is a compromise between a slightly inhomogeneous magnetic field and a sufficient potential drop between the plates, supported by the fact, that large transversal energies can be obtained with less than $\Delta U \leq 4\,\mathrm{kV}$ at small angles $\alpha \leq 20\,^\circ$. Limited by the dimensions of the ellipsometry chamber, the plate diameter is set to $\oslash_{\mathrm{plate}} = 100\,\mathrm{mm}$. This leaves $\approx 5\,\mathrm{cm}$ between plate and ground potential to prevent discharges.

The electric field strength is required to be below $\approx 10\,^{\mathrm{kV}}/_{\mathrm{cm}}$ to prevent discharges between the plates. Hence ΔU was set to $\leq 5\,\mathrm{kV}$, to ensure the presence of at least one maximum of transversal energy oscillations while

alleviating the choice of a suitable voltage source.

Since besides in the fields in between the plates, the E and B-field outside the capacitor affect the transversal energy $E_{\perp,\infty}$ as well, for electron tracking multiple magnetic field strengths $160\,\mathrm{G} \leq B_{\mathrm{const}} \leq 300\,\mathrm{G}$ will be simulated[2].

5.2.2 Integration of an aperture in the geometry

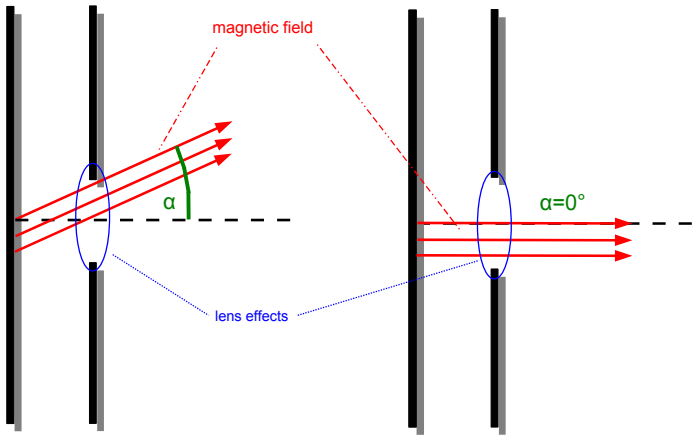

Figure 5.8: Axial symmetric schematic of a parallel plate capacitor including an aperture. Magnetic field lines pass the aperture in different zones and distances to the plate. The plate is on negative potential and affects the kinetic energy of an electron. Since the electrons are guided along these magnetic field lines, they are affected by aperture effects depending on their starting position.

An aperture applied in the front plate, see figure 5.8, enabling the electron to leave the homogeneous electric field, works as an electrostatic lens. Depending on the potential and polarity, electron beams are basically focused or defocused, their trajectory is altered. In this geometry the adiabatic tracking in medium strong magnetic fields will prohibit a deviation of the trajectory. Of course the existence and shape of an aperture affect the electron and it is self evident that the effect correlates with the minimal distance between electron and electrode. The electron property, affected by the lens while guided adiabatically, is the transversal energy $E_{\perp}$. An important feature is the phase of the gyration motion at the location of the aperture.

Figure 5.9 explains this connection, an electron closing in on some negative potential is decelerated and vice versa an electron that veers away from

[2]high magnetic fields may be obtained with an auxiliary coil

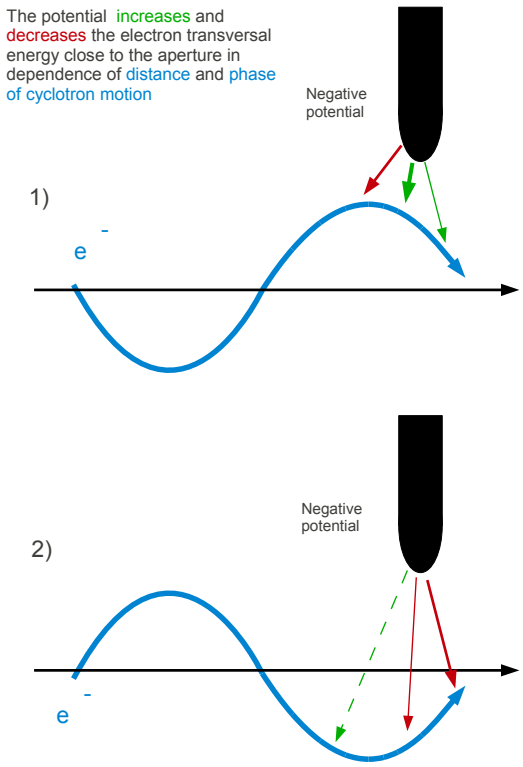

Figure 5.9: Schematic: Two electrons with different phases pass an electrostatic aperture on negative potential. The effect of an aperture depends on the phase of adiabatic motion and can both in- and decrease transversal energy.

the plate is accelerated. The comparatively large longitudinal energy is decreased and increased after passing, thus largely unaffected by the aperture. The transversal energy however is de- or increased depending on the gyration motion phase and can be both in- and decreased. The fact that the electric repulsion is correlated with the distance of electron to plate make the area closest to the aperture critical for the transversal energy development when passing an aperture. It is self explanatory that the wavelength of the oscillation needs to be of the according order of magnitude, so that the effect does not average out.

Example simulations for electrons, that are affected by an aperture are shown in Figure 5.10. The green line belongs to an electron, that is passing the aperture close to the center. It is largely unaffected in contrast to electrons that pass the aperture close to the plate (pink, blue). Since the two latter electrons were started at different positions, they reach the plate at different states of gyration. The amount of transversal energy of both

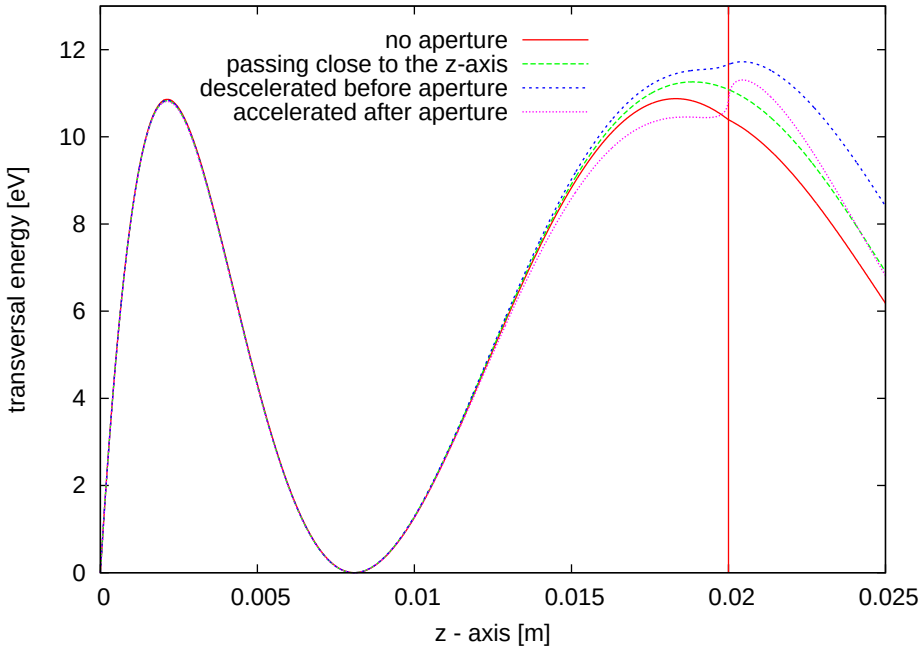

Figure 5.10: The transversal energy of four different electrons is plotted against the z-axis. The front plate position at $z = 0.02m$ is depicted with a vertical red line, the back plate is positioned at $z = 0m$. $\Delta U = 2\,\mathrm{kV}$, $\alpha = 20\,^\circ$, $B = 200\,\mathrm{G}$, aperture diameter 5 mm.

electrons is already altered close before the aperture. It should be noted, that the distances between electron and plate in the aperture plane and thus the effect on both electrons are comparable. An interesting feature is the transversal energy development in the aperture plane. The aperture effect on the blue line is visible but small, while the transversal energy (pink line) is largely increased in the aperture plane. This second electron was decelerate before the aperture and re-accelerated after passing. It should be noted, that the sole existence of an aperture increased the transversal energy $E_\perp$ of passing electrons[3]. Figure 5.11 illustrates the transversal energy shift in dependence of the minimal distance to the plate. It is obvious that electrons can gain and lose transversal energy by passing the aperture and the effects is not uniquely defined for a given plate to electron distance without further knowledge.

The emerging problem for the construction of an angular selective source is that an ensemble of various electrons, passing the aperture on different trajectories, has a transversal energy distribution. Since the idea is to create monoenergetic and monoangular electrons with a set angle $\theta_{\mathrm{solenoid}}$, the re-

[3] in comparison to the case of an ideal parallel plate capacitor without an aperture

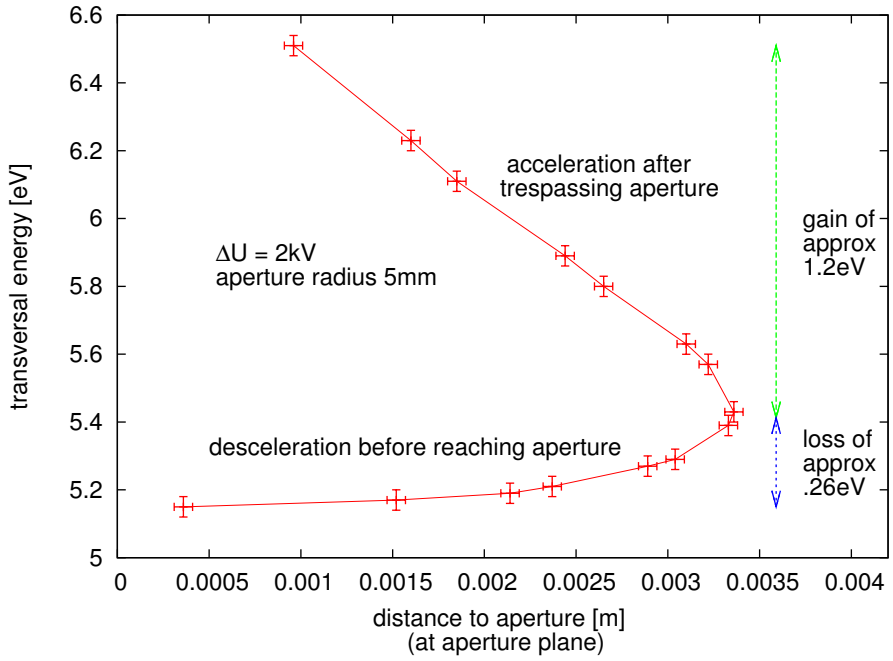

Figure 5.11: The transversal energy $E_{\perp,\infty}$ of an electron is plotted against the distance to the aperture at $z = 0.02m$. An electron, passing close to the aperture, can gain or lose transversal energy (compare figure 5.9) in comparison to a relatively unaffected pass close at the center.

sulting distribution is too broad. For example the simulation, see figure 5.12, shows that electrons gain a transversal energy distribution after implementation of an aperture of $\oslash_{\text{apt}} = 5\,\text{mm}$ diameter. The energy spread width amounts $\approx 1\,\text{eV}$ at a mean of $5.8\,\text{eV}$, i.e. $\approx 20\,\%$.

A larger aperture diameter increases the E-field inhomogeneity and punch through, smaller diameters reduce the absolute but increase the relative uncertainty, since the relative impact of the area close to the aperture is increased. In the following simulations a rounded aperture diameter of $2\,\text{mm} \leq r_{\text{aperture}} \leq 5\,\text{mm}$ proved to be a good compromise.

Plate diameters

The maximum plate diameter is restricted by the dimensions of the ellipsometry chamber at Mainz. To avoid contact or discharges the maximum radius was set to $r_{\text{plate,max}} = 5.0\,\text{cm}$. The plate radius defines the electric field, smaller radii result in a deviation from an ideal parallel plate capacitor.

In figure 5.13 simulations concerning the plate diameter are presented. Besides the energy distribution, that is caused by the aperture, an energy segregation is apparent. The transversal energies are separated depending

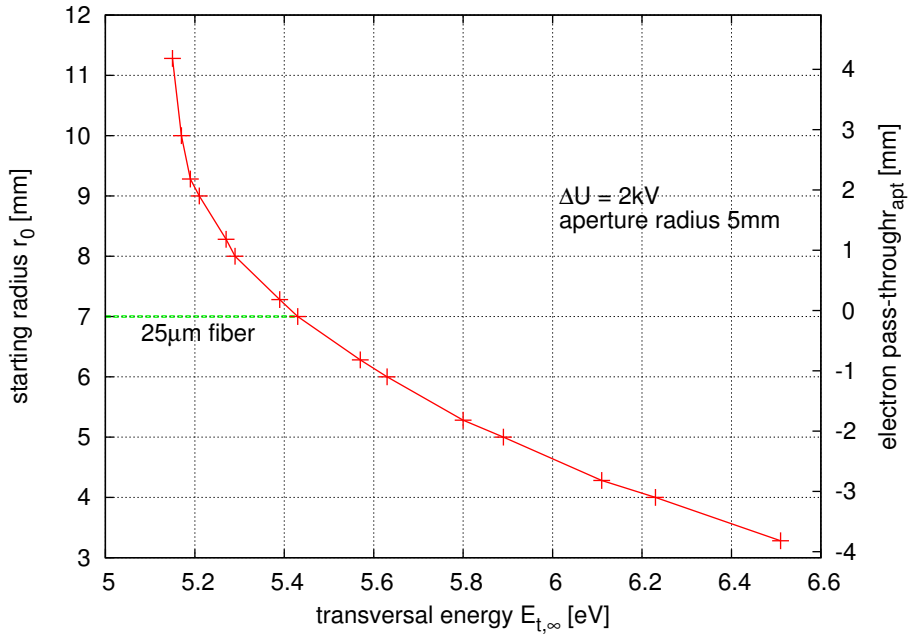

Figure 5.12: The starting position, namely r_{start}, is plotted against the transversal energy $E_{\perp,\infty}$ after passing an aperture. The transversal energy gain or loss depends on the phase, when the electron passes the aperture, thus the starting radius affects the transversal energy indirect.

on the plate diameter. Figure 5.14 shows the transversal energy gain on the first 1.5 cm. To reduce the presence of divergent fields, the plate diameter was set to the maximum feasible value of $\oslash_{\text{plate}} = 10\,\text{cm}$.

5.2.3 Decrease of the spread of $E_\perp$

Reduction of the photon emitting area

One way to significantly decrease the spread of $E_\perp$ is to reduce the electron emitting area to a small, well defined spot, see figure 5.12. The phase of the motion only depends on the constellation of the E and B fields and electron starting position. Thus with a given set of variables [ΔU, d, B, α, $\oslash_{\text{apt}}$] the phase of motion of an electron[4] only depends on the electron starting position $[x_0, y_0, z_{\text{plate}}]$. For now a possible electron starting energy due to the photoelectric effect is neglected. In figure 5.12 the transversal energy $E_\perp$ of an electron is clearly affected by the aperture and varies between 5.1 eV and 6.5 eV. A correlation between r and $E_\perp$ is also obvious. By reducing the electron emitting area to a small radius of some ten to hundred μm, denoted

[4] and thus the effect on $E_\perp$

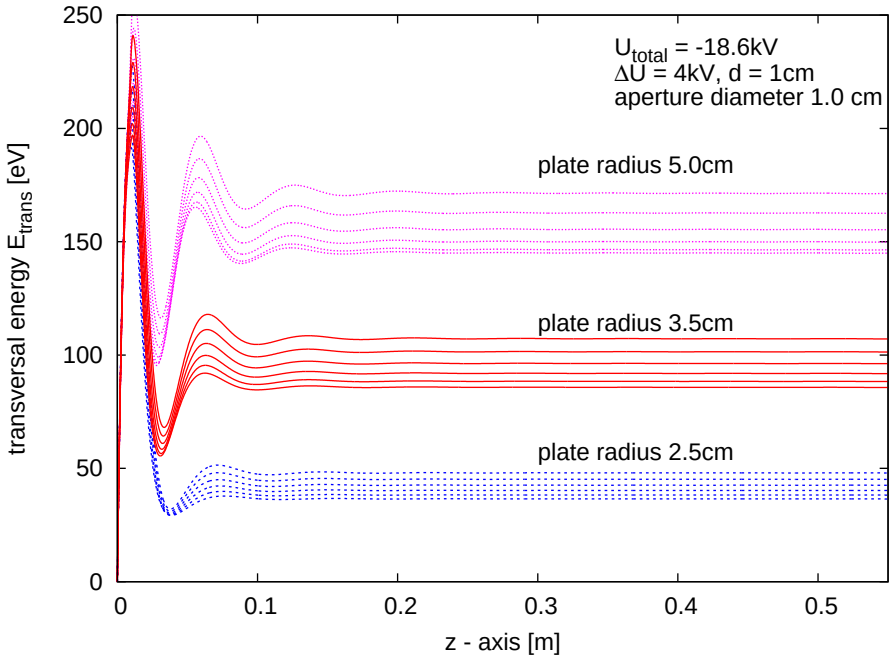

Figure 5.13: For three geometries with distinct plate radii between 2.5 cm and 5.0 cm, electrons were started on different radii. The electron starting radius correlates with the aperture effect on transversal energies. Additionally an energy segregation is caused depending on plate dimensions.

by the green line, the uncertainty becomes almost negligible.

Implementation of optical light guides

The reduction of the irradiated area leads to considerations similar to the previous electron source. External illumination, for example by a laser, may be feasible. The problem is, again, the light emitting spot needs to be small and well known for reproducible measurements. It is technically challenging to illuminate the spot from aside, shielded by two plates. The possible illumination angles, reduced by the four fixed uv-transparent windows available at the Mainz laboratory further increase the challenges. Additionally the required safety precaution, connected to the application of a laser, would impede work at the laboratory.

The implementation of optical light guides coated with a suitable metal is a proven principle. Serving as defined, light emitting spots in the backplate, they enable reproducible measurements. Of course the drawback are lower electron count rates, resulting in increased measurement times. Additionally the fibers are a fragile element of the source and need protection from damage, which would render the electron gun useless.

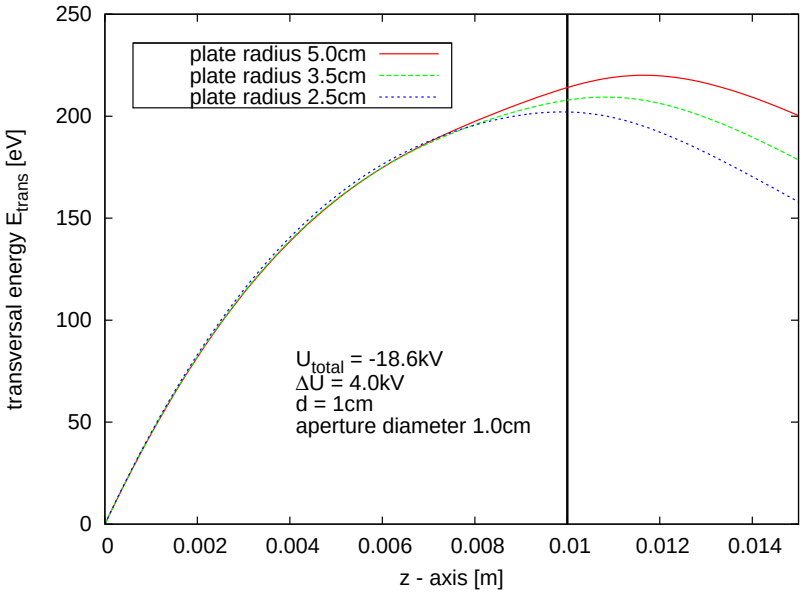

(a) Transversal energy, zoomed

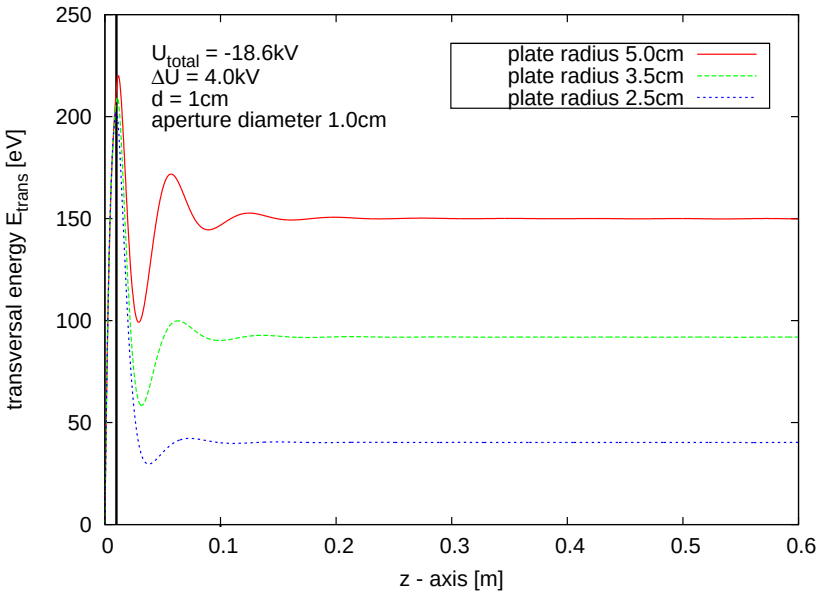

(b) Transversal energy

Figure 5.14: These figures illustrate electron transversal energy development and the electric potential along the electron trajectory for three plates with different plate diameters. The transversal energy oscillation of the three electrons is at a maximum upon reaching the front plate. The electric field of a parallel plate capacitor with smaller plate diameters is more divergent. In this case, at the $E_{\perp}(\hat{z})$ maximum, the electron phase and the divergency of the electric field cause a segregation of transversal energies.

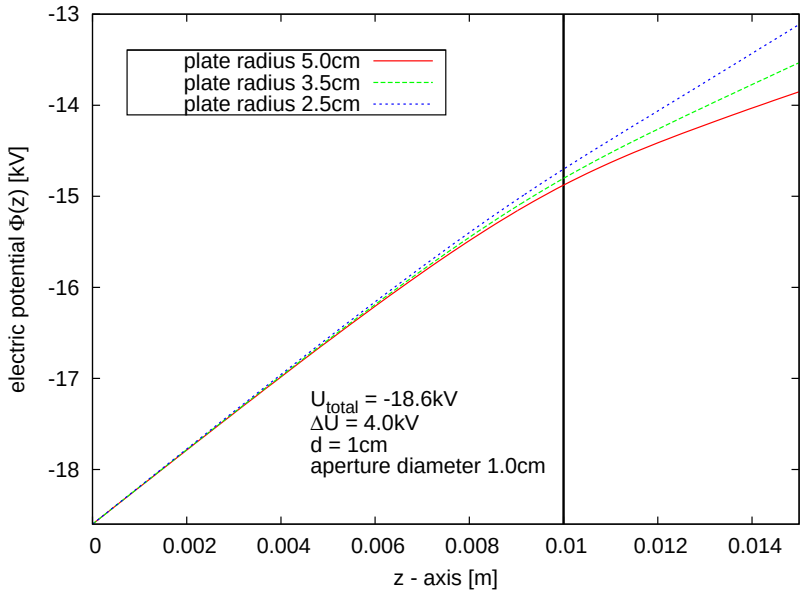

(a) Electric potential, zoomed

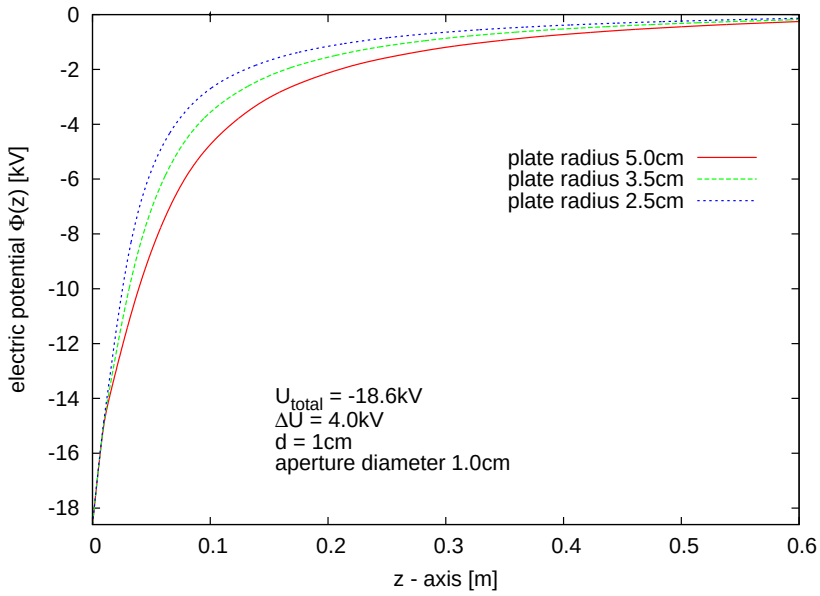

(b) Electric potential

Figure 5.15: fig. 5.14 continued

Angular distribution of θ_{solenoid}

With implemented fibers the emitting spot then is a fixed circular area defined by the fiber core position $[r, 0, z_{\text{plate}}]$ and diameter d_{fiber}. For simulations not only the r, but the (x_0, y_0) starting position distribution now has to be regarded. In the following simulations, the electrons are tracked from the backplate through the aperture and over a distance of 55 cm. The electric field is weak at $z = 0.55\,\text{m}$ and transversal energy oscillations have almost completely disappeared, leaving a small systematical error $\leq 0.5\,\%$. Tracking over larger distances basically increases computation times without noticeable improvement.

The electron starting positions are equally distributed over a circular area with a diameter of $d_{\text{fiber}} = 25\mu m$. For the purpose of reduced computation times, a starting energy distribution due to the photoelectric effect is still neglected.

The simulations are shown in figure 5.16. By reducing the electron starting area, the angular distribution has been reduced significantly. For example for electrons with $\theta_{\text{solenoid}} \approx 60\,^\circ$ it now amounts to about $\Delta\theta \approx \pm 0.35\,^\circ$ and electrons at $\theta_{\text{solenoid}} \approx 90\,^\circ$ have a spread $\Delta\theta$ of up to $\pm 4\,^\circ$. The electrons pass the plate at high angles $\alpha = 16\,^\circ$ and rather off axis at the aperture plane, resulting in larger lens effects. By using multiple fibers on different radii r the spread is expected to be decreased. Also by pushing a fraction of the distribution to values $\theta_{\text{solenoid}} \geqq 90\,^\circ$, the spread of the imaged electrons is further cut. It should be noted, that the spreads scale with the fiber diameter d_{fiber}. Regarding that these simulations contain systematical errors due to the approximation of variables, like the magnetic field, and as time was of the essence, we regarded these results as sufficient. More detailed investigations were done for a realistic magnetic field.

Similar to the previous electron source, the application of three light guides, offers some benefits. The emitting area needs to be close to the z-axis to create electron with electron angles close to $\theta_{\text{solenoid}} = 0\,^\circ$. Hence one fiber needs to be positioned at $r = 0\,\text{mm}$, so that electrons will pass the aperture close to the center and the gain of transversal energy is small (figure 5.8). All simulations for off-axis fibers show that, even for $\alpha = 0\,^\circ$, electrons will gain some transversal energy and render the gun unable to create electrons close to $\theta_{\text{solenoid}} = 0\,^\circ$. Vice versa for larger angles α the fiber needs to be off axis so that the electrons pass the aperture close to the aperture center (small $E_\perp$ gain due to lens effects) and reduce the spreads, analog to figure 5.8. The three equidistant radii used are $r_1 = 0.0\,\text{mm}$, $r_2 = 0.9\,\text{mm}$ and $r_3 = 1.8\,\text{mm}$.

5.2.4 Summary

Figure 5.17 shows some representative simulation results for the parameters:

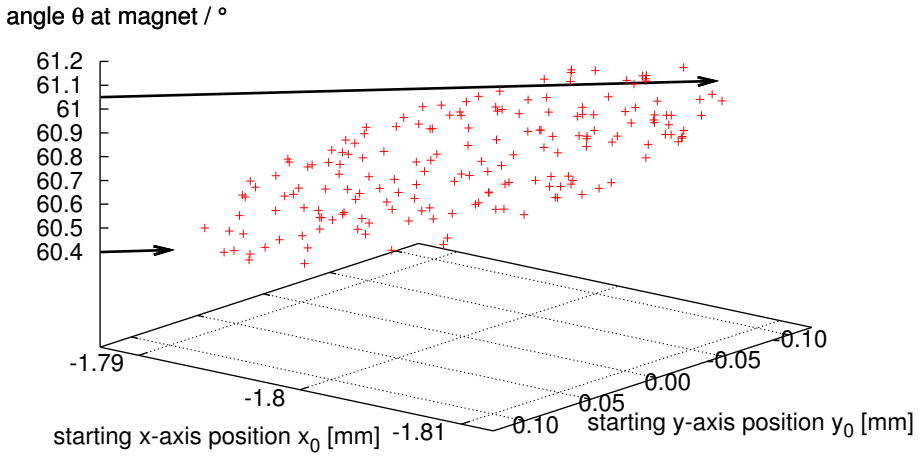

(a) $\Delta U = 2.8\text{kV}$, $B = 200\text{G}$

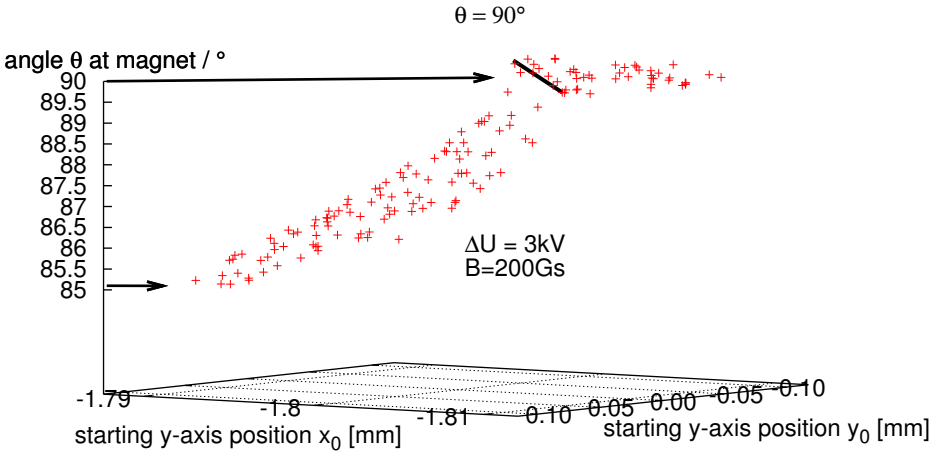

(b) $\Delta U = 3.0\text{kV}$, $B = 200\text{G}$

Figure 5.16: Electrons were started on random locations on the fiber core surface. The angle θ_{solenoid} is plotted against the electron's starting position. The angular distribution, or spread of $\theta_{solenoid}$ for one fiber, depends on and increases with $\theta_{solenoid}$. Close to $\theta_{\text{solenoid}} = 90\,^\circ$, the distribution has $\Delta\theta_{\text{solenoid}} \approx \pm 4\,^\circ$ and at $\theta_{\text{solenoid}} = 60.8\,^\circ$ $\Delta\theta_{\text{solenoid}} \approx \pm .35\,^\circ$.

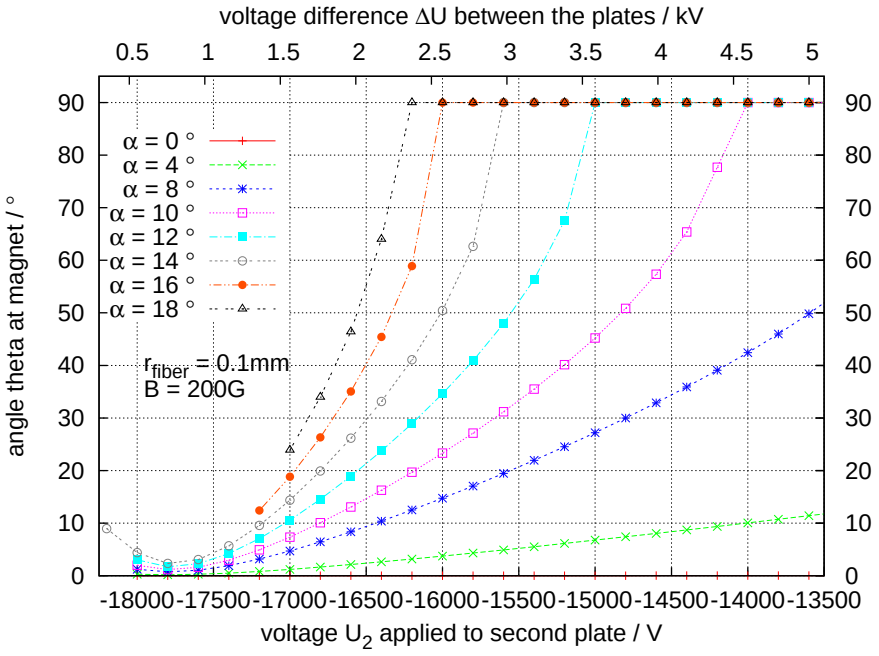

(a) Inner fiber r_1 =0.1mm

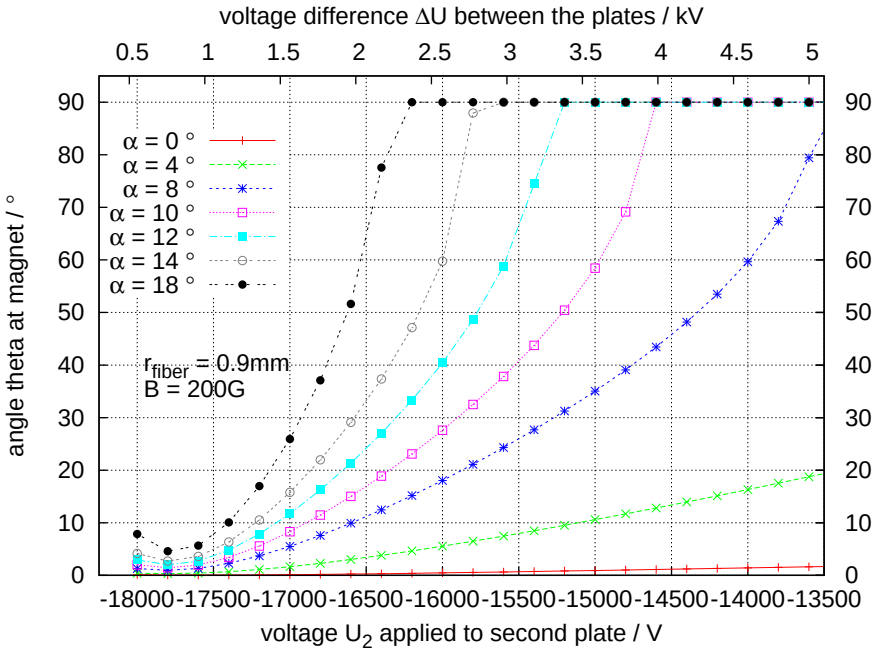

(b) Middle fiber r_2 =0.9mm

Figure 5.17: For the two fibers at $r_1 = 0.1\,\mathrm{mm}$ and $r_2 = 0.9\,\mathrm{mm}$ and angles $0\,^\circ \leq \alpha \leq 18\,^\circ$, the electron angle at the solenoid $\theta_{\mathrm{solenoid}}$ is plotted against the front plate potential U_{front}. The difference potential $\Delta U = U_{\mathrm{front}} - U_{\mathrm{front}}$ is shown on the upper x-axis. (explanation: see text)

- $B = 200\,\mathrm{G}$
- back plate potential $U_{\mathrm{total}} = -18.6\,\mathrm{keV}$
- angles α from $0\,^\circ$ to $18\,^\circ$
- difference potential $0\,\mathrm{kV} \leq \Delta U \leq 5\,\mathrm{kV}$

The angles $\theta_{\mathrm{solenoid}}$ at magnet are plotted against the voltage U_{front} at the front plate. The different lines depict simulations for different angles α. For example the blue line corresponds to $\alpha = 8\,^\circ$. It describes the gained electron angle $\theta_{\mathrm{solenoid}}$ at the magnet in dependence of the applied voltage $U_{\mathrm{front}} = U_{\mathrm{total}} + \Delta U$. It is obvious for all angles α, that $\theta_{\mathrm{solenoid}}$ scales with ΔU with a exception at low difference voltages, where a local minimum at larger angles α becomes visible. This effect causing the minimum was discussed in the summary of section 5.2.1 and is due to the electron phase of motion.

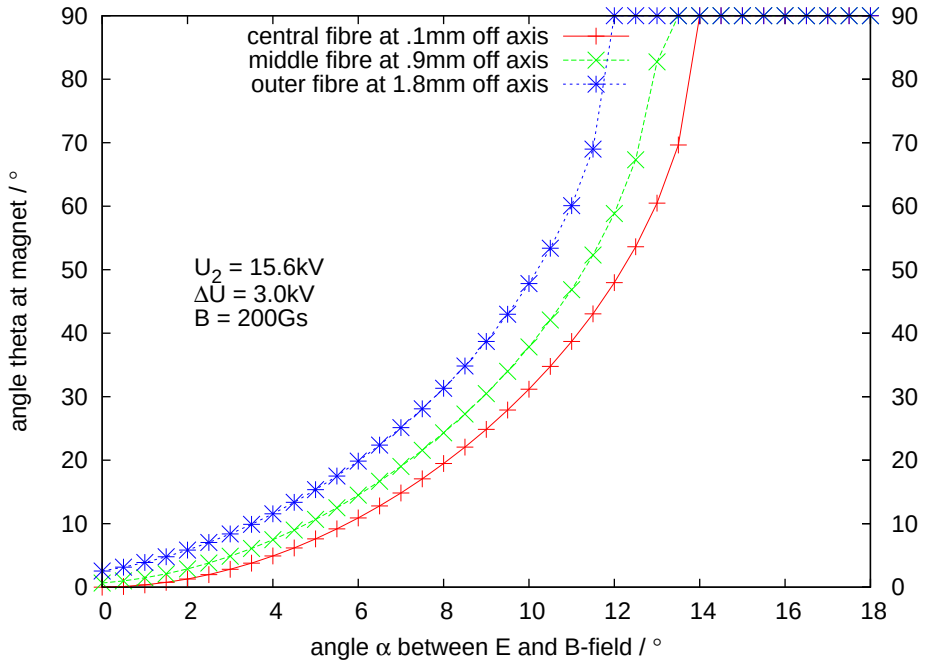

Figure 5.18: For a fixed difference potential $\Delta U = 3.0\,\mathrm{kV}$ and three fibers, namely electron starting positions, at $r_1 = 0.1\,\mathrm{mm}$, $r_2 = 0.9\,\mathrm{mm}$, $r_3 = 1.8\,\mathrm{mm}$, the angle $\theta_{\mathrm{solenoid}}$ is plotted against α. At $\alpha = 0$ only the central fiber ($r_1 = 0.1\,\mathrm{mm}$) can create photoelectrons close to $\theta_{\mathrm{solenoid}} = 0\,^\circ$. Electrons created at negative α are not regarded, since these would suffer from higher uncertainties due to the aperture. For the same reason the outer fibers are necessary to create photoelectrons at higher α with reduced energy spread.

For both off-axis fibers $\theta = 0\,^\circ$ electrons can not be created, even with a setting $\alpha = 0\,^\circ$. This effect first became visible, when the aperture was applied. All electrons passing the aperture off axis will gain a distinct amount of transversal energy, thus the inner fiber at $r_1 = 0.1\,\mathrm{mm}$ is necessary to create electrons with no transversal energy. This connection will become more clear considering the following. Besides choosing a set angle α and varying the potential difference ΔU, another possible measurement method is to set ΔU to a fixed value and alternate α. Figure 5.18 shows the corresponding plot for $\Delta U = 3\,\mathrm{kV}$ in a magnetic field $B = 200\,\mathrm{G}$ for all three fibers. It becomes evident, that the innermost fiber is required to create electrons with no transversal energies. Regarding the last plot one might question the need for additional fibers. These fibers are necessary for an energy spread reduction at larger angles α, which is is not illustrated in these plots.

All simulations for magnetic fields between $160\,\mathrm{G} \leq B \leq 300\,\mathrm{G}$ showed very similar results, differing only in details like incline of lines and position and shape of the $E_\perp$ minimum. It was decided that these results are sufficient to construct the electron source and leave more exact, but time consuming simulations for the analysis of the measurements.

5.3 The electron gun design

Geometry

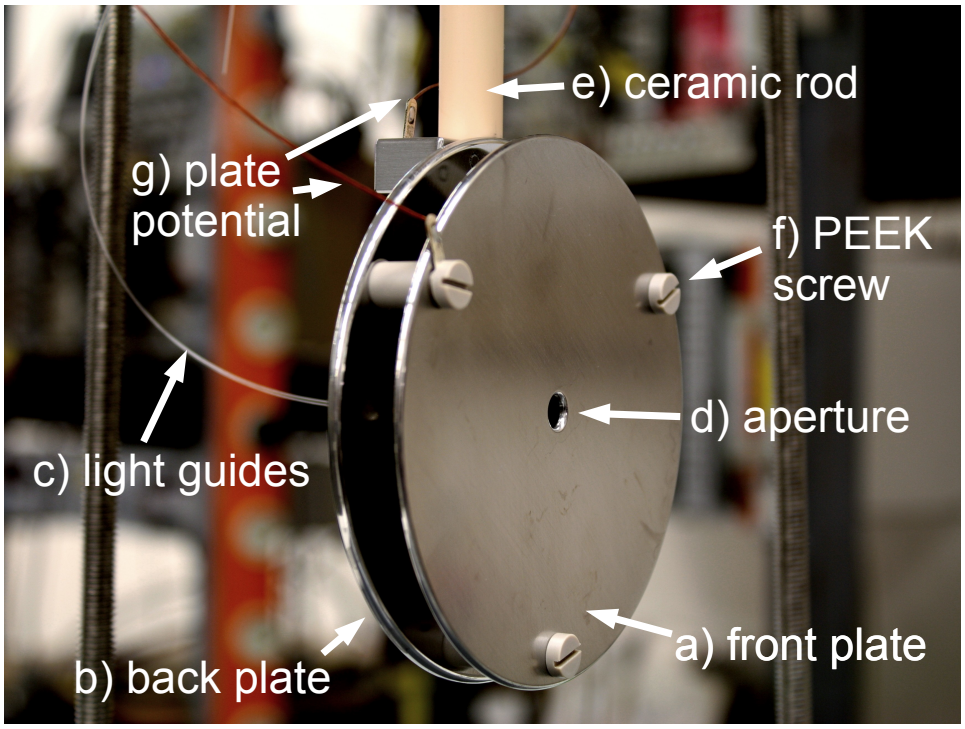

Figure 5.19: Photograph of the electron source, before implementation at the spectrometer at Mainz. The two parallel plates *(a)* and *(b)* are kept at a constant distance $d = 1\,\mathrm{cm}$ by *PEEK* screws *(f)*. In the front plate is an aperture of diameter $\oslash_{\mathrm{apt}} = 6\,\mathrm{mm}$ *(d)*. The condensed metal layer on the back plate is irradiated from behind by two (one of the three fibers broke) UV transparent fibers *(c)*. The plates lie on high voltages of up to 20 kV, supplied by kapton insulated wires *(g)*. A ceramic rod holds the plates in the center of the vacuum chamber and insulates the back plate from ground.

The electron gun design is customized to the Mainz' spectrometer environment. The vacuum chamber geometry (figure 2.4 and 2.5) reduces the maximum plate diameter to up to $\oslash_{\mathrm{plate}} = 100\,\mathrm{mm}$.

The plates are made of stainless steel with a thickness $d_{\mathrm{plate}} = 2\,\mathrm{mm}$. The plate distance is $d = 10\,\mathrm{mm}$, in accordance to the simulations the plates are kept at constant distance[5]. The aperture in the front plate has a diameter $\oslash_{\mathrm{aperture}} = 6\,\mathrm{mm}$.

The back plate is mounted on a ceramic rod, insulating the plates from ground potential. A 5×CF35 flange is mounted on the ellipsometry cham-

[5]held by three PEEK[6] screws capable for the use in high vacuum

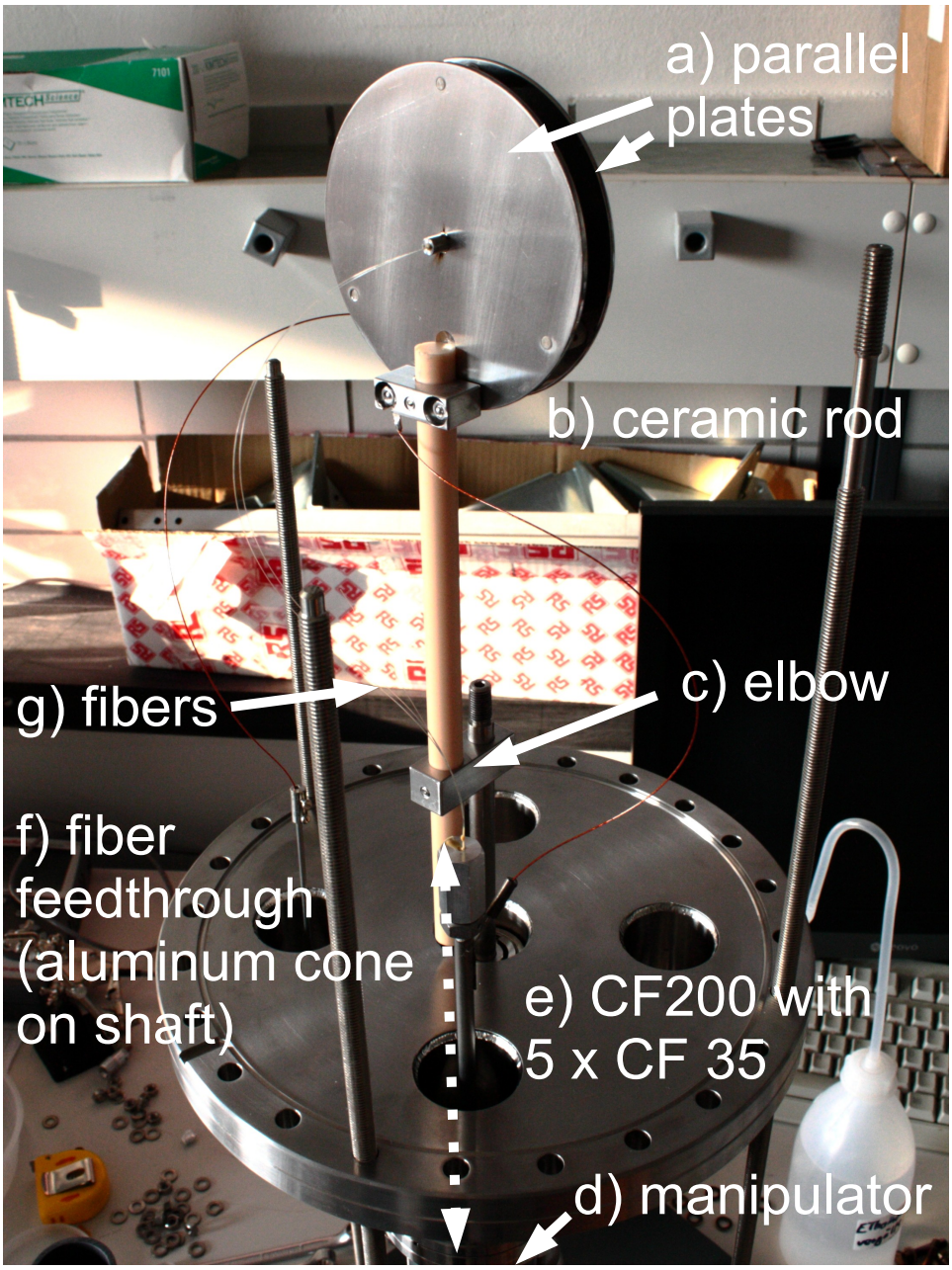

Figure 5.20: Photograph of the electron source during construction at Münster. The two parallel plates *(a)* are mounted on a ceramic rod *(b)*, which is connected over an elbow *(c)* to a manipulator *(d)*. The manipulator and two high voltage feedthroughs are mounted on three of the five CF 35 flanges (*(e)* seen from below). One of the HV feedthroughs is hollow *(f)* and carries the fibers *(g)* into the vacuum chamber.

ber CF200 Flange. The central CF35 carries a manipulator, connected to the ceramic rod, that allows aperture-centered rotation over an elbow and enables a precise setting of α, in steps of $0.1\,^\circ$.

Two CF35 high voltage feedthroughs designed for up to 30 kV, are necessary to set the plate on the potentials U_{back} and $U_{\text{front}} = U_{\text{back}} + \Delta U$. One of these feedthroughs was already in use at the previous electron-gun (chapter 4). This feedtrough was hollowed to carry the fibers into the spectrometer.

Vacuum sealing

The application of optical feedthroughs or windows and the recoupling into optical fibers in vacuum are technically challenging. Due to previous experiences (chapter 4) we chose to conduct the coupling of UV-light into the fibers outside the spectrometer and feed the fibers into the vacuum chamber.

The vacuum seal is an aluminum cone (figure 5.20 *(d)*), the fibers were fed through, that is then filled with epoxy *H20* over a distance of about 1 cm. The cone then is screwed on the hollow HV-feedthrough, with a rubber ring additionally improving the sealing. This very simple but effective setup was tested at Münster, where it sustained pressures of $p < 5 \cdot 10^{-7}$ mbar after about 1 hour of evacuation.

5.3.1 Cathode materials

Appropriate cathode materials were subject of section 2.2.3. To recapitulate considered metals: there are namely *Au*, *Ag*, *Co*, *Cr* and *stainless steel*. The workfunction Θ_{Au} of gold proved to be too high to create photoelectrons with the applied UV-diodes. Thus *Ag*, *Co* and stainless steel are preferable, since all were validated as suitable metals.

This electron gun is meant to prove the principle of angular selected electron provision for the KATRIN spectrometer. Most of the previous electron source experiments were performed with an *Ag* layer. We avoided the application of *stainless steel*, since steel is an alloy. The allocation of different elements may result in inhomogeneous compositions across the fiber. The metal work functions in contrast are required to be as homogeneous as possible over the three fiber surfaces. Hence silver was the reliable choice; a silver layer was evaporated with a density of $35(\pm 5)\,\mu\text{g}/\text{cm}^2$.

5.3.2 Implementation of fibers in the backplate

The implementation of fibers, especially the inner fiber, requires a positioning precision of $\leq 100\,\mu$m. The inner fiber is essential to create electrons with $\theta_{\text{solenoid}} = 0$. If the fiber is off axis, the electrons will also pass the aperture off axis and gain transversal energies.

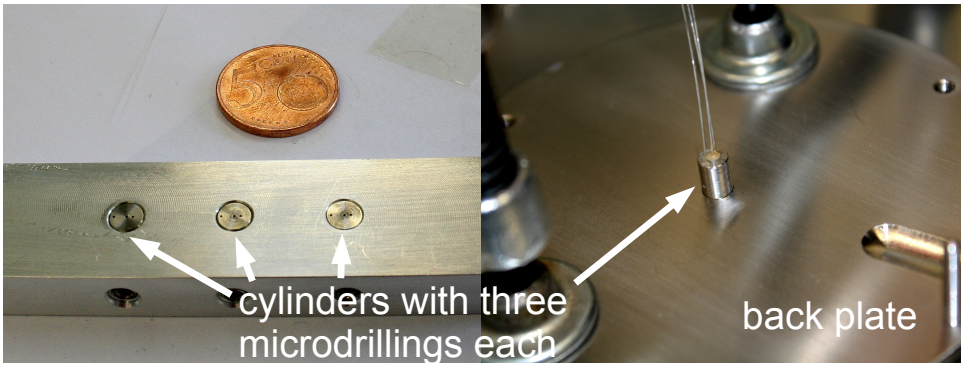

Figure 5.21: Photographs of cylinders with three microdrillings, used for high precision positioning of the fibers. *Left:* Three cylinders in comparison to a European 5 cent coin. *Right:* Cylinder (equipped with 3 fibers), attached to the back plate.

Precise positioning was achieved by drilling three micro-drillings, with a diameter $\oslash_{\text{micro}} = 300\,\mu\text{m}$ slightly larger than the outer diameter of the applied fibers ($\approx 250\,\mu\text{m}$), through a stainless steel cylinder $\oslash_{\text{cyl}} = 3\,\text{mm}$ (figure 5.21). The three drillings at the radii $r_1 = 0.0\,\text{mm}$, $r_2 = 0.9\,\text{mm}$ and $r_3 = 1.8\,\text{mm}$ lie in one line, with the second and third drilling in opposite directions of the central drilling (figure 5.22). This is analog to the positioning of fibers in the previous source and increases distances between the outer two drillings and reduces possible surface effects and unevenness.

After stripping[7] and cleaving[8] of the fiber ends, these were fed through and glued into the drilling, using *H20* epoxy. After multiple iterations of polishing, the surface and fibers were examined under the microscope. Photos are provided in figure 5.23.

A silver layer with a density of about $35(\pm 5)\,\mu\text{g/cm}^2$ was then evaporated over the whole cylinder surface. Now the device for precise positioning is to distinguish the relative position of the fiber relative to the micro-drilling and then to position the cylinder within the backplate. The positioning of the drill holes in the cylinder and backplate is more precise than the positioning of a fiber within the micro-drillings. Hence the positioning precision of the inner fiber relative to the aperture is improved significantly.

5.3.3 Optical light guides

The light guides used in the electron gun, are provided by j-fiber GmbH, Jena. These High-Power-Small-Core (HSPC) fibers contain a high *OH* per-

[7] Stripping is a common technique for removal of cladding and coating and necessary for cleaving

[8] The stripped fiber core is bend and slightly scored with a sharp diamond tip. The core eventually breaks and leaves an even surface.

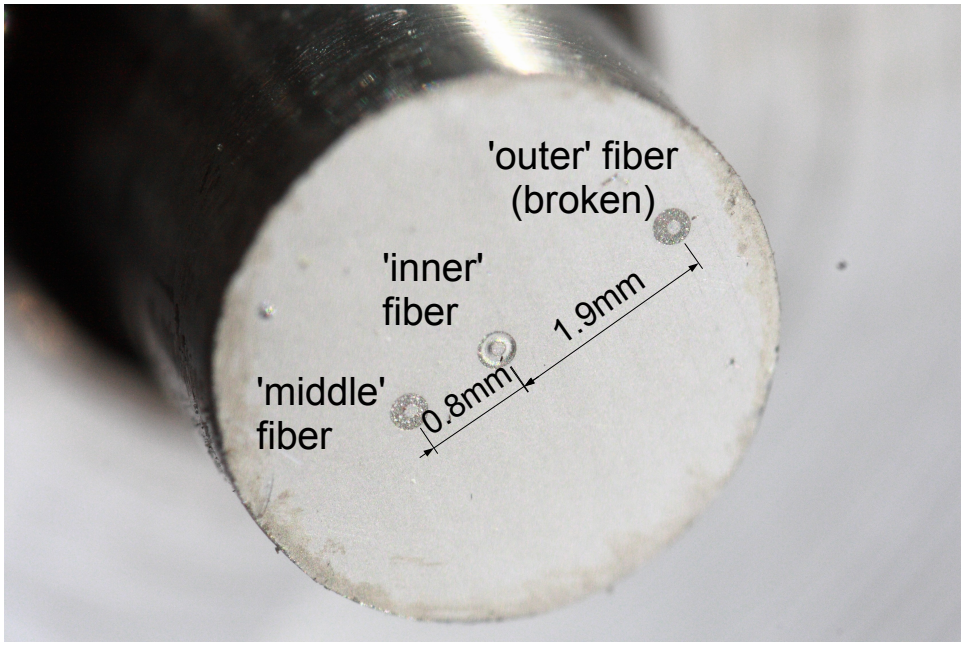

Figure 5.22: Macro-photography of the cylinder: The fibers were glued, polished and covered with a silver layer.

centage and are designed for high power transmission in the near-UV and visible range.

Figure 4.6 illustrates the typical spectral attenuation in $^{dB}/_{km}$. Since the fiber length amounts about 1 m, the transmittance of UV-light at 265 nm and 255 nm is still high, as proven at experiments with the previous electron source.

The fiber FEQ100-15000100 (15 / 125 / 250) with a core diameter of $\oslash_{\text{core}} = 15\,\mu$m is employed[9]. At the previous source (chapter 4) the electron yield, with $\oslash_{\text{core}} = 98\,\mu$m, was sufficiently high and since the angular spread $\Delta\theta_{\text{solenoid}}$ scales linear with the radius according to simulations, a fiber with an about six times smaller core $\oslash_{\text{core}} = 15\,\mu$m was chosen. The drawback is, that the intensity and thus the electron yield is assumed to correlate linear with the electron emitting area $A_{\text{fiber}} = \frac{\pi}{4} \cdot \oslash^2_{\text{core}}$. Hence the photoelectron count rates will likely be reduced with the square of the fiber core diameter.

The light guide, a step index fiber, is equipped with *FCC-12* acrylate coating. This buffer is advertised as an enhanced coating material, guaranteeing long-term performance and reliability. The drawback is that *FCC-12* coating has a specified operation temperature between -60 °C and 85 °C, meaning that baking out is prohibited and the epoxy glue, holding the fiber,

[9] in contrast to the former used *FAQS00-98105022* (98 / 145 / 245) with a $\oslash_{\text{core}} = 98\,\mu$m

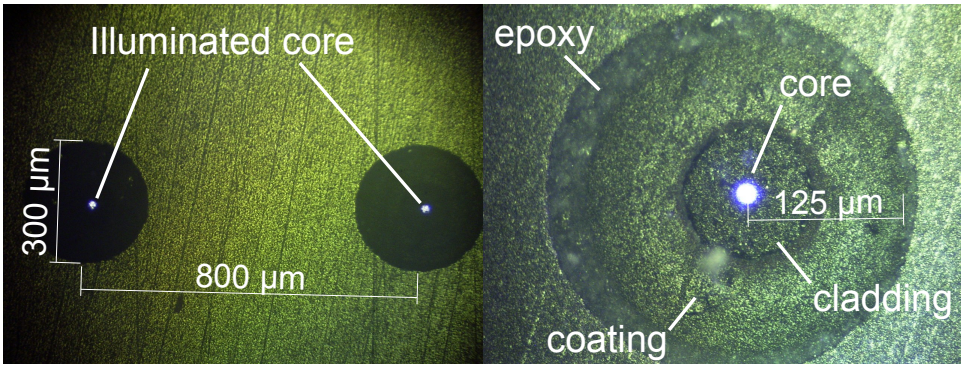

Figure 5.23: Microscope-enhanced photographs of the glued and polished fibers. *Left:* The 'inner' (left) and 'middle' fiber (right) in the drillings. The core is made visible, by illuminating the other fiber end. *Right:* With further magnification the fiber core, cladding and coating as well as the epoxy H20 glue become observable.

needs to hardened within this temperature range.

The gluing of a fiber with epoxy has the disadvantage of making the otherwise resilient coating brittle. Consequently during the preparation of the electron gun, the outermost fiber at $r_3 = 0.18\,\mathrm{mm}$ was damaged and useless throughout the experiments. A similar incident happened with the fiber-electron-gun. A thorough investigation of suitable glues might be of interest.

5.3.4 Optical coupling

Experiments with the previous electron source concerning optical couplings between UV-diodes and light guides showed, that the electron yield by simply placing the diodes in short distances of 1 mm and less in front of the fiber was a sufficient mechanism. Most problems were caused by the fact, that one diode was used to alternately illuminate three fibers and the coupling had to be established and tuned every time the fibers were switched. As a result, we now used three similar diodes for the new electron source with a once established and then fixed optical coupling.

A new array for optical coupling was designed, as shown in figure 5.24. The three ends of the fibers are clamped in a metal jacket and screwed on the lower side of the array under the diode mounts. The idea was to establish the coupling once and then fix the diodes. This setup will require further improvements in the future, since low electron count rates induced problems. Low electron count rates are linked to increased measurement times. While in former experiments the micrometer screw seemed rather hindering, now with a lack of micrometer screws or similar devices these count rates impeded proper setup of the coupling. The photoelectron count

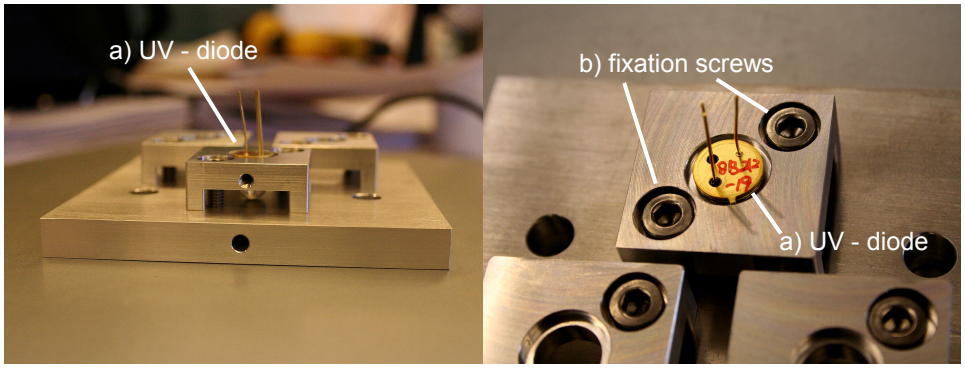

Figure 5.24: The optical coupling array for three UV diodes (a). The fiber ends are fed through the bottom plate. The diode position is adjusted, until photoelectron count rates are at a maximum, and then the diode is fixed with the according screws (b).

rate of one fiber was inferior to the other throughout the whole experiment despite all efforts to improve the coupling and the reason could not be found (analog to section 4.2.2).

5.3.5 The high voltage supply

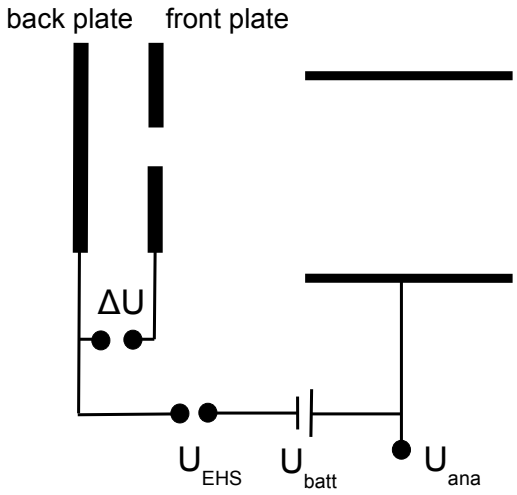

Figure 5.25: Wiring diagram for the measurements at Mainz.

Several high voltage supplies were necessary to perform the experiment. The according wiring diagram is shown in figure 5.25.

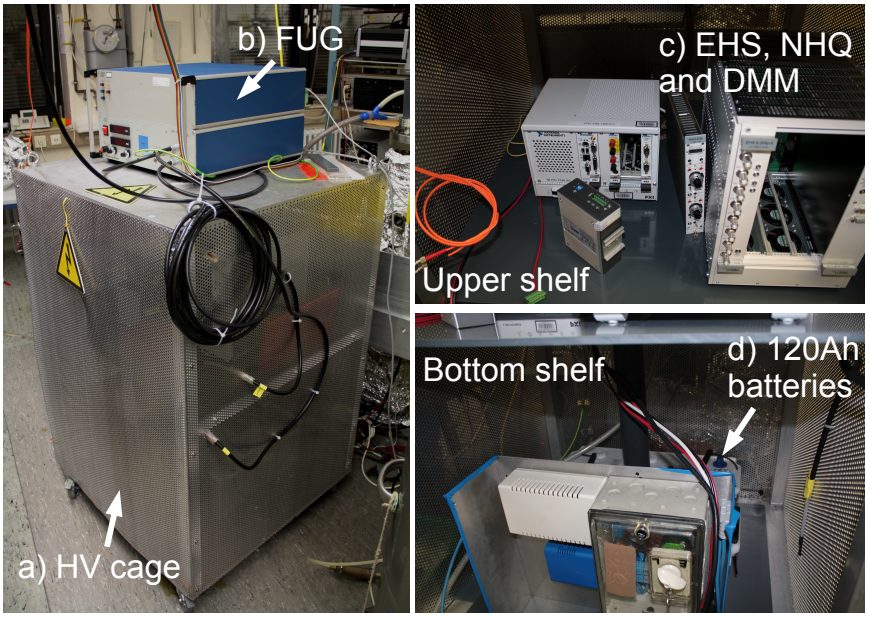

Figure 5.26: Photography of the HV cage. *Left:* The HV cage (a) and the FUG voltage supply *(b)* for U_{tot}. *Top right:* upper shelf with the PXI System, EHS, NHQ and the digital multimeter *(c)*. *Bottom right:* The 120 Ah batteries *(d)* behind the instruments power supply.

1. The spectrometer requires a voltage $U_{\mathrm{ana}} = -18.6\,\mathrm{kV}$ equivalent to the tritium spectrum end-point energy. The wire electrodes and thus the analyzing plane will lie on this potential and define the longitudinal energy threshold of the high pass MAC-E filter.

2. A second high voltage potential is necessary for the back plate to define the total kinetic electron energy. As an alternative the back plate is set on the analyzing plane potential U_{ana} plus a constant potential offset $U_{\mathrm{batt}} = 96.04\,\mathrm{V}$, supplied by an array of batteries[10] and a second voltage supply $0\,\mathrm{V} \geq U_{\mathrm{EHS}} \geq -500\,\mathrm{V}$. This enables the scanning of the back plate potential against spectrometer. This offers higher precision for transmission function measurements, because the source U_{EHS} provided by a *ISEG EHS8205p-K* has a precision of $\delta U_{\mathrm{bp}} = 10\,\mathrm{mV}$. The battery voltage U_{batt} was frequently read out, as it directly affects the transmission function position.

3. The third essential voltage source provides the potential difference ΔU between the plates. This potential does not need such high accuracy as the back plate potential, since it has no effect on the total energy and the effect of the uncertainty on the electron transversal energies

[10] the offset is to be measured regularly to ensure reproducibility

is so small that it is not measurable. The applied voltage source is a *ISEG NHQ226L* with a maximum voltage output of $U_{\mathrm{NHQ,max}} = 5\,\mathrm{kV}$ and a precision of $\delta U_{\mathrm{NHQ}} = 100\,\mathrm{mV}$.

All voltages except U_{ana} were set and read by a *labview*-based graphical user interface. To distinguish the precise potential difference between plate and analyzing plane, a PXI digital multimeter (DMM) with an 8-digit precision was integrated and read out by the software.

The voltage supplies were set in a high voltage cage, as seen in figure 5.26. All voltage sources were supplied with low noise power via two serial 120 Ah batteries. DCDC chopper converters provided the required voltages between -24 V and 24 V for the instruments.

The KATRIN high precision HV divider (see [Thü07], [Hoc08]) was available at Mainz during the first half of the measurement period and enabled high precision read-out of the spectrometer potential U_{ana}.

Noise on voltage supplies

Some problems prevented the realization of the HV supply full potential.

- The constellation of U_{back}, U_{ana} and the high precision HV divider acted as an antenna. Hence voltage fluctuations were measurable on both potentials. This noise impaired the expected measurement precision and directly caused a broadening of the measured transmission functions.

- The DCDC chopper converters operate at high frequencies. The choppers additionally increased the noise on the high voltage. Compensation impedances were installed and smoothed the high frequency ripples.

Overall after disconnection of the high voltage divider, installation of impedances at the chopper converters and grounding the HV supply on a star shaped ground, the noise could finally be reduced to about 0.1 V peak-to-peak. This noise has to be considered in the interpretation of all following transmission function measurements, as the functions are broadened.

5.4 Measurement

The measurements were conducted at the Mainz' spectrometer, besides Troitsk, the predecessor of the KATRIN spectrometers.

Change of the source potential U_{tot}

During measurements, several discharges occurred within the spectrometer. Such discharges had been already observed for previous tests with electron

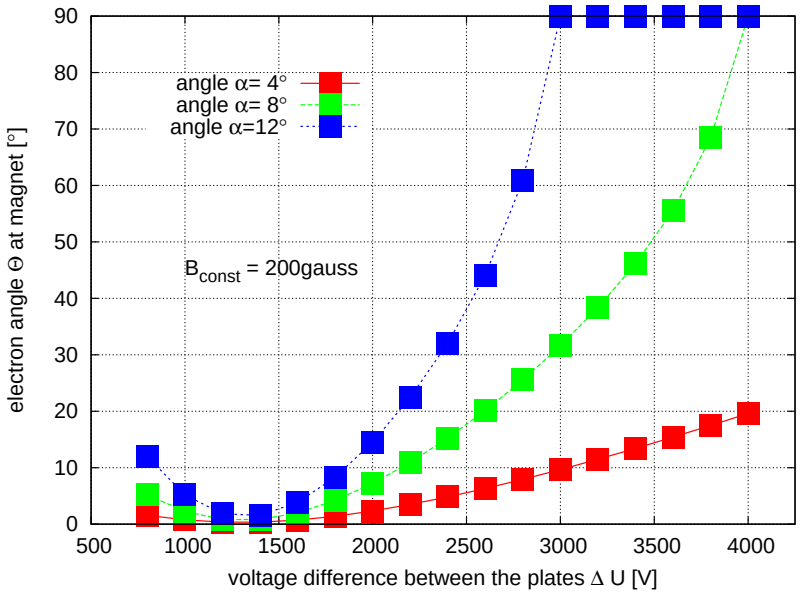

Figure 5.27: Summary of simulations with simplified geometries for the inner fiber (analog to figure 5.17). U_{back} was reduced to $-15\,\text{kV}$. Although the magnetic field strength at the back plate is lower, a simulation for $B = 200\,\text{G}$ is shown, taking into account, that the electron is accelerated over a distance with increasing B-field strength. Simulations for $150 \leq B \leq 300$ show similar results.

sources. It is most probable that the electron source and field emission filled the Penning trap (section 2.3) between front plate and analyzing plane, which led to discharges of the trap.

Indications for discharges had been initially observed for voltages $U_{\text{total}} \leq -12\,\text{kV}$. After conditioning of the plates, no indicates for discharges were observed up to $\leq -16\,\text{kV}$. In the following U_{tot} was kept below $-15\,\text{kV}$, in order to prevent severe discharges and protect the equipment.

Figure 5.27 shows new parallel plate simulations for $U_{\text{tot}} = -15\,\text{kV}$. As can be seen, the basic principle of angular selection is unaffected and measurements were performed with these settings.

5.4.1 Transmission function measurements

Transmission function runs are labeled using the settings of α and ΔU. For transmission function measurements the potential U_{EHS} is scanned from low voltages (no transmission) into full transmission. The potential U_{EHS} determines the potential difference between source and spectrometer and thus the surplus energy of electrons in the analyzing plane. An isotropic emitting source has a broad transmission function over the full resolution of

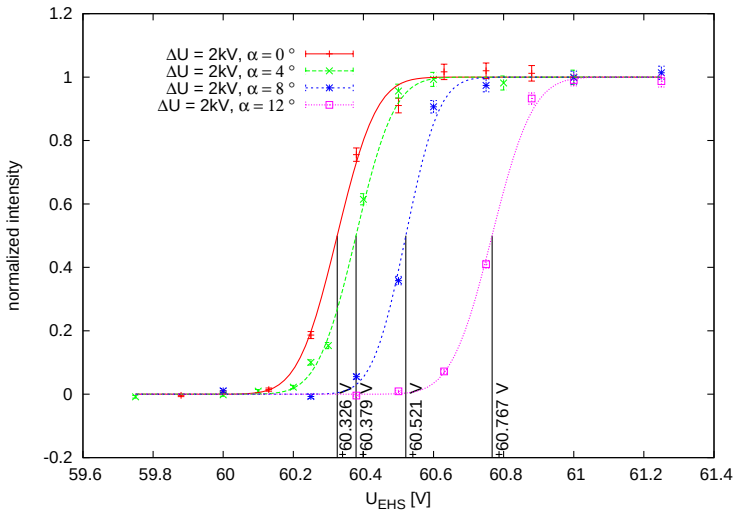

Figure 5.28: Four transmission functions, measured at $\Delta U = 2\,\mathrm{kV}$ and different angles α. The functions were fitted with an error function and the center of the function is illustrated.

the spectrometer. In contrast an ideal source, that emits electrons with only one angle $\theta_{\mathrm{solenoid}}$, has a step transmission function.

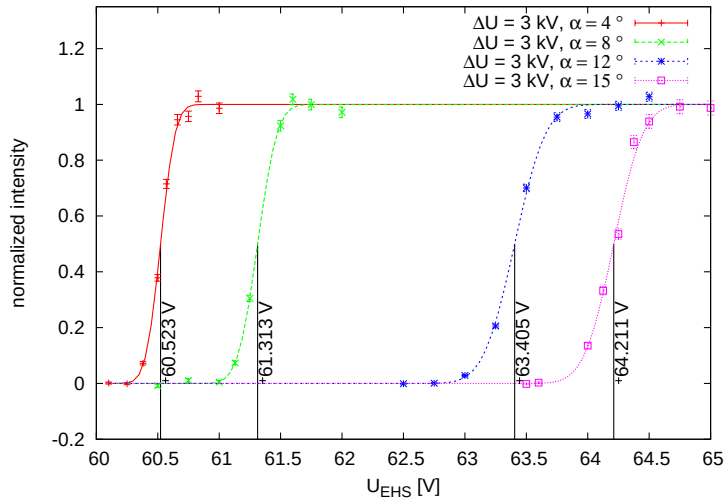

Figure 5.29: Four transmission functions, measured at $\Delta U = 3\,\mathrm{kV}$ and different angles α.

Simulations yield angular spreads for given α and ΔU which was smaller than $\pm 4\,^\circ$ at high angles close to $\theta_{\mathrm{solenoid}} \approx 90\,^\circ$ and below $\pm .3\,^\circ$ at angles

Table 5.1: Typical parameters throughout the measurement period.

U_{ana}	$-15\,\text{kV}$
resolution	$\approx 5\,\text{V}$ at $-15\,\text{kV}$
potential difference ΔU	0 to 4 kV
angle α	0 to 15 °
pressure (source) p_{source}	$< 1 \cdot 10^{-8}\,\text{mbar}$
Outer aircoil currents	19 A
Inner aircoil current	8.8 A
Inner outer aircoil current	5 A
Earth field compensation	$I_{\text{A}} = 15\,\text{A}$
coil currents	$I_{\text{B}} = 40\,\text{A}$
UV-diode current I_{FW}	20 mA, constant

$\theta_{\text{solenoid}} \leq 60\,°$ for an ideal source (see figure 5.16). Hence the transmission function is estimated to be sharp, but not a step function.

To be able to measure the shape of sharp transmission functions in detail, the resolution of the spectrometer was set to $\Delta E = \approx 5.0\,\text{eV}$ at energies of $-15\,\text{keV}$. Typical measurement parameters are listed in table 5.1.

The photoelectron count rates proved as relatively low and one U_{EHS} step of a transmission function was measured for usually 300 s to 1000 s to obtain a significant number of counts. Since the 'inner' fiber, depicted as *fiber I* showed higher count rates than the 'middle' *fiber II*, the transmission functions were almost exclusively measured for the inner fiber.

Four transmission functions for $\Delta U = 2.0\,\text{kV}$ and α varied between 0 and 15 ° are presented with figure 5.28 and 5.29 for $\Delta U = 3\,\text{kV}$. The measured transmission functions are comparatively sharp in comparison to the resolution and each function has a distinct position on the EHS scale. This indicates angular selectivity. However the functions still have a width of $\geq 190\,\text{mV}$. This width is partially attributed to the mentioned noise on potentials U_{ana} and U_{front}. Therefore each transmission function is fitted with an error-function. The error-function is a step function convoluted with a Gaussian, and can describe a sharp transmission function, broadened by noise, starting energies and aperture effects. This is relevant for section 5.5.

The sine-shaped noise on the potential was displayed on a oscilloscope. During the measurement period, noise was successfully reduced from about $\geq 0.5\,\text{V}$ peak to peak to $\approx 0.1\,\text{V}$ peak to peak. An example for the effect of noise on the transmission functions is illustrated in figure 5.30. In the first case the width was decreased from $950 \pm 30\,\text{mV}$ to $480 \pm 10\,\text{mV}$ (left), in the second from $800 \pm 30\,\text{mV}$ to $320 \pm 10\,\text{mV}$ (right). Thereby the width of the function is measured between 10 % and 90 % of the function maximum. In the following the transmission function width will be described by the parameter σ_{sim} of the according fit. This parameter is equivalent to the

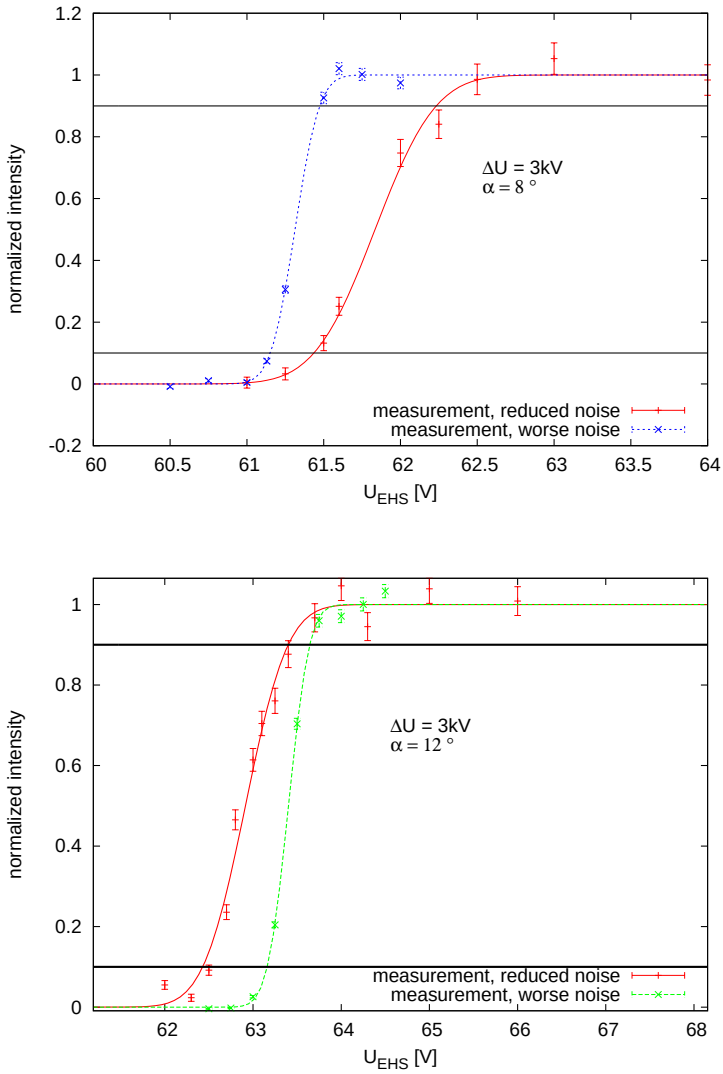

Figure 5.30: Noise on the potential has an influence on the transmission function measurements. From an original $\approx .5\,\mathrm{V}$ peak to peak noise to $\approx .1\,\mathrm{V}$ peak to peak, the width of the transmission function was decreased. It is interesting to note, that for the transmission function illustrated on the left, the onset of function remains constant, whereas on the right, at higher angles, the point of full transmission remains unchanged.

standard deviation σ_{sim} of the gaussian convoluted with the step function.

Figure 5.31 illustrates transmission function measurements for $\alpha = 12\,^{\circ}$ and ΔU from $1.75\,\mathrm{kV}$ to $3.5\,\mathrm{kV}$. For this setting of angle α, photoelectrons were detected up to $\Delta U = 3.5\,\mathrm{kV}$. At higher potential differences ΔU no

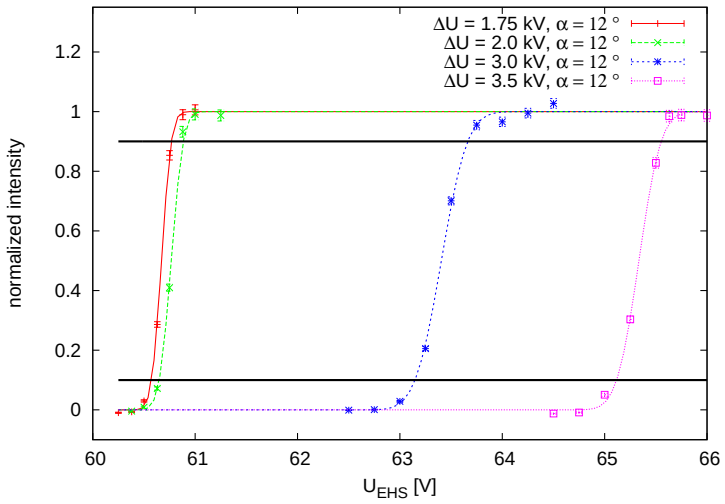

Figure 5.31: Transmission functions for $\alpha = 12\,^\circ$ and four different ΔU. The functions are distributed over approximately the full resolution of 5 V. Below $\Delta U = 1.75\,\mathrm{kV}$ and above $\Delta U = 3.5\,\mathrm{kV}$ no photoelectrons were detected.

photoelectrons were detectable. The center of the transmission function was measured at $U_{\mathrm{EHS}} = 65.33 \pm 0.01\,\mathrm{V}$ for $\Delta U = 3.5\,\mathrm{kV}$. As the resolution amounts 5 V at $-15\,\mathrm{kV}$ and the center of a transmission function for $\alpha = 0\,^\circ$ and $\Delta U = 2\,\mathrm{kV}$ was measured at $U_{\mathrm{EHS}} = 60.326\,\mathrm{V}$ it is highly probable, that electrons close to and above $\theta_{\mathrm{solenoid}} = 90\,^\circ$ are emitted for $\Delta U = 3.5\,\mathrm{kV}$. Electrons with larger angles are then magnetically retarded by the entrance magnet. This interpretation is supported by the reduced width of the transmission function at $\Delta U = 3.5\,\mathrm{kV}$ compared to the one at $\Delta U = 3\,\mathrm{kV}$

5.4.2 Calculation of emitted angles $\theta_{\mathrm{solenoid}}$

Table 5.2 lists measured transmission function center positions. The function positions are distributed over $\approx 5.3\,\mathrm{V}$, which is the approximated resolution of the spectrometer at $-15\,\mathrm{kV}$. This indicates, that photoelectrons with $\theta_{\mathrm{solenoid}}$ between 0 and $90\,^\circ$ have been created.

The width of the functions increases from small angles to larger angles until reaching $\theta_{\mathrm{solenoid}} = 90\,^\circ$. This is in accordance with simulations, where the angular distributions rises with increasing angle $\theta_{\mathrm{solenoid}}$. A large fraction of this width is attributed to the noise on the source and spectrometer potentials.

Since the share of angular spread to the width of the transmission function can not be distinguished from the noise contribution, the angular distribution can only be determined including noise.

Table 5.2: Summary of transmission function measurements: in dependence of α and ΔU, the center position of the transmission function and the width of the function, both derived from the error function fit, are listed.

α ($\pm 0.1\,^\circ$)	ΔU [kV]	U_{EHS} [V]	σ_{TM} [mV]
12°	1.75	60.672 (0.003)	75.2 (5.3%)
12°	2.0	60.767 (0.009)	91.8 (7.7%)
12°	3.0	63.405 (0.011)	200.9 (4.8%)
12°	3.5	65.334 (0.011)	168.4 (7.1%)
4°	3.0	60.523 (0.005)	94.3 (5.3%)
8°	3.0	61.313 (0.009)	126.3 (7.1%)
12°	3.0	63.405 (0.011)	200.9 (4.8%)
0°	2.0	60.326 (0.007)	86.2 (7.3%)
4°	2.0	60.379 (0.008)	86.2 (7.3%)
8°	2.0	60.521 (0.008)	75.2 (13.8%)
12°	2.0	60.767 (0.009)	91.8 (7.7%)
4°	4.0	60.764 (0.013)	126.3 (16.0%)
8°	4.0	62.746 (0.018)	186.1 (23.0%)

5.5 Simulations with realistic geometries

The measurements at Mainz were mostly consistent with the simulations but there were also some discrepancies in comparison to the predictions made based on previous simulations. New simulations with more realistic geometries were conducted with the scope of further understanding the electron source. Especially the width of transmission functions was measured larger than predicted. This effect was expected, since noise, electron starting energy and angle distributions had been neglected before.

A new electron tracking tool based on the routine *elcd2.c* was provided by Dr. F. Glück (Forschungszentrum Karlsruhe). The tool reduced calculation times and allowed the tracking of a larger number of electrons under different starting conditions and with higher statistics. The tool *elcd3_2.c*) used for previous simulations used the method of field calculation via numerical differentiation, which increases accuracy of tracking for geometries including the wire electrodes. Abandoning numerical differentiation *elcd2.c* is faster at computation. It is also able to register interaction with an electrode. Due to the abundance of wire electrodes in the simulation geometry, *elcd2.c* is preferable.

Instead of a constant magnetic field, a realistic magnetic field coil constellation for the Mainz spectrometer was employed. This coil geometry had been used and verified before for [Hug08], [Val09] and simulations for the electron source described in chapter 4.

Since electron tracking for realistic three dimensional geometries is very

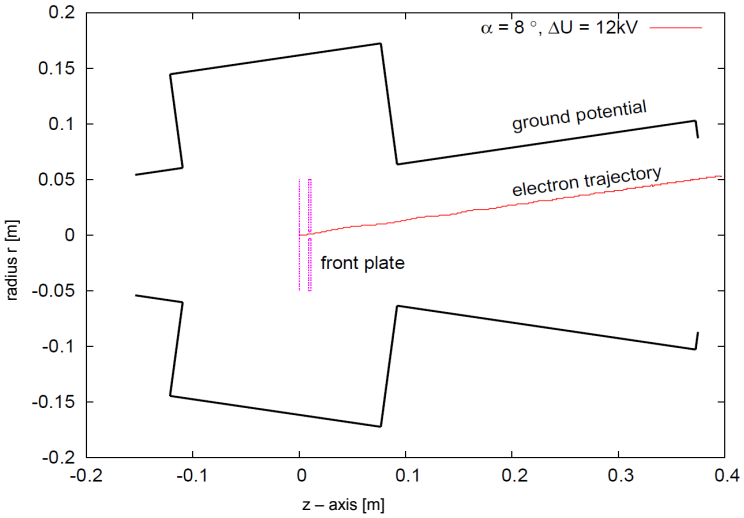

Figure 5.32: Illustration of the approximated geometry using the program *elcd2.c*, which only allows axially symmetric geometries. The parallel plates, surrounded by the vacuum chamber. Due to rotational symmetry the plates were positioned perpendicular to the z-axis and magnetic field (not shown, parallel to the electron trajectory) and chamber were rotated by α. One example electron is tracked from the back plate through the aperture towards the solenoid, which is not shown and positioned at $z \approx 61\,\mathrm{cm}$.

slow and possibly inaccurate, the vacuum chamber around the plates was approximated axially symmetric, see figure 5.32. This geometry on ground potential will affect the acceleration of electrons and their transversal energy gain, thus this approximation is a potential source of error. The angle α was kept below $12\,^\circ$ during the measurements, hence the axial symmetric approximation seems fair.

Electron starting conditions

The electron gains kinetic energy due to the photoelectric effect. The photon energy is defined by the spectrum of the UV-diode, whereas the kinetic energy is depending on the metal work function, as discussed in section 2.2.3.

Randomly distributed over the surface of the 'inner' fiber with its center at $r_1 = 0.10(\pm 0.01)\,\mathrm{mm}$ and a diameter $\oslash_{\mathrm{core}} = 15\,\mu\mathrm{m}$, the electrons were started isotropically with uniformly distributed energies $\leq E_{\mathrm{start}}$ (0 to 0.4 eV), the maximum kinetic energy gained by the photoelectric effect. Angular isotropic distribution means in this case a uniform distribution of $\cos\theta_{\mathrm{start}}$ and ϕ, thus a 2π distribution in forward direction. Both the energy distribution as well as the angular distributions are only approximations and are not exactly known for the real source.

5.5.1 Comparison of simulations with the measurement

For numerous combinations of maximal starting energy E_{start} and field constellations (α, ΔU) simulations were conducted and compared to the measurements. The transmission function measurements are thereby described by the fit parameters and uncertainties, namely the transmission function position on the energy scale and the σ of the fit, according to the width of the function. For comparison of measurement and simulation the lowest transmission function onset and highest observed point of full transmission were regarded as the limits of the resolution, corresponding to $\theta_{\text{solenoid}} = 0$ at $U_{\text{EHS}} = 60.3\,\text{V}$ and $\theta_{\text{solenoid}} = 90\,^\circ$ at $U_{\text{EHS}} = 65.6\,\text{V}$.

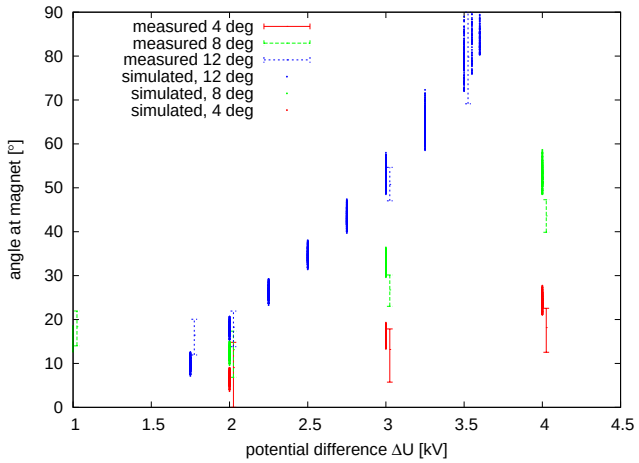

Figure 5.33: Comparison of measurement and simulation in the angular scale (θ_{solenoid}) for three angles α. The angular distributions of simulation and measurement are plotted against the potential difference ΔU. The measurements are thereby depicted by transmission function center position and width, which are translated to an angle at the entrance magnet via

$$\theta_{\text{solenoid}} = \arcsin\left(\sqrt{\frac{U_{\text{EHS}} - 60.3\,\text{V}}{U_{\text{res}}}}\right),$$

with $U_{\text{res}} = 5.3\,\text{V}$. For the simulations with $E_{\text{start}} = 0.12\,\text{eV}$, the angle θ_{solenoid} of randomly started electrons (see text) is illustrated. Discrepancies, between measurement and simulation concerning the transmission function width in comparison can be explained by noise on the potentials U_{back} and U_{ana}, whereas discrepancies of the angle in dependence of ΔU is attributed to differences between real and simulated geometry as well as to a constant offset to all three angles α.

Figure 5.33 shows a comparison of measurement and simulation in the angular scale (θ_{solenoid}), whereas figure 5.34 illustrates the comparison in the

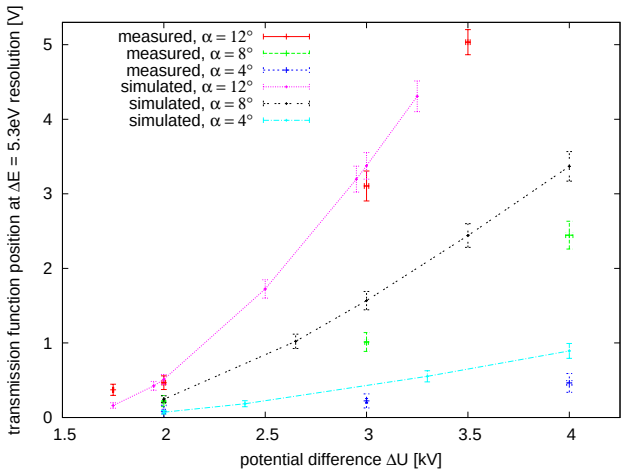

Figure 5.34: For three angles α measurements and simulations are compared in the energy scale analog to figure 5.33.

transversal energy scale. Discrepancies were observed concerning:

- The gain of transversal energy, equivalent to larger angles θ_{solenoid}, is higher for the simulation than for the measurement for all three angles α. This may be explained by deviation of approximated electrode geometries as well as by a constant offset $< 1\,^\circ$, that may be present for the measurements for all three angles α.

- At potential differences $\Delta U = 1.75\,\text{kV}$, the measurements show larger angles than predicted by simulations. In the energy scale, the effect is smaller but observable as well.

Angular distribution for fixed settings of α, ΔU

In order to understand the effect of starting energies on the angular distributions, electrons with three starting energies $E_{\text{start},1} = 0.06\,\text{eV}$, $E_{\text{start},2} = 0.12\,\text{eV}$ and $E_{\text{start},3} = 0.18\,\text{eV}$ were investigated for various field constellations. Electrons with no starting energy are not listed, since the observed angular distribution was negligible small. For the three angles α the standard deviation σ_{sim} of the electron distribution in the energy scale was determined. The corresponding histograms are provided with figure 5.35.

As expected, with larger transversal energies, the angular distribution increases up to the $\theta_{\text{solenoid}} = 90\,^\circ$ cutoff, when electrons are magnetically retarded by the entrance magnet.

Noise on the electrostatic potentials was observed during measurements. This broadened the measured functions. In order to support the validity of simulations by comparing measurement and simulations the following options were taken to estimate the effect.

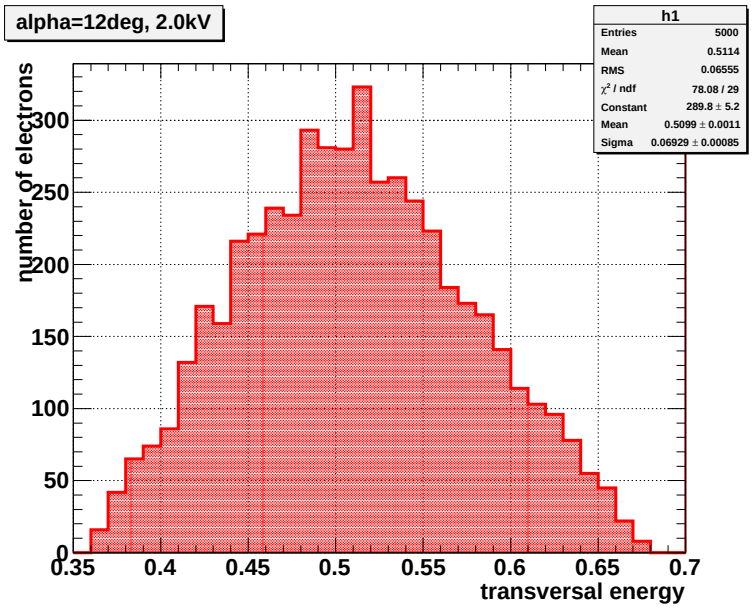

(a) $\alpha = 12°$, ΔU=2.0kV

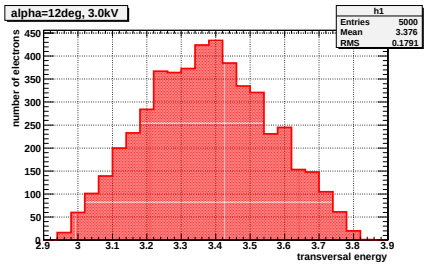

(b) $\alpha = 12°$, ΔU=3.0kV

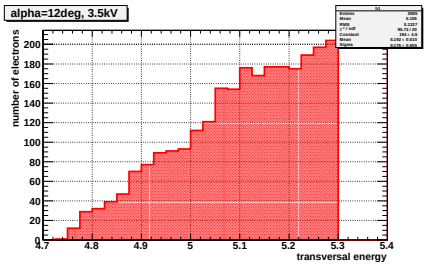

(c) $\alpha = 12°$, ΔU=3.5kV

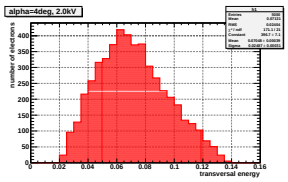

(d) $\alpha = 4°$, ΔU=2.0kV

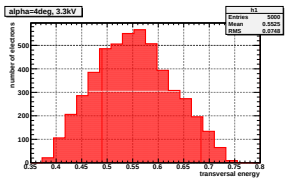

(e) $\alpha = 4°$, ΔU=3.3kV

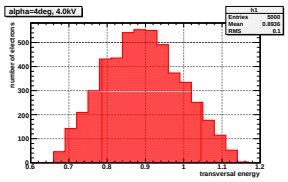

(f) $\alpha = 4°$, ΔU=4.0kV

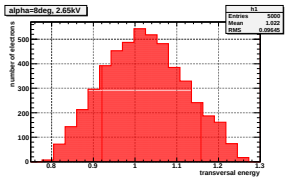

(g) $\alpha = 8°$, ΔU=2.65kV

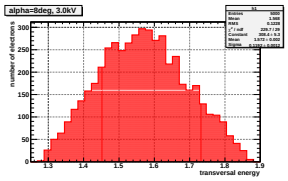

(h) $\alpha = 8°$, ΔU=3.0kV

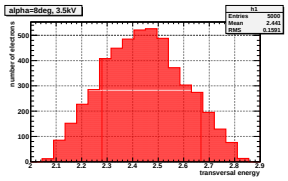

(i) $\alpha = 8°$, ΔU=3.5kV

Figure 5.35: Histograms of the electron transversal energy distribution, equivalent to angular distributions. The distributions are approximated by a Gaussian for further analysis. The distribution for $\theta_{\text{solenoid}} = 90\,°$ at $\alpha = 12\,°$ and $\Delta U = 3.5\,\text{kV}$ is interesting to note, as a fraction of electrons is magnetically retarded and thus the transversal energy spread is reduced. The mean value and RMS of these histograms are listed in table 5.3.

Table 5.3: Summary of simulations, for $\Delta U_{\mathrm{res}} = 5.3\,\mathrm{V}$. Listed are the mean value and root mean square of histograms, see figure 5.35, depicting the transversal energy spread. In figure 5.36 these results are illustrated and fitted with a spline.

α	$E_{\mathrm{start}} = 0.06\,\mathrm{eV}$		$E_{\mathrm{start}} = 0.12\,\mathrm{eV}$		$E_{\mathrm{start}} = 0.18\,\mathrm{eV}$	
	Mean [meV]	RMS [meV]	Mean [meV]	RMS [meV]	Mean [meV]	RMS [meV]
4°	67.87	16.86	71.31	24.04	71.0	29.31
	148.5	25.57	185.1	40.13	151.0	44.30
	180.6	28.45	552.5	74.8	183.0	49.29
	412.0	45.50	893.6	100.0	413.4	78.76
	545.6	57.90			546.7	93.1
	885.1	72.34			885.3	125.2
8°	244.1	32.21	245.0	45.53	246.2	55.76
	1014	68.92	1022	96.45	1013	119.3
	1558	88.15	1568	122.8	1556	152.6
	2429	114.80	2441	159.1	2426	198.7
	3372	140.5	3369	198.6	3367	243.1
12°	157.1	25.94	161.3	365.9	159.5	44.97
	505.5	46.4	424.7	59.66	506.5	80.33
	1715	87.99	511.4	65.55	1713	152.3
	3363	128.6	1724	123.3	3358	222.6
	4293	148.3	3197	173.6	4287	256.7
			3376	179.1		
			4308	205.9		

- A Gaussian fit is viable for comparison of the simulated σ_{sim} with the measured σ_{TM}.
- σ_{sim} was plotted as a function of the center of the Gaussian and interpolated by a spline to obtain σ_{sim} values for U_{EHS} which were not simulated.
- For each measured transmission function (center position), σ_{sim} predicted by simulations is derived using the spline fit.
- In case both noise and angular distribution are normally distributed, the sigma of a transmission function is described by

$$\sigma_{\mathrm{TM}} = \sqrt{\sigma_{\mathrm{sim}}^2 + \sigma_{\mathrm{noise}}^2}. \tag{5.4}$$

  For three maximum kinetic energies E_{start}, the variables σ_{sim} (derived from simulation spline fit) and σ_{TM} (derived from fitted transmission function measurements) are used with equation 5.4. Thus σ_{noise} can be estimated, as listed in table 5.4.
- Figure 5.36 illustrates the comparison of simulation and experiment. The black line demonstrates the effect of $\sigma_{\mathrm{noise}} = 0.0796\,\mathrm{eV}$, the mean value due to table 5.4 for $E_{\mathrm{start}} = 0.12\,\mathrm{eV}$.

- As figure 5.36 shows both the start energy distribution and the noise are needed to describe the measured data.

Table 5.4: Estimated sigma of noise σ_{noise} for three maximum starting energies E_{start}.

simulation	noise	
E_{start} [eV]	mean [mV]	RMS [mV]
0.06	100.6	11.2
0.12	79.6	6.8
0.18	29.3	21.4

5.5.2 Summary

Regarding the mean values and RMS from table 5.4 and figure 5.35 a maximum starting energy $0.12\,\text{eV} < E_{\text{start}} < 0.18\,\text{eV}$ and noise with $49.2\,\text{meV} < \sigma_{\text{noise}} < 83.7\,\text{meV}$ may describe the measurements more accurate, but since several assumptions were made before and simulations do not exactly describe the measurements, the importance of the definition of E_{start} should not be overrated.

According to the simulations a maximum kinetic energy of $E_{\text{start}} = 0.12\,\text{eV}$ to $0.18\,\text{eV}$ is realistic. This is in so far interesting, as assumptions on the work function for the silver layer can be made. The spectrum of the diode with photon energies $4.68(0.15)\,\text{eV}$ is shown in figure 2.2. The precision of work function measurements of silver was increased over the years and amounts to $4.14(0.04)\,\text{eV}$ to $4.45(0.02)\,\text{eV}$ due to M. Chelvayohan and C. H. B. Mee [C+82]. The values describe the surfaces of purified silver monocrystals, especially the sulfur contamination was reduced via argon bombardment. Since the silver layer on the electron source had not been purified, the results of older measurements by Dweydari and Mee [Dwe73] $\Phi_{\text{silver}} = 4.52\,\text{eV}$ to $4.74\,\text{eV}$ are more according to the source.

Overall the gain of transversal energy, according to the selection of θ_{solenoid}, and the angular spread and distribution can be described by simulations sufficiently well and deviations are to be explained mainly by differences between real and simulated geometries and assumed electron starting conditions.

Thus in principle the electron source and its properties are understood and conclusions for following generations of this electron source can be formulated.

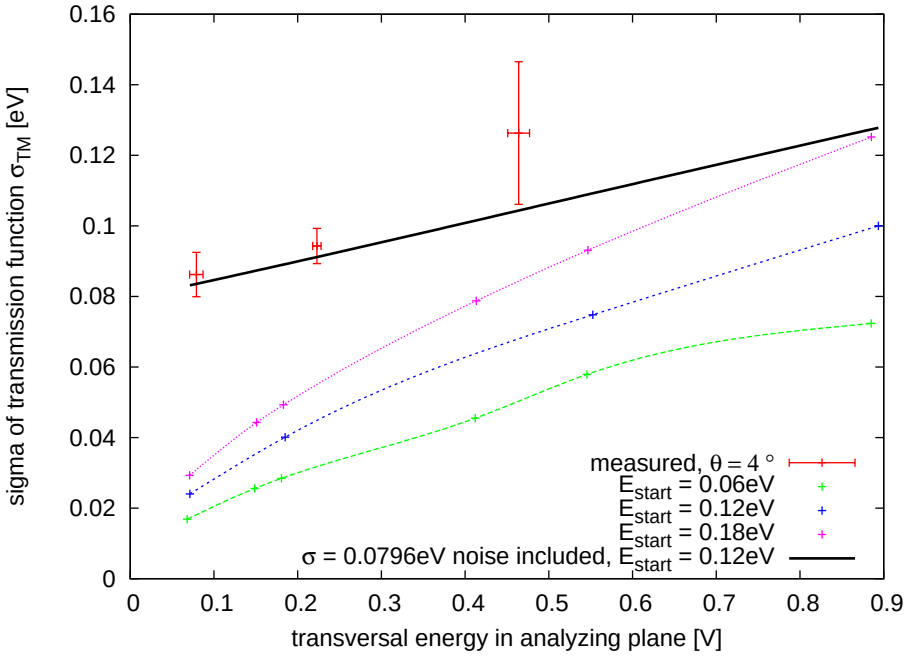

(a) $\alpha = 4°$

Figure 5.36: The simulations for three maximum kinetic electron starting energies E_{start} are compared to the measurements (red with error bars). The σ_{sim} were plotted against the transversal energies, for a resolution $\Delta E = 5.3\,\text{eV}$, and spline fitted. Assuming Gaussian noise ($\sigma_{\text{noise}} = 83.7\,\text{meV}$) and energy distribution for $E_{\text{start}} = 0.12\,\text{eV}$, the sigma of a convolution of both signals is illustrated as a black line. Regarding the case $\alpha = 12\,°$, a larger starting energy and lower noise would describe the measurements more accurately. Comparing with the measurement shows that both start energy distribution and noise are needed to describe the data.

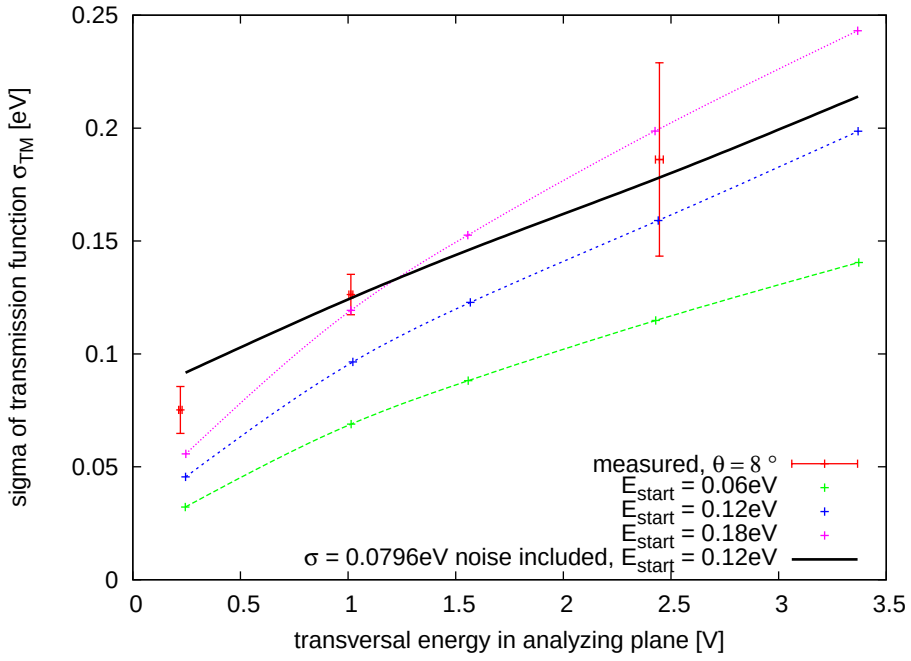

(a) $\alpha = 8°$

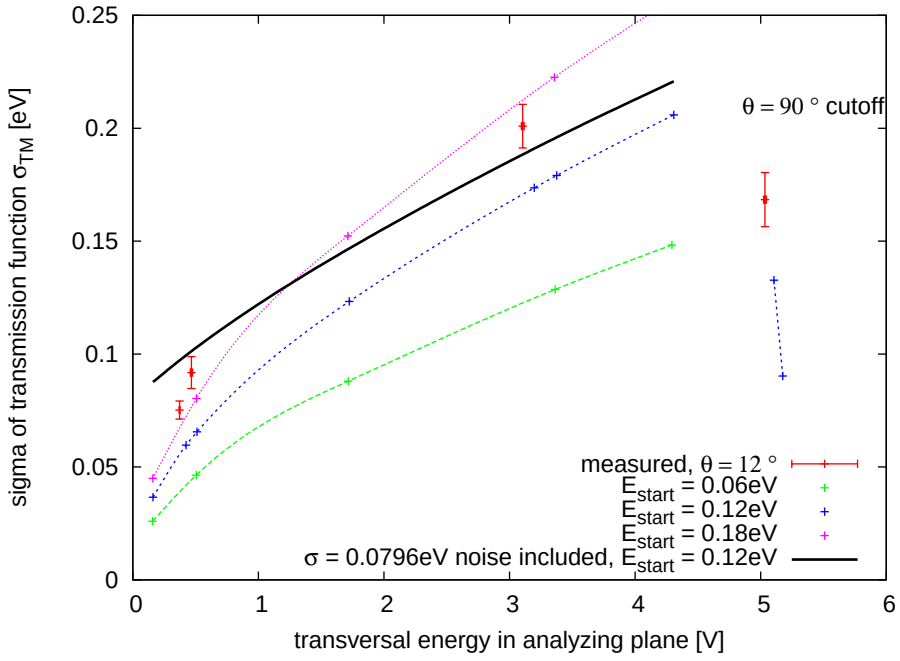

(b) $\alpha = 12°$

Figure 5.36: continued

Chapter 6

Conclusion and Outlook

The properties of the electron source are in principle well understood. By reduction of effects like starting energy and source environment the source has the potential to create well defined electrons, concerning energy and angle. Thereby only two parameters (α, ΔU) are relevant for the angular selection in the experiment. The principle of angular selectivity was proven in section 5.4, but further development of this source may be useful.

Acceleration against ground potential

First of all I want to discuss the source geometry. As seen for the simulations with realistic geometries, the ground potential affects the acceleration of electrons behind the plates. By using fixed geometries the influence of the surrounding environment, namely the vacuum chamber, can mostly be reduced.

- There are several ways of implementation, for example a second plate on ground potential with an aperture at a slightly larger distance. Such a geometry was first investigated and simulated before we chose to construct a source with only two plates. Due to lens effects this geometry was at first considered as highly chaotic and small effects like change of ΔU and α had large effects. Additionally the second lens increased the angular distribution. Anyhow that investigated setup had a distance of ≈ 2 to 3 cm between second and third plate, mostly due to the limited space at the ellipsometry chamber. An aperture on ground potential at larger distances ≈ 10 to 20 cm might be worth investigating.

- Other possibilities are a pipe on ground potential, mounted at a close distance of a few cm behind the front plate and with a sufficient diameter to reduce lens effects, as proposed by F. Glück (Forschungszentrum Karlsruhe)

- or acceleration against an array on ground potential.

Angular distribution due to starting conditions

The starting conditions show large effects on the angular distribution. It is advisable to reduce the electron starting energy, gained by the photoelectric effect. This is achieved by matching cathode material and light source. Since UV diodes possess spectra with relative large FWHM the work function of the material should at least accord to the spectrum peak position. However higher work functions result in decreased photoelectron count rates.

Another possibility is the application of lasers, with selectable center wavelengths. Lasers were not advisable for proof of principle measurements at the Mainz spectrometer, but for a high precision electron source, e.g. for KATRIN, the arguments lapse with the background, that the relative broad diodes spectra increase the angular distribution by far. By matching the laser wavelength to the cathode material the electron starting energy might be significantly reduced.

Optimization of optical coupling and fibers

The optical coupling between fiber and light source requires enhancements in comparison to previous couplings. The application of lasers would by far increase the effectiveness of the coupling, since lasers can relatively easy be connected to a fiber.

Since external illumination is technically very challenging, continuing with the application of fibers is advisable. Anyhow the selection of fibers might be reconsidered. The attenuation of UV-light by the fiber is high and new fibers, providing higher UV-light intensities at the back plate, might be commercially available on the market. Also the fiber coating and fixation of fiber (by gluing) in the back-plate require further improvement. The coating became brittle due to contact to the epoxy glue and the otherwise resilient light guide was vulnerable. Damage to the fiber casts the electron source useless and needs to be prevented.

Appendix A

A: Technical drawings

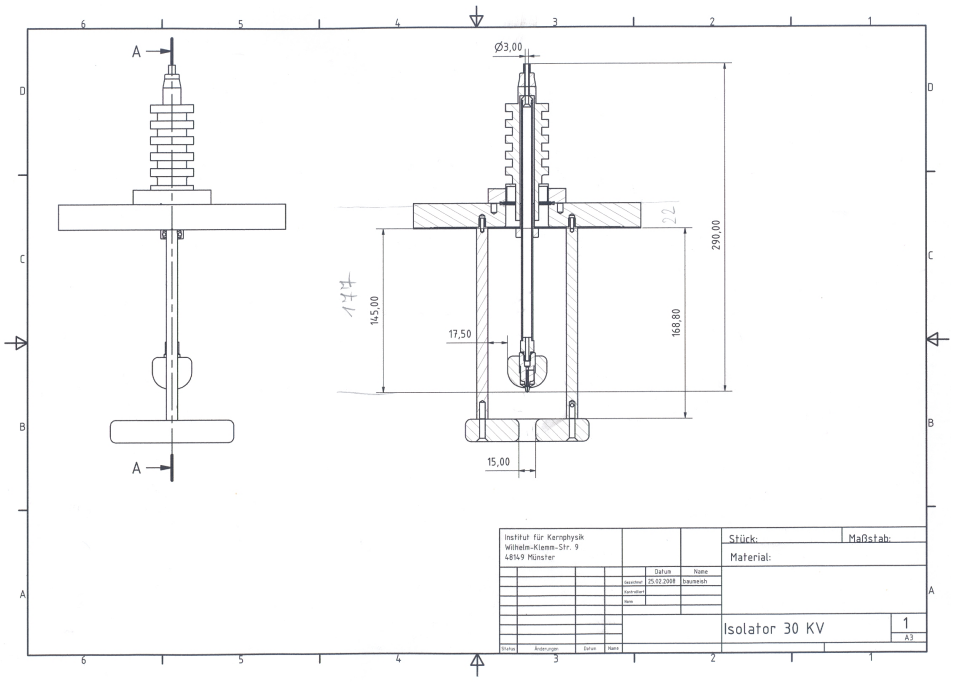

Figure A.1: Blueprint of the angular selective electron gun, based on the curvature of the surface (see chapter 4).

Appendix B

B: UV-Diode spectra

Calibration and uncertainties at measuring the UV-LED spectra

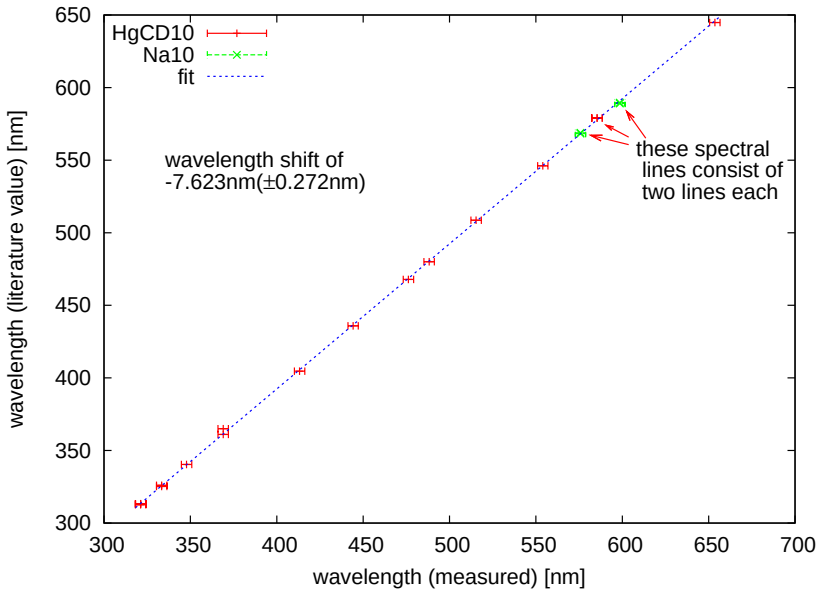

Figure B.1: Calibration of the Jobin Yvon H10 monochromator. The distinct spectral lines of *HgCD10* and *Na10* spectral lamps were measured and plotted against the literature values [Wea81]. A linear function accurately fits the measurement, thus the only observable falsification is a constant offset between measured values and literature values. The ordinate intersection $\lambda_o = 7.623(\pm 0.272)\,\mathrm{nm}$ corresponds to the monochromator offset. This offset is regarded in all provided figures.

For the calibration of the monochromator, the distinctive spectral lines of *HgCD10* and *Na10* spectral lamps were measured. The calibration results are shown in figure B.1.

Besides the calibration, two further effects have to be taken into account, since they are implied in the measured spectra.

1. The PIN photodiode suffers from low detection efficiency at short wavelengths and the spectral response at about 230 nm to 300 nm, as provided in figure B.2, does affect the measurement. The spectral response will especially be notable concerning the signal intensity in comparison for both measured spectra. The spectral response was fitted with a function, to correct the provided figures.

2. The wavelength dependent resolution Δ_λ of the grating spectrometer causes a broadening of the determined spectrum, since the detector measures the convolution of the original spectrum and the monochromator resolution in the UV-range. To estimate Δ_λ we used a device by measuring the broadening of a the NaD line, which is in fact a superposition of two lines at

   - $\lambda_{\mathrm{NaD},1} = 588.995\,\mathrm{nm}$ and
   - $\lambda_{\mathrm{NaD},2} = 589.592\,\mathrm{nm}$.

   We then assume the Doppler broadening and the broadening due to pressure and lamp temperature to be zero, which is very unlikely. This means that the measured broadening of about $5\,\mathrm{nm} \leq \Delta\lambda_{\mathrm{NaD}} \leq 6\,\mathrm{nm}$ was caused only by the resolution of the grating spectrometer at $\lambda_{\mathrm{NaD}} \approx 589.3\,\mathrm{nm}$. Due to the resolution mechanic of a grating spectrometer

   $$\frac{\Delta\lambda}{\lambda} = A = const. \tag{B.1}$$

   the *FWHM* caused by spectrometer resolution at $\lambda_{\mathrm{LED}} = 265\,\mathrm{nm}$ is

   $$\Delta\lambda_{\mathrm{LED}} = \frac{\lambda_{\mathrm{LED}}}{\lambda_{\mathrm{NaD}}} \cdot \Delta\lambda_{\mathrm{NaD}} \leq 2.7\,\mathrm{nm} \tag{B.2}$$

   at most.

   Pressure and Doppler broadening, which are unknown for the used spectral lamp, generally play a superior role at spectral line broadening, so apparently the resolution will be way below $\Delta_{265\,\mathrm{nm}} \ll 2.7\,\mathrm{nm}$. Hence the resolution does only slightly affect the spectral measurement.

3. The time dependent evolution of the LEDs spectra might also be of interest, considering that pulses of varying length will be used in the experiment. M. Shagatov et al. [S$^+$03] investigated the spectral evolution of *UV-LEDs*. The investigated AlGaN diodes are related to the *T9B25* and *T9B26*. To outline one conclusion, the ultraviolet fraction of the spectrum developes within a few ns, while the optical fraction takes longer, in the order of 300 ns, to develop.

All three effects will therefore only slightly affect the measured optical spectrum.

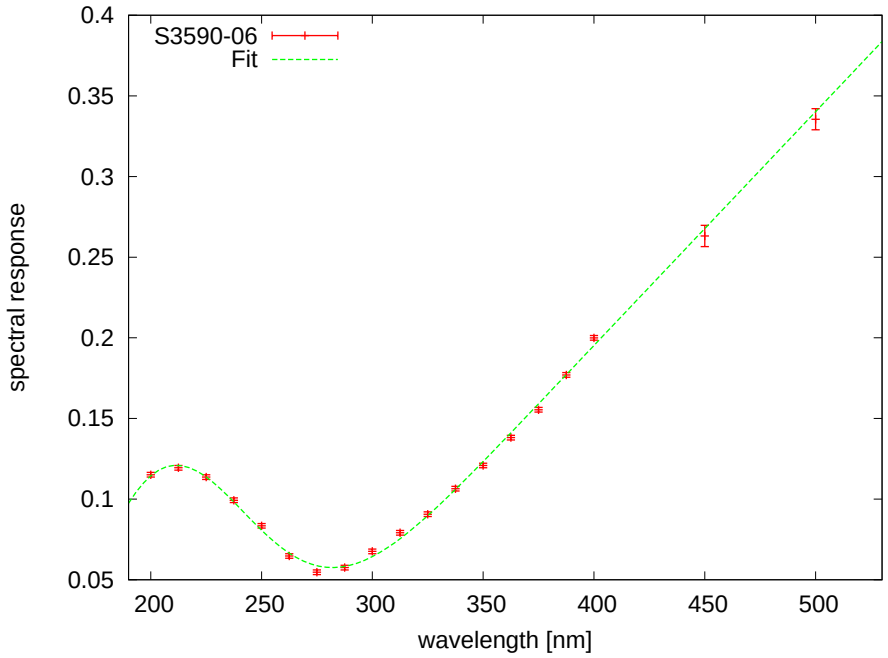

Figure B.2: The spectral response function of a Hamamatsu S3590-06 in the relevant wavelength regime, including the fit used for correction purposes. The minimum is close to the diodes peak wavelengths, thus the spectral response has to be regarded at spectra measurements.

Bibliography

[A+59] P. A. Anderson et al. Work function of gold. *Phys. Rev.*, 115:553–554, 1959.

[C+82] M. Chelvayohan et al. Work function measurements on (110), (100) and (111) surfaces of silver. *J. Phys. C*, 15:2305–2312, 1982.

[Col05] The KATRIN Collaboration. KATRIN design report. 2005.

[Dun] J. Dunmore. Pixelation-dependence of transmission function, *KATRIN* internal document, BSCW: Review of Detector Design SUMMER 07.

[Dwe73] A.W. Dweydari. *Phys. Status Solidi a*, 17:247, 1973.

[Eas70] D. E. Eastman. Photoelectric Work Functions of Transition, Rare-Earth, and Noble Metals. *Phys. Rev. B*, 2, 1970.

[Frä07] F. Fränkle. KATRIN internal document, BSCW: Detector - Electron Gun. 2007.

[H+66] E. E. Huber et al. The effect of mercury contamination on the work function of gold. *Appl. Phys. Lett.*, 8:169–171, 1966.

[Ham] Hamamatsu product documentation for Deuterium lamp L6565.

[Ham08] D. Hampf. *Untersuchung der APD S1315 von RMD im Hinblick auf ihren Einsatz als Detektor am SpecTrap Experiment.* Diploma thesis, Westfälische Wilhelms-Universität Münster, 2008.

[Hoc08] F. Hochschulz. *Weiterentwicklung der Präzisions-Hochspannungs-Messung für das KATRIN-Experiment.* Diploma thesis, Westfälische Wilhelms-Universität Münster, 2008.

[Hug08] K. A. Hugenberg. *Design of the electrode system for the KATRIN main spectrometer.* Diploma thesis, Westfälische Wilhelms-Universität Münster, 2008.

[Lid08] D. R. Lide, editor. *Handbook of Chemistry and Physics.* CRC Press, 2008.

[Ost09] B. Ostrick. *Eine kondensierte ^{83}Kr-Kalibrationsquelle für das KATRIN Experiment.* PhD thesis, Westfälische Wilhelms-Universität Münster, 2009.

[Pic92] A. Picard. A solenoid retarding spectrometer with high resolution and transmission for keV electrons. *Nuc. Instr. Meth. B*, 63, 3:345.358, 1992.

[S+03] M. Shatalov et al. Time-resolved electroluminescence of AlGaN-based light-emitting diodes with emission at 285nm. *Appl. Phys. Letters.*, 82:167–169, 2003.

[Sav95] G.F. Saville. Feasibility study of photocathode electron projection lithography. *J. Vac. Sci. Technol.*, B 13, 6:2184–2188, 1995.

[Smo41] R. Smoluchowski. Anisotropy of the electronic work function of metals. *Phys. Rev*, 60:661–674, 1941.

[Str09] S. Streubel. *Aufbau eines PET-Demonstrations-Experimentes und Anwendung von dessen FADC-basiertem Datenaufnahmesystem für Photoelektronenspektroskopie.* Diploma thesis, Westfälische Wilhelms-Universität Münster, 2009.

[Thü07] T. Thümmler. *Präzisionsüberwachung und Kalibration der Hochspannung für das KATRIN-Experiment.* PhD thesis, Westfälische Wilhelms-Universität Münster, 2007.

[V+09] K. Valerius et al. A UV LED-based fast-pulsed photoelectron source for time-of-flight studies. *New Journal of Physics*, 11, 6, 2009.

[Val04] K. Valerius. *Elektromagnetisches Design für das Hauptspektrometer des KATRIN Experiments.* Diploma thesis, Westfälische Wilhelms-Universität Münster, 2004.

[Val09] K. Valerius. *Spectrometer-related background processes and their suppression in the KATRIN experiment.* PhD thesis, Westfälische Wilhelms-Universität Münster, 2009.

[Vöc08] S. Vöcking. *Implementierung der Multipole Boundary Element Methode für das KATRIN-Eperiment.* Diploma thesis, Westfälische Wilhelms-Universität Münster, 2008.

[W+99] S. G. Walton et al. Low energy, ion-induced electron and ion emission from stainless steel: The effect of oxygen coverage and the implications for discharge modelling. *J. Appl. Phys.*, 85:1832, 1999.

[Wea81] R. C. Weast, editor. *Handbook of Chemistry and Physics.* CRC Press, 1981.

[Zac09] M. Zacher. *Electromagnetic design and field emission studies for the inner electrode system of the KATRIN main spectrometer*. Diploma thesis, Westfälische Wilhelms-Universität Münster, 2009.

[Zbo] M. Zbořil. *thesis in prep.* PhD thesis, Westfälische Wilhelms-Universität Münster.

Danksagung

Ich möchte hiermit allen danken, die, sei es direkt oder indirekt, bei der Verwicklichung dieser Diplomarbeit mitgewirkt haben.

Ein großer Dank geht an Prof. Weinheimer, der es schafft sich neben seiner Forschung auch redlich um seine Studenten und Mitarbeiter zu kümmern, stets ein offenes Ohr für mich hatte und mir erst die Arbeit an diesem interessanten Thema ermöglichte.

Weiterhin möchte ich Prof. Frekers für die Übernahme der Zweitkorrektur dieser Arbeit danken.

Besonders bedanken möchte ich mich bei Marcus, Kathrin und Karen für Eure engagierte Betreuung. Unter anderem möchte ich mich herzlich bei Euch für all die Mühen beim Gegenlesen dieser Diplomarbeit und die vielen hilfreichen Vorschläge und Anregungen bedanken, auch wenn sie nur einen Teil Eurer tollen Unterstützung ausmachen.

Ein großer Dank gebührt Hans Werner und Helmut, die mit ihrer kompetenten Unterstützung die Realisierung der Elektronenkanonen erst möglich machten.

Zusätzlich zu den genannten Personen gebührt der Dank allen, die mit mir zusammen die außergewöhnliche Zeit in Mainz voller Höhen und Tiefen, sprich Messzeiten, durchgestanden haben. Danke für die Strapazen, die Ihr auf Euch genommen habt, für all Euren Einsatz und all die Ideen, die diese Messphasen erst zu einem Erfolg führten.

Ich danke den Mitarbeitern der Firma j-fiber GmbH, Jena, für die gute Zusammenarbeit und Unterstützung bei der Auswahl passender Lichtwellenleiter.

Ausserdem möchte ich natürlich allen Mitgliedern der AG Weinheimer und inbesondere meinem Büro für die tolle Zeit danken. Macht weiter so!

Zu guter Letzt gebührt meiner Familie, besonders meinen Eltern und meinem Bruder, ein großer Dank. Ihr habt mich immer unterstützt und ich kann mir keine bessere Familie vorstellen.

Vielen Dank!